Copyright

by

Xu Feng

2019

The Dissertation Committee for Xu Feng Certifies that this is the approved version of the following Dissertation:

BIOPHYSICAL BASIS OF SKIN CANCER DETECTION USING RAMAN SPECTROSCOPY

Committee:

James W. Tunnell, Supervisor

Andrew K. Dunn

Thomas E. Milner

Matthew C. Fox

BIOPHYSICAL BASIS OF SKIN CANCER DETECTION USING RAMAN SPECTROSCOPY

by

Xu Feng

Dissertation

Presented to the Faculty of the Graduate School of

The University of Texas at Austin

in Partial Fulfillment

of the Requirements

for the Degree of

Doctor of Philosophy

The University of Texas at Austin

August 2019

Dedication

To my parents, my husband, and my dear daughter.

Acknowledgements

First and foremost, I would like to thank Dr. James Tunnell. I was very fortunate to have you as my supervisor during my Ph.D. pursuit. You are not only my advisor, but also a role model in my life. You encouraged me when I was faced with difficulties in research; you cared about me and always offered to help; and you gave me strong support for career development.

I am grateful to the faculties and staff who helped me fulfill this work. Dr. Mia Markey gave me crucial guidance in statistical analysis and clinical decision making. Dr. Aaron Baker supplied me with the histology facility. Dr. Tim Yeh gave me advice on qualifying exam and career planning. Dr. Andrew Dunn and Dr. Thomas Milner assessed my academic progress to make sure I was on the right track. Greg Lyness and Esther Maier from College of Pharmacy provided histology service, and Erika Hale from Department of Statistics and Data Sciences offered statistical consulting. Our BME staff were also of great help: Bobby Knight, Jim Pollard, Lacy Whites, Chase Dawkins, Margo Cousins, Sophia Bixby, and the administrators that have worked with our lab.

I want to acknowledge Seton Healthcare family and the Austin Dermatological Surgical Center for collaboration. Dr. Matthew Fox and Dr Jason Reichenberg, thanks for your enthusiasm in translating our work from benchtop to bedside. Katherine Sebastian and Fabiana Lopes, thanks for consenting the patients so I could collect the qualified tissue for experiment. Sandra Esparza and Leandra Turner, thanks for providing the Mohs sample and making my trips to the clinic enjoyable.

I want to thank everyone in the Tunnell lab. Dr. Liang Lim, I have learned a lot from you. I was touched by the long email you sent me two years ago when I had difficulty

deciding my future career. Dr. Will Goth, I cannot believe six years have passed, and we will both start a new chapter in the same city. Hieu Nguyen and Yao Zhang, thanks for bringing energy to the lab, and initiating fun lab activities such as Color Run and Zilker Relays. Jason Zhang, I appreciate that you worked as an undergraduate researcher with me for 3 years. Dr. Austin Moy, I learned the communicating and writing skills from you. Dr. Bin Yang, Dr. Varun Pattani, Dr. Manu Sharma, Dr. Ricky Hennesy, Jason King, Andrew Stier, and Dr. Susie Torres-Hurtado, thank you all for playing a part in my graduate study.

I also want to thank a few colleagues from other labs. Dr. Evan Perillo generously helped me with the software control of the confocal laser-scanning microscope. Colin Sullender, Lisa Richards, Shams Kazmi, David Milner, and Ahmed Hassan, thanks for organizing Biomedical Optics and Graduate Organization (BOGO). Travis Cantu, Subhamoy Das, Andrew Mark, Cong Liu, Peng Chen, Yen-Liang Liu, Chengyi Tu, Chi Zhao, Kai Liu, Haibo Li, you have helped me in different aspects of life.

I gratefully acknowledge the funding sources that made my dissertation work possible. I was funded by the Cancer Prevention & Research Institute of Texas (CPRIT) for the first 4 years, and UT Graduate Continuing Fellowship for the last year. My work was also partially supported by other fellowships from the UT Graduate School.

Last but not least, I would like to thank my family. Being thousands of miles away, my parents always told me not to worry about them, just “study well, eat well and be safe”. Their selfless love motivated me to overcome challenges with no fear. My husband Di gave me plenty of love and encouragement. We had so many unforgettable memories in Austin – we met, got married, and had our lovely daughter here. I am tremendously grateful to have you and Carina in my life.

Abstract

BIOPHYSICAL BASIS OF SKIN CANCER DETECTION USING RAMAN SPECTROSCOPY

Xu Feng, Ph.D.

The University of Texas at Austin, 2019

Supervisor: James W. Tunnell

The goal of this dissertation is to study the potential of Raman spectroscopy in improving the clinical diagnosis of skin cancer, including two main applications: noninvasive screening of melanoma skin cancer and surgical margin detection of nonmelanoma skin cancer.

Skin cancer is the most common type of malignancy, accounting for over 5.4 million cases and 10 thousand deaths per year in the United States alone. Like most cancers, the current "gold standard" diagnosis relies on biopsy and histopathology, which is invasive, time-consuming, and costly. Moreover, large numbers of benign lesions are biopsied for melanoma diagnosis, resulting in substantial financial burden and patient discomfort. Therefore, an urgent need exists to develop a noninvasive, fast, and accurate method for skin cancer detection.

The first part of the dissertation focuses on exploring the biophysical origin of *in vivo* melanoma detection. Our group has previously reported on the development of a clinical Raman spectroscopy system towards spectral biopsy of skin; however, the biochemical changes that Raman spectroscopy relies on for accurate melanoma diagnosis

remained unclear. As a result, we proposed a biophysical inverse model to address this issue. To build the model, we established a custom confocal Raman microscope to extract *in situ* human skin constituents spanning normal and various diseased states. Our results indicate collagen, elastin, keratin, cell nucleus, triolein, ceramide, melanin, and water are the most important model components. Furthermore, collagen and triolein are the most relevant markers to discriminate malignant melanoma from benign nevi.

The second part of the dissertation discusses the biophysical basis of nonmelanoma skin cancer margin delineation. We discovered the diagnostic markers to accurately differentiate tumor from normal skin, which is critical to maximize positive patient outcomes in skin cancer surgery. The biochemical changes derived from our model were highly correlated with histopathological diagnosis. We further demonstrated the feasibility of a superpixel acquisition approach for rapid classification of tumor boundaries in skin biopsies. Our results suggest Raman spectroscopy will be a powerful tool for intraoperative surgical guidance.

Table of Contents

List of Tables

List of Figures

Chapter 1: Introduction

This chapter will start from an introduction of skin cancer, followed by the conventional method for skin cancer detection. Next, the optical methods will be introduced, including our primary research tool – Raman spectroscopy. The two main challenges of Raman spectroscopy in cancer research will be discussed, which becomes the motivation of this dissertation. Finally, this chapter will introduce the outline of this dissertation.

1.1 Background of Skin Cancer

Skin cancer is the most common type of malignancy, accounting for over 5.4 million cases and 10,000 deaths per year in the US alone [1]. Skin cancer can be divided into two types: melanoma and nonmelanoma skin cancer. Basal cell carcinoma (BCC) and squamous cell carcinoma (SCC) are the two most common types of nonmelanoma skin cancer. BCC accounts for approximately 75% of all skin cancers, while SCC makes up approximately 20% of all skin cancers. Although nonmelanoma skin cancer is usually not fatal, it can cause significant local damage and can metastasize if left untreated [2]. On the contrary, melanoma accounts for less than 2% of all skin cancer cases, but it contributes to a vast majority of skin cancer deaths. When detected at an early stage, most of the melanomas can be treated and cured by standard surgical excision. While at later stages, the risk of progression to lethal metastatic disease dramatically increases [3].

1.2 Standard of care in skin cancer detection

Detection is a general term that defines the action or process of identifying the presence of tumor. Current standard-of-care in skin cancer detection involves both screening and treatment.

At present, the standard-of-care for skin cancer screening relies on visual inspection of suspicious lesions followed by biopsy and histopathology. The biopsies are performed

in a dermatologist's office and then sent to the histopathology lab for further examination. A few additional days may be needed to deliver the final results. These biopsy procedures are invasive, inefficient, and inconvenient. More importantly, the process has low diagnostic accuracy (49-81% among dermatologists for melanoma [4]). The number of pigmented lesions needed to be excised to identify one melanoma, also called "negative biopsy ratio", varies among dermatologists, new and experienced general practitioners [5]. The negative biopsy ratio varies between 6.3:1 and 8.7:1 by dermatologists, and between 20:1 and 30:1 for general practitioners [6]. The negative biopsy ratio can be even higher for female patients and young patients (less than 30 years old) [7]. Large numbers of biopsies are performed on benign skin, leading to a substantial financial burden to the healthcare system and the patients. According to a recent study, the estimated cost of biopsied benign tumors ranges from $624 million to $1.7 billion [8]. As a result, a critical need exists to develop a noninvasive, accurate, fast, and inexpensive method for early skin cancer screening.

The standard-of-care for skin cancer treatment is surgery. As to melanoma skin cancer, standard surgical excision or wide excision is commonly employed to remove the melanoma and a small margin of normal skin around it. The margin of normal skin depends on the thickness and location of the melanoma [9]. For nonmelanoma skin cancer, common types of surgery include standard surgical excision, Mohs micrographic surgery (Mohs), curettage and electrodesiccation, and cryosurgery [10]. Particularly, Mohs surgery is a precise surgical technique that aims to remove all the tumor cells, while preserving as much of the surrounding healthy tissue as possible. Mohs surgery is by far the most effective treatment for high-risk BCC and SCC. According to one study, the 5-year recurrence rate of Mohs is 1 – 3% for primary BCC and 5 – 7% for recurrent BCC. In contrast, the 5-year recurrence rate of standard surgical excision is 3 – 10% in primary BCC and >17% in recurrent BCC [11].

1.3 Optical Techniques for Skin Cancer Detection

The maturing of photonic technologies has created an opportunity to develop the optical biopsy – a minimally invasive or noninvasive alternative to the traditional biopsy. The basic principle of optical biopsy is to interact with a tissue using light, and then decode the returned signal containing the characteristic of the tissue.

Ideally, an optical biopsy needs to meet four main requirements in order to achieve the maximum clinical significance. An optical biopsy needs to have (1) high resolution to reveal cellular or subcellular content; (2) high speed for real-time measurement; (3) high penetration depth to investigate a lesion in three-dimension; (4) molecule-specific and label-free detection [12]. Unfortunately, optical techniques can hardly meet all the requirements, because interrelationships exist among those requirements. For example, in spectroscopic field, high resolution imaging often results in slow acquisition speed. High resolution image acquired at high speed is often at the tradeoff of the spectral content. Another tradeoff exists between penetration depth and resolution: improving axial resolution may decrease the maximum possible imaging depth, as in the case of optical coherence tomography.

The remainder of this section will introduce several optical biopsy methods that have demonstrated to be promising in skin cancer detection. They are divided into non-spectroscopic techniques (including reflectance confocal microscopy, coherence optical tomography, two-photon-excited fluorescence, second-harmonic generation), and spectroscopic techniques (including diffuse reflectance, laser-induced fluorescence, infrared, and Raman spectroscopy). All the methods introduced here are label-free, so techniques such as surface-enhanced Raman scattering (SERS) [13-15] that involves exogenous enhancement mechanism are not within the scope of this introduction.

1.3.1 Non-spectroscopic Techniques

Reflectance confocal microscopy (RCM) allows for the evaluation of skin at the cellular level (0.5 – 1.0μm lateral resolution, and 1 – 3μm optical sectioning). The basic

contrast mechanism is the changes in refractive index. RCM has become a valuable adjunct to dermoscopy, and has been successfully translated from benchtop to bedside (Vivascope 1500 and Vivascope 3000 (a handheld version), Caliber I.D. Inc., Rochester, NY, USA) [16-18]. RCM is a promising tool for the diagnosis of melanocytic lesions. RCM is particularly accurate for light-colored lesions (specificity was 39% for dermoscopy and 84% for RCM) [19]. In a preliminary study, a sensitivity/specificity of 94%/94% was obtained for detecting BCC cancer margin [20]. Limitations of RCM include: (1) limited imaging depth of approximately 250μm, so information deeper than the upper reticular dermis cannot be captured; (2) time required to scan and training needed to read the images; (3) low contrast of nucleus as compared to hematoxylin and eosin (H&E) histopathology. To solve (3), aluminum chloride is routinely used to enhance for nuclear contrast. Aluminum chloride generates compaction of chromatin, which can result in increased backscatter and brightening of nuclear morphology [17, 18].

Optical coherence tomography (OCT) imaging also detects the changes in refractive index. OCT is the optical analog of ultrasound. One major advantage of OCT is it can provide real-time 1D depth, 2D cross-sectional, and 3D volumetric images in real-time. Besides, OCT has a deep penetration depth. Frequency domain OCT can probe as deep as 2mm with enough cellular clarity to diagnose nonmelanoma skin cancers [21]. OCT has demonstrated promising outcomes by enabling accurate margin mapping of nonmelanoma skin cancer in advance of Mohs micrographic surgery [22]. In another study, OCT can predict BCC with an overall sensitivity of 89% and specificity of 60% [23]. OCT has been combined with RCM in a handheld device for detecting and delineating the margins of BCC *in vivo*. The result demonstrated that using combined OCT and RCM facilitated the identification of superficial and nodular BCCs, as well as lateral and deep margins [24]. Despite of the success, the technical challenges associated with OCT have limited its application in oncology. For instance, large volumes of tissue need to be imaged at high cellular resolution to detect cancer. Besides, OCT image interpretation may also be challenging for oncologists [25].

Two-photon-excited fluorescence (TPEF), and second-harmonic generation (SHG) are the two major types of nonlinear optical imaging tools. TPEF and SHG both depend on simultaneous interaction of two photons with the tissue. Different from TPEF, SHG does not have energy loss, so the excited photon has exactly twice the energy of the interacting photons (thus the emission frequency is the twice of the excitation frequency). The contrast mechanism of TPEF is the endogenous fluorescent molecules found in tissues, such as the mitochondrial matrix protein nicotinamide adenine dinucleotide (NADH), flavin adenine dinucleotide (FAD), the structural proteins elastin, keratin, and collagen, and the pigments melanin. On the contrary, SHG is highly sensitive in detecting collagen fibers, a clinically relevant biomarker. TPEF, SHG, combined with coherent anti-stokes Raman scattering (CARS) can be used to generate H&E-like histopathology to differentiate BCC and SCC from normal skin [26]. In another study, TPEF was used to examine the pigmented melanoma in human *in vivo*. By using a six-axes diagnostic matrix and machine learning, benign nevi could be distinguished from melanoma with 75% sensitivity and 80% specificity [27]. A recently developed nonlinear optical imaging platform can simultaneously acquire autofluorescence, and second/third harmonic generation from a single excitation source. This technique has been successfully used to image cellular and extracellular components, and may be a promising tool in cancer research [28].

1.3.2 Spectroscopic Techniques

As mentioned earlier in this chapter, one significant aspect of optical biopsy is obtaining molecule-specific information. Molecular contrast is typically achieved by spectroscopy. Major spectroscopic techniques for cancer detection include diffuse reflectance, laser-induced fluorescence, infrared, and Raman spectroscopy.

Diffuse reflectance spectroscopy (DRS) and laser-induced fluorescence spectroscopy (LIFS) detects the optical scattering, absorption and fluorescence properties of sampled tissue. Because the physiological parameters of the tissue are associated with the progression of disease, DRS and LIFS provides a quantitative and objective

measurement for tissue diagnosis. A previous study in our lab found a significantly lower amount of scattering and higher amount of absorption parameters in cancerous lesions as compared to normal skin. The clinical DRS-LIFS system classified BCC with a sensitivity/specificity of 94%/89% [29]. In another clinical study, oblique incidence DRS system distinguished malignant melanoma with 90% sensitivity and specificity, and also classified BCCs and SCCs with 92% sensitivity and specificity [30].

Infrared (IR) and Raman spectroscopy are two major vibrational spectroscopic techniques. Although both techniques can provide chemical composition and molecular structural information in cells and tissues, their physical mechanisms are fundamentally different. Raman spectroscopy is due to the inelastic scattering of light by the molecular vibrations, while IR spectroscopy results from the absorption of light. Water is an extremely strong absorbing medium for IR spectroscopy. To bypass the water absorption obstacle, sample is commonly either sliced into micrometer sections for transmission measurements, or measured under attenuated total reflection [31]. Therefore, IR is preferably used as a visualization tool to aid pathologists in assessing tissue specimens [32]. Fourier transform IR has been successfully translated into clinic for rapid all-digital histopathology of human breast and prostate sections [33, 34].

Raman spectroscopy is first observed by Indian Nobel Laureate C.V. Raman in 1928 [35]. The first biological application was reported in 1970 [36]. Spontaneous Raman scattering is weak, and always comes with the Rayleigh scattering light and tissue autofluorescence. In the recent decades, advances in near-infrared lasers, optical filters, fiber optics and CCD cameras have greatly improved its sensitivity in detecting the chemical composition of biological tissues. For instance, Rayleigh scattering light can be well separated from Raman scattered light using a high optical density notch filter, and tissue autofluorescence can be greatly reduced by using near-infrared excitation.

Raman spectroscopy has the following advantages: First, it is highly sensitive and specific to the alternations in molecular signatures (lipids, proteins, DNA, etc.). For instance, Kochan *et al.* used Raman imaging to detect the changes of lipid droplets content

in fatty liver disease, and found that the drug treatment resulted in an increased degree of unsaturation of lipids forming droplets in a mouse model [37, 38]. Those molecular signatures can in turn be correlated with tissue pathology or physiology for diagnosis. Bergner *et al.* used Raman imaging to correlate the concentration of proteins, lipids, nucleic acids, and lipid to protein ratios with the glioma brain tumor grades [39]. Secondly, Raman spectroscopy is minimally-invasive and label-free, making it a safe and attractive tool for clinical applications. Finally, it can provide an objective diagnosis with minimum tissue processing [40, 41].

Raman spectroscopy has also been combined with other optical biopsy tools to improve diagnosis. For instance, a combination of Raman spectroscopy with reflectance confocal microscopy has been used to explore the *in vivo* water concentration profiles and natural moisturizing factor for the stratum corneum [42]. Raman spectroscopy has been combined with three label-free nonlinear imaging modalities (CARS, TPEF, and SHG) to generate H&E-like images [43]. Raman spectroscopy has also been integrated with optical coherence tomography (Raman-OCT system) to precisely visualize tissue morphology and simultaneously determine tumor type [44]. OCT image can provide an initial morphological analysis of the lesion, and then guide acquisition of biochemically specific Raman data [45, 46].

1.4 Challenges of Raman Spectroscopy in Cancer Research

Although Raman spectroscopy is promising in cancer detection, it has several well-understood shortcomings that must be overcome so that it can become a reliable and common diagnostic tool. This involves two main challenges: (1) exploring the biophysical origin of Raman detection, and (2) increasing the acquisition speed. These challenges become the motivations of this dissertation.

1.4.1 Revealing the Biophysical Origin

The first challenge of Raman spectroscopy (or optical biopsy methods in general) in cancer research is unveiling the biophysical basis of detection. For image-based

detection, the challenge exists in interpreting the images in a way that a pathologist is familiar reading. In traditional detection method, tissue samples are commonly stained using hematoxylin and eosin (H&E) stain to review by a pathologist. The hematoxylin stains the nuclei of a cell blue, and eosin stains the extracellular matrix and cytoplasm pink. However, optical imaging modalities rely on different contrast mechanisms, thus substantial training is required to read the images. To identify basal cell carcinoma from a reflectance confocal image, pathologists were trained to read five criteria, such as the presence of elongated monomorphic basaloid nuclei, increased vasculature, and prominent inflammatory infiltrate [47].

Machine learning and deep learning have opened up a new era in image-based cancer detection. Digitally stained histopathology has been developed for various optical imaging modalities. Examples are autofluorescence [48], Fourier Transform infrared spectroscopy [49], and nonlinear microscopy [50-52]. Furthermore, machine learning and deep learning make it possible to automatically classify the images for presence or absence of cancer [33, 53, 54].

In contrast, spectrum-based detection is commonly achieved by fiber probe-based approaches. To date, most fiber probe-based approaches have used statistical algorithms to describe the spectral differences of Raman spectra, such as principal component analysis (PCA) [55] and independent component analysis (ICA) [56]. However, those statistical methods are like "black box" – the principal or independent components are difficult to relate to the biophysical origin of disease, such as the microstructural organization of proteins and lipids and the functional state of cellular metabolism. These microstructural changes are what pathologists and dermatologists use to make diagnostic decisions and decide on the most appropriate treatment [57].

1.4.2 Increasing the Acquisition Speed

The fundamental limitation of spontaneous Raman spectroscopy is the small Raman scattering cross-section, which is on the order of 10^{-30} cm^2 per molecule [58].

Therefore, integration time needs to be long enough to generate a Raman spectrum with acceptable signal-to-noise ratio. The typical integration time is ~1s for tissue. Using higher laser power can reduce the integration time, but may lead to tissue damage.

One solution is to use Raman optical fiber probe for large-volume screening. The sampling volume is typically on the order of mm^3, but can vary depending on the probe design. For instance, the sampling depth of spatially offset Raman spectroscopy in on the order of cm, while a confocal probe is on the order of 10 – 100μm [59]. Raman optical fiber probe is preferably used in pointwise sampling mode rather than the imaging mode. Raman optical fiber probe has allowed for fast and accurate cancer diagnostics, including *ex vivo* study of breast [60, 61], prostate [62], lung [63] and skin [64, 65], and *in vivo* study of breast [57], cervical [66], and skin [4, 67].

Another solution is to use coherent Raman scattering (CRS) microscopy to for rapid label-free imaging. Different from spontaneous Raman scattering, which depends on spontaneous interactions, the Raman processes in coherent Raman scattering are driven coherently, leading to an enhancement of the scattering signals by several orders of magnitude [68]. Two types of coherent Raman scattering have been developed favorably for biomedical applications: coherent anti-stokes Raman scattering (CARS) [69], and stimulated Raman scattering (SRS) [70]. While spontaneous Raman scattering involves only a pump beam as the excitation source, coherent Raman scattering involves both the pump beam and Stokes beams, where the difference in frequency between the two beams is tuned to match molecular vibrations of interest [58].

CARS is commonly combined with second harmonic generation and multiphoton fluorescence to generate label-free chemical imaging. By using intrinsic signals from CH_2 and CH_3 vibrations of lipids and protein, high resolution images can be generated for various tissue types, including brain [71, 72], skin [26, 73], lung [74], and liver [75, 76]. An *in vivo* CARS endoscope has been developed for real-time histopathology diagnosis [77].

SRS is developed more recently and offers further several advantages over CARS: (1) it does not have non-resonant background; (2) the Raman spectrum is identical to spontaneous Raman spectrum, but with a much narrower range; (3) the signal and concentration of target molecules have a linear relationship [78]. One highlight of *in vivo* SRS is its application to brain tumor margin assessment [79]. A 97.5% sensitivity and 98.5% specificity were achieved in detecting brain tumor infiltration in human [80]. SRS microscopy built upon fiber laser source also has the promise to facilitate the use for clinical applications [81, 82].

Spontaneous Raman spectroscopy allows for acquiring full spectrum content, and has much simpler and less inexpensive setup. Therefore, techniques have also been developed upon spontaneous Raman spectroscopy for rapid measurement. Examples to speed up spontaneous Raman acquisition include line-scan [83], wide-field imaging [84], Weiner estimation [85], multi-focal array [86], and DuoScan [87]. Line-scan Raman spectroscopy used cylindrical lens to generate a uniform laser line of approximately 100 μm [83], and simultaneously record the Raman spectra on the line using a two-dimensional imaging sensor [88, 89]. Wide-field Raman spectroscopy used a fiber bundle array as the collection fibers combined with a tunable filter to generate fast images [84]. Weiner estimation method could rapidly reconstruct full Raman spectrum at each pixel of the Raman narrow-band image. Multi-focal array method used micro-lens [90], scanning galvanometer mirrors [86], or spatial light modulator [91, 92] to generate multipoint illumination. DuoScan method generated a square illumination by continuously scanning the laser beam, and was used to characterize human bone composition [93].

1.5 OVERVIEW OF DISSERTATION STUDY

The goal of this dissertation is to study the potential of Raman spectroscopy in improving the clinical diagnosis of skin cancer. We addressed two main challenges of Raman spectroscopy in cancer research as mentioned in **Chapter 1.4**: we explored the biophysical origin of accurate melanoma and nonmelanoma skin cancer detection, and we expedited Raman acquisition for rapid skin cancer surgical margin assessment.

In an effort to explore the biophysical origin, we proposed a biophysical human skin cancer model in **Chapter 2**. Our model is innovative because the model components are *in situ* skin constituents extracted from fresh human skin sections spanning normal and various disease states. In order to extract *in situ* skin constituents, we built a custom confocal Raman microscope integrated with a reflectance confocal microscope. **Chapter 2** resulted in eight Raman active biomarkers to describe the spectral differences of various skin pathologies.

In **Chapter 3**, we applied our biophysical model for the first time to an *in vivo* clinical melanoma dataset. Our lab has previously developed a fiber-probed based clinical system [94], and achieved high accuracy in detecting malignant melanoma from benign nevi [67]; however, the biophysical origin of accurate *in vivo* melanoma detection remains unclear. One of our key findings is that collagen and triolein are the most relevant diagnostic markers to discriminate melanoma from benign nevi. Our results would increase fundamental knowledge of cancer processes as well as lay the groundwork for improving the diagnostic performance of the technology.

In **Chapter 4**, we explored the biophysical basis of *ex vivo* nonmelanoma skin cancer surgical margin detection. Although previous studies have demonstrated that confocal Raman microscope is highly accurate in detecting the tumor margins of basal cell carcinoma, the biophysical basis of this accurate detection remains unclear. Therefore, we discovered the most relevant diagnostic markers for accurate discrimination of basal cell carcinoma from surrounding normal tissues. The biophysical changes derived from our model was consistent with histopathological diagnosis.

Chapter 5 describes a superpixel acquisition method to overcome the technical hurdle of traditional Raman imaging in speed. We then applied this method for the first time to rapid skin cancer surgical margin assessment. Our findings suggest that Raman spectroscopy is a promising surgical guidance tool for identifying tumors in the resection margins.

We conclude this dissertation in **Chapter 6.**

Chapter 2: Establishing a Raman biophysical inverse model for skin cancer detection[1]

2.1 INTRODUCTION

This chapter describes a novel Raman "biophysical model" of human skin cancer. The morphological and biochemical composition of skin tissue are derived from the model, and then used to classify skin cancers.

Previous biophysical models used model components either measured directly from synthetic/purified chemicals [65, 95-98], or extracted from tissue sections *in situ* [39, 99, 100]. The advantage of using synthetic/purified chemicals as model components is that they can be easily measured without the need for Raman imaging. This concept has been applied successfully to a previous Raman model of excisional skin biopsies [65] and has given us some prior knowledge about skin composition. Other groups used *in situ* constituents to build biophysical models of other disease processes, such as coronary atherosclerosis [99], breast cancer [100], and brain tumor [39].

Here, we expand upon this approach by developing a biophysical human skin model using *in situ* skin constituents. *In situ* constituents better represent the milieu of biological tissues that cannot be recapitulated in a synthetic environment. In human skin many constituents are present in various forms and each has a slightly different Raman spectrum. For instance, both collagen type I and III are abundant in human dermis; however, if both of them are included in the model, it may lead to overfitting and unstable results. In addition, skin constituents synthesized in the lab or from commercial sources are not in their natural states as in the human skin. For instance, the Raman features of a protein may change when it is exposed to organic solvents during synthesis. As a result, a single spectrum of skin constituent extracted from its microenvironment can provide a more

[1]Portions of this chapter are adapted from X. Feng, A. J. Moy, H. T. Nguyen, J. Zhang, M. C. Fox, K. R. Sebastian, J. S. Reichenberg, M. K. Markey, and J. W. Tunnell, "Raman active components of skin cancer," Biomedical optics express **8**, 2835-2850 (2017).

general picture of the biophysical origins of skin spanning normal and abnormal disease states.

Furthermore, we applied the model for the first time to *in vivo* human skin cancer screening data that covers a wide range of normal, nonmelanoma and melanoma skin cancers and precancers [67]. Previous Raman models of human skin were either built for *ex vivo* tissue specimens [65] or *in vivo* normal skin [101]; however, Raman biophysical models have not been applied to *in vivo* skin cancer screening to interpret biophysical changes between pathologies.

In this chapter, we performed Raman imaging of tissue sections using a custom confocal Raman microscope. Multivariate curve resolution (MCR) analysis [102] was used to resolve *in situ* skin constituents from Raman images. Our results suggest that eight skin constituents are the most relevant building blocks, illustrating some variances with their corresponding synthetic components. The basis spectra of those skin constituents were then combined linearly to describe *in vivo* human skin spectra. The fit coefficients provided insight into the biochemical and structural composition of normal, benign and malignant skin tissues. Our model revealed the most important skin constituents representing the spectral features of skin tissues, and provided significant guidance to develop diagnostic algorithms for real-time noninvasive skin cancer diagnosis in future.

2.2 MATERIALS AND METHODS

2.2.1 Raman Instrumentation

Raman images were collected with a custom-built confocal Raman microscope illustrated in **Figure 2.1**. The system was also integrated with a reflectance confocal microscope (RCM) and a bright-field microscope, which provided the morphology image for assisting in locating the region of interest for Raman imaging.

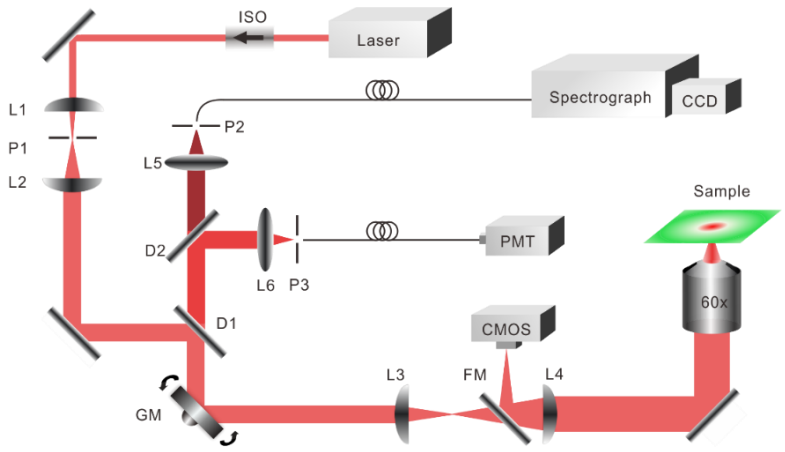

Figure 2.1: Schematic of confocal Raman and confocal laser-scanning microscope used for skin measurements. The flip mirror and CMOS camera were used for bright-field imaging. ISO, isolator; D1, D2: dichroic mirror; P1 – P3: pinhole; L1 – L6, lens; GM, galvanometer mirror; FM, flip mirror.

The Raman excitation source was an 830nm single mode diode laser (LM830-PLR200, Ondax). The laser beam was reshaped, expanded and delivered to the sample through a microscope objective (Olympus, NA = 1.2, 60x). The galvanometer mirror performed 2D raster scanning on the tissue. The backscattered Raman signal was collected by a spectrograph (f/1.8i, Kaiser) and a deep cooling CCD camera (IDUS, Andor) through an optical fiber (50 μm, NA=0.22), which also acted as a pinhole. The Rayleigh scattering light was collected by a PMT (C10709, Hamamatsu), and amplified by a current preamplifier (SR570, Stanford Research Systems). A data acquisition board (PCIe-6351, National Instruments) and LabVIEW software (National Instruments) were used to control the system. The power delivered to the sample was approximately 45mW. Lateral resolution was measured from the FWHM (full width at half maximum) of the point spread function using 0.2 and 0.5 μm microbeads. Axial resolution was measured from the FWHM of the intensity profile by translating a mirror towards the objective. The lateral, axial and

spectral resolution of the Raman system was around 1 μm, 8 μm and 8 cm^{-1}, respectively. A more detailed characterization of the system can be found in **Appendix A**.

2.2.2 Tissue Preparation and Raman Imaging

Our study was approved by the Institutional Review Board at The University of Texas at Austin and Seton Medical Center. Fresh frozen human skin tissue samples were acquired from biopsy specimens during routine skin cancer surgery at Austin Dermatologic Surgery Center. After being transferred to the lab, the samples were stored at -80C. They were then thawed to -22C in a cryostat and sliced into 10 μm thin sections. The sections were transferred to magnesium fluoride slides (Edmund Optics) for the Raman measurement, and serial sections were transferred on standard microscope slides for hematoxylin and eosin (H&E) staining. Prior to Raman imaging, the sections were warmed to room temperature and kept moisturized with 0.9% saline solution.

Next, we performed Raman imaging on skin sections. Typical integration time at each pixel location was 2s. Typical step size in both the x and y directions was 1μm, but sometimes to achieve a large of view a step size of 5 μm was used. Imaging area varied from 30×30 μm^2 to 150×150 μm^2. We then correlated the Raman image with the histopathology image of the serial stained section. A board-certified dermatologist assisted in identifying and confirming the morphology and biochemical components measured. In total, we collected more than 40 Raman images from samples of different disease states, including 24 images from 11 basal cell carcinoma (BCC) patients, 15 images from 5 squamous cell carcinoma (SCC) patients and 4 images from 1 malignant melanoma (MM) patient.

2.2.3 Data Preprocessing and MCR Analysis

Raman data preprocessing was performed using MATLAB (R2015b, MathWorks). All spectra underwent wavelength calibration, background subtraction, cosmic ray removal and smoothing. The system spectral response was calibrated using a tungsten halogen lamp

(LS-1-CAL, Ocean Optics). The fluorescence background was then removed by modifying a 5th order polynomial fitting routine [103]. The effective spectral range was 800 to 1800 cm^{-1}.

A multivariate curve resolution (MCR) method was employed to resolve individual morphological or biochemical components from the Raman image. This method has been successfully applied to stimulated Raman imaging data by Zhang *et al*. [104]. The basic concept of MCR is to decompose the raw spectra matrix *D* (unfolded from Raman imaging) into the product of two smaller matrices *C* and S^T by a bilinear model:

$$D = C \cdot S^T + E \quad \textbf{(2.1)}$$

S^T corresponds to the matrix of the pure spectra, C is the related concentration profiles for each of the components and *E* is the error matrix. As an unsupervised learning method, the number of components contributing to D was determined either by prior knowledge or by assessing the results obtained using singular value decomposition (SVD). After initial estimation is given for S^T, the C and S^T are optimized iteratively using an alternative least-squares algorithm (ALS) until convergence is reached.

Here, we used a MATLAB based MCR-ALS toolbox [102] to determine C and S^T. The initial estimates of C and S^T were determined by means of a purest variable detection method [105]. The basic idea is to resolve highly overlapping near-infrared spectra with baseline problems by using the second-derivative spectra [105]. A nonnegative constraint and a 10% of tolerance were added to the ALS optimization. The concentration images for each individual component were reconstructed from C, and the corresponding basis spectra were obtained from S^T. We then categorized the basis spectra according to their biochemical or structural origin, such as elastic fibers, collagen fibers and cell nucleus.

We obtained a library of basis spectra from various skin sections spanning normal skin, and various skin disease states. The spectra in the same category were then averaged

to create a single basis spectrum to represent that biochemical or structure. Although the basis spectra collected from different patients had minor differences, after averaging spectra from many patients we could ensure that the inter-patient variation was minimized.

2.2.4 Clinical Screening Data Description

In vivo human skin spectra came from our previous skin cancer screening study [67]. Data were collected from an optical fiber probe [106] integrated in a multimodal spectroscopy system [94] on different sites, such as scalp, nose, earlobe, shoulder and thigh. Lesion types including basal cell carcinoma (BCC, 19 lesions), squamous cell carcinoma (SCC, 38 lesions), actinic keratosis (AK, 14 lesions), benign pigmented lesion (PL, 17 lesions) and malignant melanoma (MM, 12 lesions). BCC and SCC are the most common types of nonmelanoma skin cancers, whereas AK and PL are the most common precancers of SCC and MM, respectively. Raman spectra of adjacent normal skin for each individual lesion were also collected. Although normal skin measurements were not verified by histopathology, they were visually verified to be normal by an experienced dermatologist/physician assistant.

2.2.5 Model Establishment

A sample's Raman spectrum can be represented as a linear combination of the Raman spectra of the sample's individual constituents. The signal intensity is then proportional to the chemical concentration [107]. Therefore, if one knows the spectra of the basis tissue constituents *a priori*, one can determine the concentration of those basis constituents. We used linear least-squares fitting with a nonnegative restraint for model fitting, according to the following equation:

$$X = c \cdot s + e \qquad \textbf{(2.2)}$$

While X is the sample's spectrum (*in vivo* human skin spectrum). s is the spectra matrix of the sample's individual constituents. c is the relative spectral contribution (fit parameter) predicted by the model. e is the noise related with the clinical Raman system. Next, a combination of forward selection and backward elimination methods was performed to derive the most relevant basis constituents to the spectroscopic model. Finally, after applying the model to all the *in vivo* human skin data, we could obtain the biochemical and structural makeup of tissues spanning normal and various disease states.

One important factor that may influence the performance of the model is collinearity of the basis spectra. Collinearity is a common issue in linear regression that may lead to an unstable result [108]. The following equation is to calculate the collinearity coefficients R between two basis spectra, x and y:

$$R = \frac{x^T y}{(x^T x)(y^T y)} \tag{2.3}$$

A value of 0 means the two basis spectra x and y do not have collinearity, and 1 indicates the two vectors are the same. This equation was used for the initial evaluation of the model components.

2.3 RESULTS

2.3.1 Extraction of Primary Skin Constituents *in Situ*

The basis spectra were categorized into: (1) cellular components, (2) epidermal extracellular matrix (ECM), (3) dermal ECM, (4) lipids, (5) pigments, and (6) miscellaneous. We will illustrate each category in the following part of this section.

2.3.1.1 Cellular Components

To identify cellular tumor components, Raman imaging was performed within a tumor cluster in a BCC section (**Figure 2.2**). Using MCR analysis, we reconstructed three concentration images (**Figure 2.2** a-c) corresponding to cell nucleus, cell cytoplasm, and the Raman substrate. Those structures correlated well with the bright field, RCM, and histopathology images (**Figure 2.2** d-f), and their Raman spectra had similar characteristic peaks with the known spectra measured from the pure chemicals (**Figure 2.2**). This approach was used to resolve the other skin constituents in the following sections as well. As seen from the plots on the right, the basis spectra of *in situ* nucleus and synthetic DNA (Sigma-Aldrich) are similar, which both have the pronounced contribution from phosphodioxy group PO_2^{-1} at 1093 cm^{-1}. However, the difference spectrum shows that *in situ* nucleus has substantial differences from synthetic DNA. For example, *in situ* nucleus appears to have a higher contribution from DNA backbone at 835 cm^{-1} [109].

The spectra of *in situ* cytoplasm and synthetic actin also have high similarity, but major differences can be found at 1003 cm^{-1} phenylalanine peak, 1081 and 1092 cm^{-1} lipid band. Numerous other peaks can also be appreciated in the difference spectra. These differences indicate the morphologically derived basis spectra of nucleus and cytoplasm include features related to other elements found in the cell.

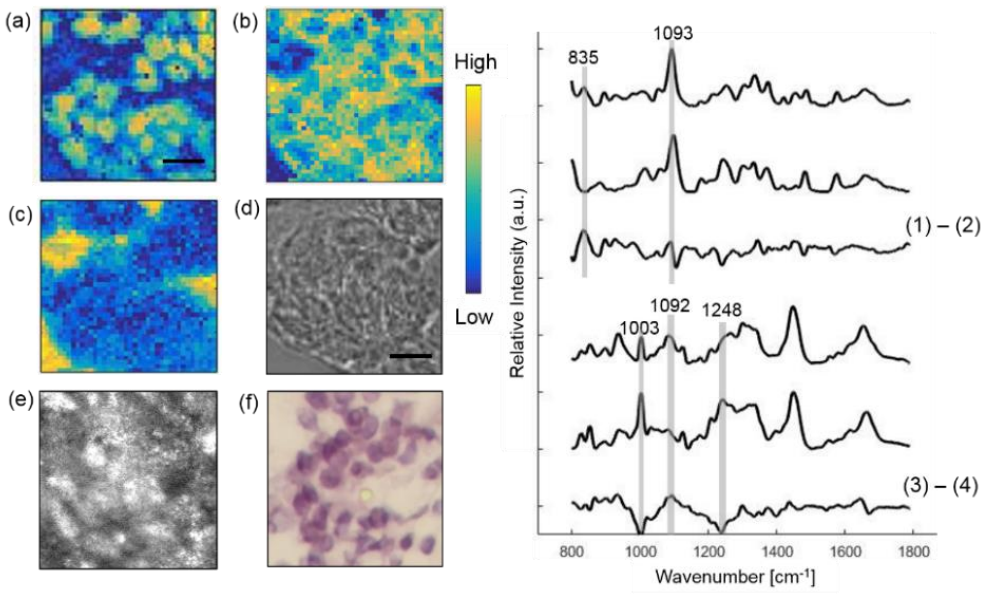

Figure 2.2: Extracting cellular components from a BCC lesion. Raman images of nucleus (a) and cytoplasm (b) and Raman substrate (c) are compared with bright-field image (d), RCM image (e) and histopathology image (f). The boxes on (e) and (f) mark the location of Raman imaging. The contrast of the RCM image was provided by the relative difference in refractive index of cells and the surrounding stroma. Plots on the right show Raman spectra of *in situ* nucleus, synthetic DNA and their difference spectrum. Also *in situ* cytoplasm, synthetic actin and their difference spectrum. Scale bar: 10 μm.

2.3.1.2 Epidermal ECM

The epidermal layer of skin provides the barrier to water permeation and abrasion resistance. It is produced by continuous cell division of keratinocytes in the basal layer. Ultimately, the keratinocytes cornify and produce the stratum corneum, which is the dead, flattened cells at the outermost layer of the skin [110]. Because keratin is the main chemical component of epidermal ECM, we use *in situ* keratin to represent epidermal ECM.

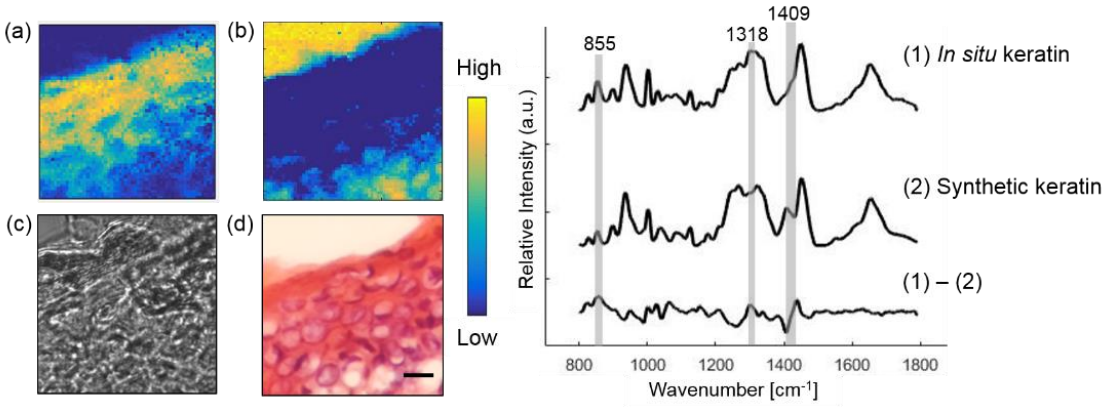

Figure 2.3: Extracting the epidermal component from a normal skin section. Raman images of *in situ* keratin (a) and Raman substrate (b) are compared with bright-field image (c) and histopathology image (d). Plots on the right show Raman spectra of *in situ*, synthetic keratin and their difference spectrum. Scale bar:10 μm.

Figure 2.3 illustrates Raman imaging performed on epidermis from a normal skin section. Tissue architecture correlates well with the histopathology image. The concentration images of epidermal ECM and the Raman substrate were reconstructed using MCR analysis. The Raman spectra of *in situ* and synthetic keratin are similar with substantial differences found at the protein bands at 855, 1318 and 1409 cm^{-1} [111].

2.3.1.3 Dermal ECM

Dermal ECM comprises fibrillar collagens and associated proteins. Collagen fibers account for about 70% of the weight of dry dermis, while elastin maintains skin elasticity through a durable cross-linked array. Large diameter elastin-rich elastic fibers reside in the reticular dermis [112].

Figure 2.4 illustrates Raman imaging performed on a BCC skin section to extract dermal ECM proteins. The *in situ* collagen (collagen fiber), *in situ* elastin (elastic fiber), dye, and Raman substrate were resolved from the image by MCR analysis. The thin blue-gray elastic fibers and the pink collagen fibers can be identified from the histopathology image. The plots on the right compares the Raman spectrum of *in situ* collagen with synthetic type I and III collagen. Major differences are found at 856, 1248 and 1665 cm^{-1} protein bands between *in situ* and type I collagen, and 1157 and 1514 cm^{-1} between *in situ* and type III collagen. *In situ* and synthetic elastin have very similar spectra, which indicates that elastin is the major chemical component of elastic fibers.

2.3.1.4 Lipids

Skin's epidermal surface is comprised of sebaceous and stratum corneum lipids. Epidermal lipids act like a cement to fill the spaces between the cells. The major constituents of sebaceous lipids are triglycerides (triolein), wax esters and squalene, while the epidermal lipids are a mixture of ceramides, free fatty acids and cholesterol [42, 113]. Ceramide is an important epidermal surface lipid as it composes almost half of the SC lipids [110].

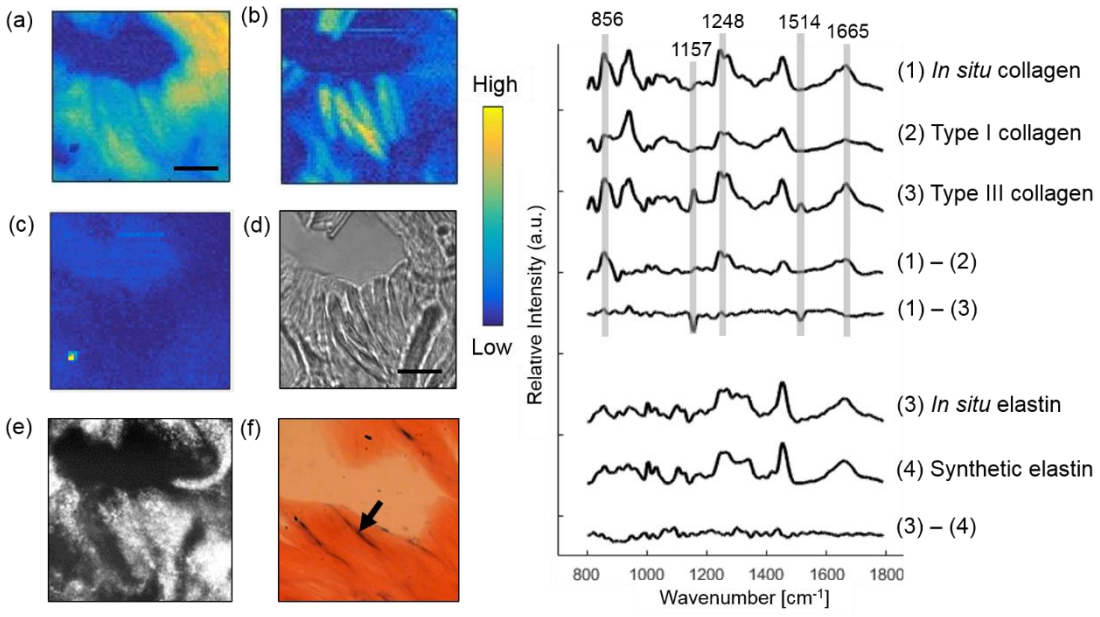

Figure 2.4: Extracting dermal components from a BCC skin section. *In situ* collagen (a) and elastin (b) are resolved from the image. The dye used by the dermatologist to mark the orientation of the tissue was also detected (c). Raman images are compared with the bright-field image (d), RCM image (e) and histopathology image (f). The box on (e) marks the location of Raman imaging. The arrow in (f) points to a thin blue-gray elastic fiber. Plots on the right displays Raman spectrum of *in situ* collagen, synthetic collagen and the difference spectrum. Also Raman spectrum of *in situ* elastin, synthetic elastin, and their difference spectrum. Scale bar: 10 μm.

Raman imaging was also performed to derive the basis spectra of lipids. **Figure 2.5** illustrates extracting *in situ* ceramide and triolein within a hair follicle from a SCC skin section. The synthetic spectra are not shown because they look similar to *in situ* spectra. Instead, we compare the difference spectra between *in situ* lipids. Although *in situ* ceramide and palmitic acid look similar, they have different spectral intensity in C-C stretching mode

at 1063 and 1128 cm^{-1}, CH_2 twisting mode at 1296 cm^{-1}, CH2 bending mode at 1440 cm^{-1} and C=C stretching mode at 1656 cm^{-1}. Larger variance was observed in those bands between *in situ* ceramide and triolein. Triolein is not only abundant in skin lipid, but also in subcutaneous fat [100]. As triolein has a very strong Raman scattering cross-section, it contributes greatly to Raman spectrum of human skin.

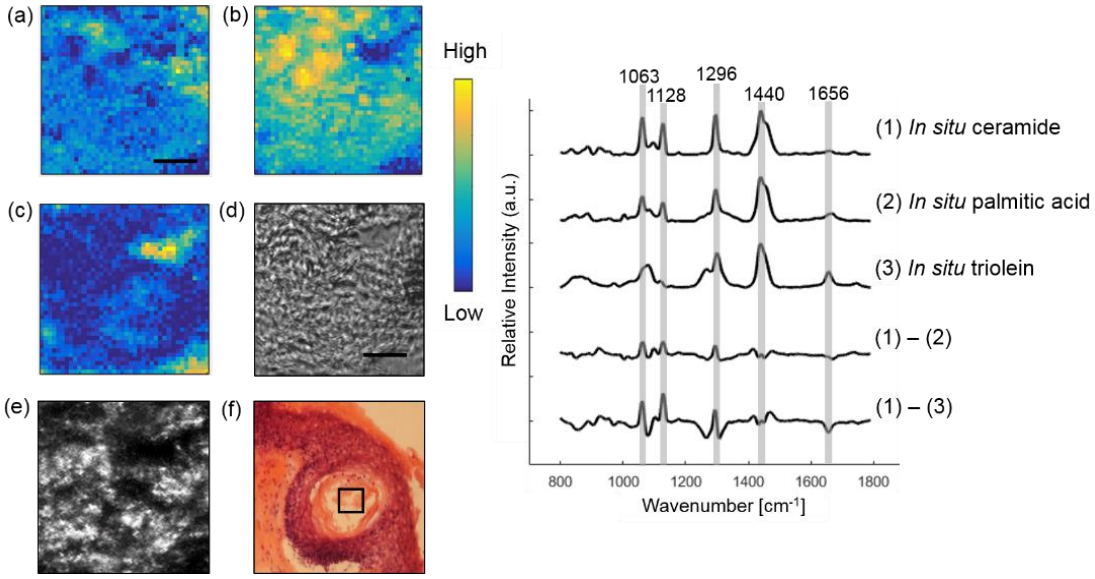

Figure 2.5: Extracting lipids within a hair follicle from a SCC skin section. *In situ* ceramide (a), triolein (b) and Raman substrate (c) are resolved from the image. Raman images are compared with the bright-field image (d), RCM image (e) and histopathology image (f). Some lipids in (f) were lost during the staining processing. The box on (e) and (f) marks the location of Raman imaging. Difference spectrum between *in situ* ceramide and palmitic acid and difference spectrum between *in situ* ceramide and triolein are also shown. Scale bar: 10 μm.

2.3.1.5 Pigments

Skin pigments include melanin and beta carotene. Melanin is produced by melanocytes in the basal layer of the epidermis. In **Figure 2.6**, we identified melanin from a MM skin section. As expected, melanin provides strong contrast in RCM image [114]. We lowered the laser excitation to 20mW to reduce tissue burning caused by strong absorption of melanin. As this led to a worsening in the SNR, we further smoothed the melanin spectrum by fitting it to Gaussian functions [115]. The two broad peaks located at 1378 cm^{-1} and 1573 cm^{-1} were consistent with the spectrum of *in vivo* cutaneous melanin [115]. Beta carotene is a plant-derived carotenoid. It was extracted from skin sections adjacent to fatty tissue. The characteristic peaks of beta carotene at 1008, 1156 and 1515 cm^{-1} are consistent with a previous study [116].

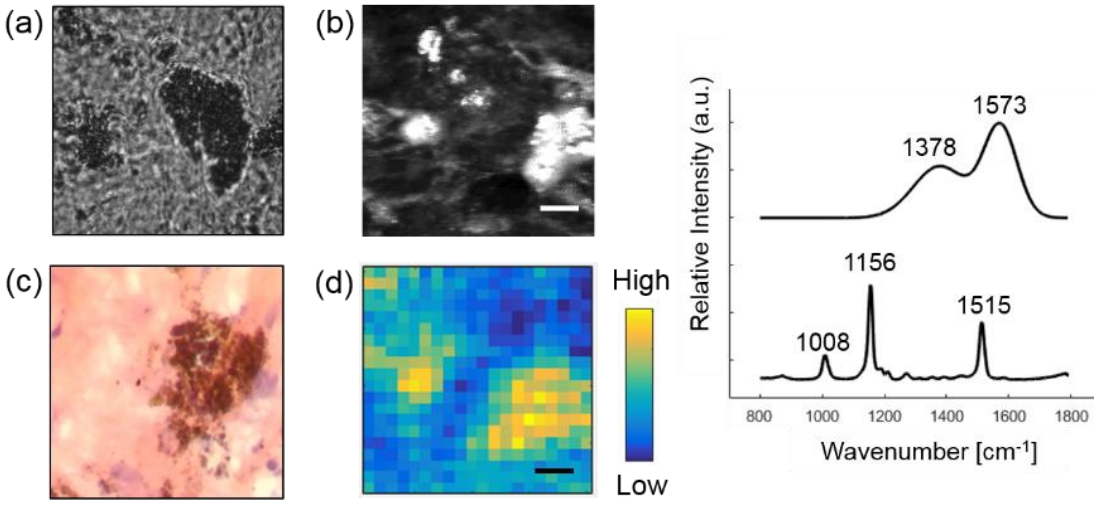

Figure 2.6: Extracting melanin from a MM skin section. Raman image of melanin (d) are compared with bright field image (a) RCM image (b) and histopathology image (c). Basis spectra of melanin and beta carotene are shown on the right. Scale bar: 50 μm.

2.3.1.6 Miscellaneous

In Raman imaging, water came from the saline used to keep the skin section moist. We found water plays an important role in fitting the broad Raman band at 1645 cm^{-1}. Hemoglobin and calcium hydroxyapatite (CaH) were only detected in one skin section but were included in our library. Morphologies such as hair follicle (HF) and keratin pearl (KP) were also obtained. KP was extracted from SCC lesions with acceleration of keratinization. **Figure 2.7** shows the basis spectra of these constituents. Although the spectra of HF and KP are similar, the difference spectrum suggested that the former contained cellular information (DNA backbone at 835 cm^{-1} and phosphodioxy group PO_2^{-1} at 1093 cm^{-1}). Finally, we included a spectrum of fiber background generated from the Raman optical fiber probe. This component is used to fit the broad peak between 1000 – 1100 cm^{-1} in the *in vivo* data.

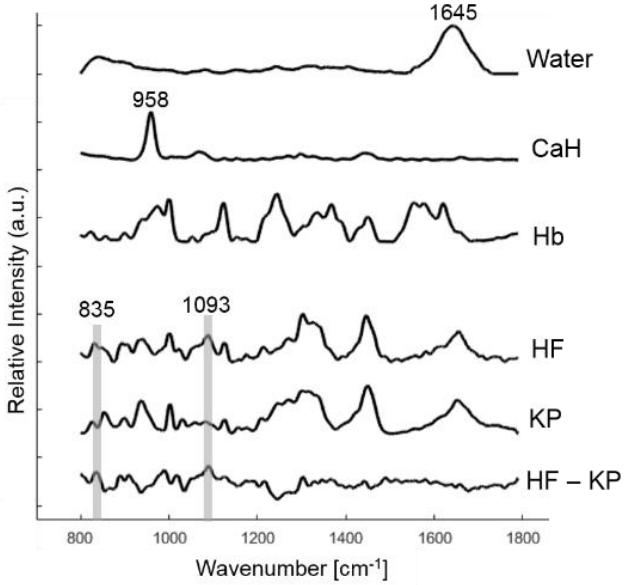

Figure 2.7: Basis Raman spectra of water, calcium hydroxyapatite (CaH), hemoglobin (Hb), hair follicle (HF) and keratin pearl (KP) collected *in situ* are displayed. The difference spectrum between HF and KP is also shown.

2.3.2 Biophysical Modeling Results

A total of fifteen candidate model components were derived. The basis spectra were peak normalized with a minimum value of 0 and maximum value of 1. Their collinearity coefficients are displayed in **Table 2.1**. Beta carotene and calcium hydroxyapatite are not shown because they have low collinearity (< 0.50) with other components. Several components have high collinearity, such as *in situ* keratin in epidermis, keratin pearl (KP), and hair follicle (HF), likely because keratin dominates their chemical composition. As a result, we selected only one model component to represent keratin. In addition, we observed high collinearity between cell cytoplasm (Cyt) and other protein-rich components (elastin (Ela), keratin, KP, and HF). These components share common features of many functional groups, such as C-C stretching around 939 cm^{-1}, Amide III around 1270 cm^{-1}, CH modes around 1454 cm^{-1} and amide I around 1660 cm^{-1}. Considering that (1) cell cytoplasm has a much smaller Raman scattering cross-section and less quantity than keratin, and (2) the spectrum of keratin may contain some cell features due to their close proximity, we finally excluded cytoplasm from our model. In addition, Raman spectrum of palmitic acid (PA) has a high degree of overlap with triolein (0.94) and ceramide (0.96), so PA was also excluded from the model. In total, we arrive at eight primary Raman active components: collagen, elastin, triolein, cell nucleus, keratin, ceramide, melanin and water (**Figure 2.8**). The peak positions of main Raman bands are displayed in **Table 2.2**.

Table 2.1: Collinearity measurement for candidate model components[a].

		Col	Ela	Ker	KP	HF	Cyt	Nuc	Trio	Cer	PA	Mel	Hb	Water
	Col	1.00												
	Ela	0.89	1.00											
(a)	Ker	0.88	**0.93**	1.00										
	KP	0.86	**0.94**	**0.97**	1.00									
	HF	0.77	**0.90**	**0.94**	**0.95**	1.00								
(b)	Cyt	0.86	**0.93**	**0.95**	**0.97**	**0.95**	1.00							
	Nuc	0.64	0.76	0.70	0.75	0.78	0.77	1.00						
	Trio	0.70	0.78	0.82	0.82	0.84	0.86	0.59	1.00					
(c)	Cer	0.56	0.62	0.66	0.66	0.70	0.72	0.44	0.85	1.00				
	PA	0.65	0.75	0.79	0.79	0.82	0.83	0.51	**0.94**	**0.96**	1.00			
(d)	Mel	0.47	0.58	0.56	0.61	0.56	0.57	0.48	0.39	0.33	0.42	1.00		
(e)	Hb	0.64	0.73	0.68	0.72	0.67	0.69	0.61	0.41	0.34	0.44	0.78	1.00	
	Water	0.56	0.58	0.58	0.65	0.57	0.62	0.48	0.33	0.20	0.29	0.55	0.60	1.00

[a]Components are sorted according to their major composition: (a) protein, (b) cell, (c) lipid, (d) pigment, (e) miscellaneous. Components include collagen (Col), elastin (Ela), keratin (Ker), keratin peal (KP), hair follicle (HF), cell cytoplasm (Cyt), cell nucleus (Nuc), triolein (Trio), ceramide (Cer), palmitic acid (PA), melanin (Mel), hemoglobin (Hb) and water.

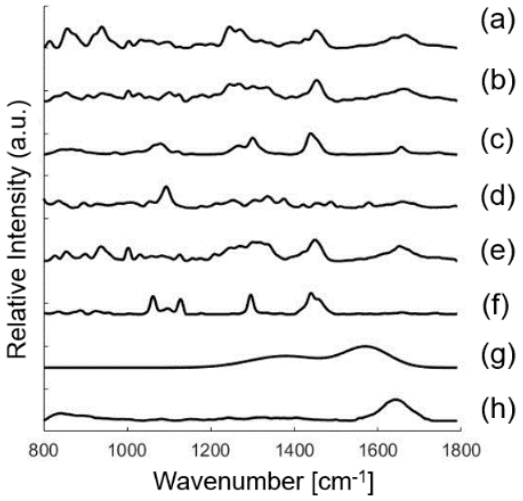

Figure 2.8: Basis spectra used in the biophysical model of skin. Model components include collagen (a), elastin (b), triolein (c), nucleus (d), keratin (e), ceramide (f), melanin (g), water (h).

Table 2.2: Peak positions of main Raman bands in the Raman active components.

Raman peaks [cm^{-1}]	Band assignments	Components
835	DNA backbone: O-P-O/ tyrosine	nucleus
855	CCH bending (aromatic) of protein	elastin, keratin
856	C-C vibration of the collagen backbone	collagen
937	C-C stretching of proline and valine and protein backbone	keratin
940	C-C stretching of protein backbone	collagen, elastin
1003	C-C vibration of phenyl ring	collagen, elastin, keratin
1063	C-C asymmetric skeletal stretching of lipids (trans-conformation);	ceramide
1080	C-C skeletal stretching	triolein
1093	O-P-O symmetric stretching vibration of the DNA backbone	nucleus
1128	C-C symmetric skeletal stretching	ceramide
1248	Amide III (β-sheet and random coil conformations)	collagen, elastin
1254	β sheet/ thymine/ cytosine (DNA base/ DNA & RNA base)	nucleus
1269	Amide III (α-helix conformation), C-N stretching, N-H in-plane bending	collagen, elastin, keratin
1301	C-H modes (CH2 twisting and wagging) of lipids; CH2/CH3 bands	triolein
1336	desmosine/isodesmosine	elastin
1337	adenine, guanine (DNA & RNA base)	nucleus
1378	linear stretching of the C-C bonds within the rings	melanin
1440	CH2/CH3 bands	triolein, ceramide
1450	C-H bending of proteins	keratin
1454	C-H stretching, C-H asymmetric deformation	collagen, elastin
1573	in-plane stretching of the aromatic rings	melanin
1645	O-H bending mode of liquid water	water
1653	C-O stretching model of amide I	keratin
1656	C-C lipids	triolein
1665	C-O amide I vibration	collagen, elastin

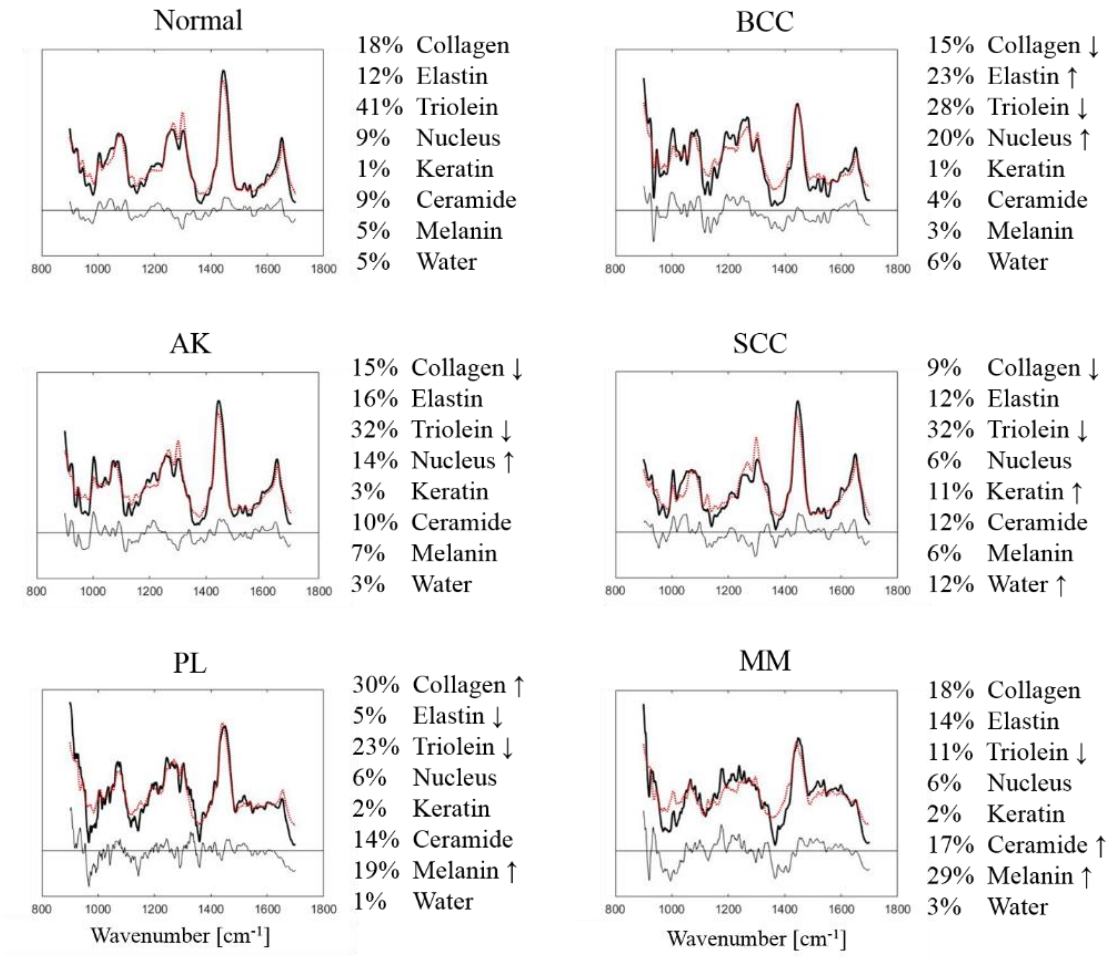

Figure 2.9: Model fitting results for *in vivo* human skin spectra categorized as Normal, BCC, SCC, AK, PL and MM. Mean Raman tissue spectra (solid lines), model fits (dotted lines), residuals are plotted on the same scale. Fit coefficients in percentage are listed on the right. The arrow indicates the most characteristic changes for each lesion type.

In an effort to validate that these eight components captured the primary skin constituents as measured on *in vivo* human skin cancers, we fit this linear component model to the clinical data set. We determined the relative contribution from the eight model

components of each of the pathology groups. **Figure 2.9** shows the fitting result of the mean Raman spectra. Considering the order of magnitude of the residuals with respect to the bulk tissue spectra, most of the spectroscopic features are well represented. The fit coefficients across each model component are normalized to sum to 1.

The results illustrate key biophysical changes of skin with different tissue types. For instance, normal skin has an average of 41% triolein, 30% of dermal ECM (collagen and elastin), and minor contribution from nucleus, ceramide, melanin and water. However, the contribution of triolein drops significantly from normal skin (41%) to nonmelanoma skin cancer/precancer (BCC, SCC, AK) (28%, 32%, 32%) and to MM, PL (11%, 23%). As expected, melanin content is much higher in MM (29%) and PL (19%) compared to other tissue types (3 – 7%). In addition, keratin concentration is higher in SCC (11%) as compared to other tissue types (1 – 3%).

2.4 DISCUSSION

In this chapter, we establish a Raman "biophysical model", an inverse model for determining biophysical skin components using *in vivo* Raman spectroscopy. We built a confocal Raman microscope to identify eight of the most relevant skin constituents contributing to the spectral differences among different skin malignancies.

Our model components were found to be consistent with previous studies. Some were commonly used in skin and non-skin models. For instance, collagen and triolein are known to be important contributors to the Raman signal of breast, gastric, and artery tissues [97, 99, 100]. We demonstrated these two components also played an important role for fitting *in vivo* skin data. Other components were more specific to skin. For instance, Caspers *et al.* used ceramide to model epidermal lipid in human stratum corneum layer [117]. Silveira *et al.* included elastin to model skin dermal protein [65]. Keratin was important for *in vivo* skin to consider the impact of epidermis [101, 117] but not necessary for excisional skin fragments because the measurement was on the dermis side [65].

Melanin was important only when pigmented lesions were considered, so it was used to model melanoma skin tissue [65].

However, our model is different from previous biophysical Raman skin models in the following two aspects. First, we used skin constituents in their microenvironment as the basis spectra. Our results showed that it was possible to use a single morphologically derived basis spectrum rather than synthetic/purified chemicals. As demonstrated in the Results section, *in situ* skin constituents had substantial differences from their corresponding synthetic chemicals, even if their major chemical components were the same. Since *in situ* constituents are extracted from skin in their natural state, without any further processing, they can better represent the skin microenvironment that cannot be recapitulated in a synthetic environment. Second, our model was validated by a previous *in vivo* clinical screening study [67] acquired by a Raman optical fiber probe [106]. Currently, the only biophysical Raman skin cancer model was based on excised fragments of BCC and melanoma skin tissues [65]. We expanded upon this research to apply our model to *in vivo* skin spectra study and covered a wider range of nonmelanoma and melanoma skin cancers and precancers.

While we found a total of 15 measurable Raman components in skin, we found the most consistent model outcomes were achieved when minimizing this number to only eight components. Our approach was to select only one Raman constituent to represent those *in situ* components that were chemically similar and with high collinearity. Similarly, Stone *et al.* demonstrated that including both amino acids and the proteins containing them in a linear model skewed the fit coefficients [96]. Our experience is that minimizing the number of protein components resulted in the most consistent fit coefficients.

The biophysical changes of skin derived by our model follow known morphological and biochemical changes in skin malignancy. We observed that there is less triolein in skin cancer/pre-cancer lesions relative to the amount of triolein in normal skin. Triolein is a major form of triglyceride in human skin, which presents as subcutaneous fat and epidermal surface lipid. The apparent decrease in triolein as cancer progresses could be due

to: (1) the reduction of subcutaneous fat sampled by the probe, caused by the thickening epidermis during lesion formation; and/or (2) the reduction of membrane lipid synthesis induced by UV damage [34]. Because subcutaneous fat exists in a substantial amount and has large Raman scattering cross section [118] we believe (1) is the major reason. The thickening of epidermis originates from the progression of malignancy [119].

While both melanoma and nonmelanoma skin cancers were included in this study, the direct comparison between BCC or SCC and MM is much less clinically relevant [120]. Thus, we compared nonmelanoma (BCC, SCC, AK) versus normal skin and MM versus PL separately. We observed that the amount of collagen was substantially lower in nonmelanoma skin cancer lesions as compared to normal skin. This could be explained by the breakdown of collagen in dermis due to the role metalloproteinases (MMP) play in degrading collagen and prohibiting procollagen biosynthesis [35]. The thickening of the epidermis also leads to reduced collagen signal collected by the probe. Furthermore, we observed the amount of elastin was higher in BCC lesions as compared to normal skin, potentially resulting from the existence of solar elastosis. Elastosis is characterized by the accumulation of disorganized elastic fibers in the dermis and commonly found in photoaging skin [36]. Finally, we found keratin was substantially higher in SCC compared to the other groups, which suggests massive keratinization disorders during SCC tumor progression [37].

By visual inspection, the mean spectra of MM and PL appear very different than the mean spectra of other pathologies. The spectral flattening between 1500 and 1700 cm^{-1} is caused by increased melanin and pigmentation, indicating Raman is sensitive to pigment-related variations. However, discriminating MM from PL remains the most challenging discrimination in skin cancer screening, resulting in high negative biopsy ratios clinically. In our study, we observed melanin content in MM is substantially higher as compared to PL, indicating massive melanocyte proliferation. The significantly lower level of triolein in MM than PL could be explained by both the reasons given above and by the strong absorption of melanin, which further reduced the signal sampled from subcutaneous

fat. In addition, collagen is substantially lower in MM than PL. This suggests that tumor formation is closely related to the changes in its stroma microenvironment in favor of its proliferation and eventual metastasis [37, 38]. Our model demonstrated that collagen, triolein, and melanin are the most important cancer identifiers for MM. Future work will explore the diagnostic potential of these biophysical parameters in discriminating skin cancers.

We observed a higher fitting residual in MM than the other tissue types. The basic assumption of our linear fitting model is that the scattering properties of tissue do not significantly distort the Raman spectrum [107], but this assumption may not hold for melanin due to its strong absorption and scattering. Intrinsic Raman spectroscopy may help correct this distortion by relating the observed and intrinsic Raman spectra through diffuse reflectance using light transport model [121]. We will also explore nonlinear fitting models to improve the fitting, such as partial least-squares (PLS) and support vector machine (SVM). Other factors also contribute to the residuals in general. One factor is that the basis spectra and bulk tissue spectra were acquired from two independent Raman systems, which were composed of different detectors, lenses, beam splitters, etc. Spectral response calibration was used to match the spectral response of the two systems, but it could not completely eliminate the differences in the spectra measured by the two systems. Another factor is the signal generated by probe components, such as the fiber background, epoxy and sapphire [106].

In general, we did not find site-specific constituents that are not covered by the current model, but the concentration of the 8 components may vary due to location. For example, when the measurement was taken on the scalp surround with dark hairs we would detect melanin signal. Future work will examine how sensitive our model is in picking up such information.

2.5 CONCLUSION

In this chapter, we proposed the first Raman biophysical model that used *in situ* Raman active components as the building blocks, and applied to *in vivo* skin cancer screening data. Our results indicate that eight basis spectra derived from collagen, elastin, triolein, cell nucleus, keratin, ceramide, melanin, and water are the most relevant to describe the spectral features of human skin Raman data. In the next chapter we will evaluate the performance of this model in discriminating skin cancer pathologies within the context of ongoing clinical studies of Raman spectroscopy for skin cancer screening in our group. We envision our model being used with the Raman probe for analyzing individual lesions pointed out by patents or providers. We think it would be reasonable to scan the top ten concerning lesions on any patients without affecting the current patient flow in a physician's office.

Chapter 3: Biophysical basis of *in vivo* skin cancer screening using Raman spectroscopy[2]

3.1 INTRODUCTION

This chapter aims to explore the diagnostic markers that Raman spectroscopy relies on for accurate *in vivo* melanoma detection.

Previous studies have shown that Raman spectroscopy is highly sensitive in differentiating malignant melanoma (MM, the deadliest version of skin cancer) from benign pigmented lesion (PL, frequently confused in the clinic with MM) [4, 67, 122]. Our group has demonstrated that MM (12 lesions) can be discriminated from PL (17 lesions) with 100% sensitivity and specificity by using a novel Raman probe-based system [94] and principal component analysis (PCA) with a logistic regression classifier [67]. Schleusener *et al*. discriminated MM (23 lesions) and PL (33 lesions) with a balanced accuracy of 91% using partial least squares discriminant analysis (PLS-DA) [123]. Lui *et al*. discriminated MM (44 lesions) from PL (286 lesions) with 90 - 99% sensitivity and 15% - 68% specificity [4] using principal component analysis with generalized discriminant analysis (PCA-GDA). A follow up independent validation study from the same group showed consistent results for discriminating MM (53 lesions) from PL (336 lesions) [124]. Their research later led to the commercial launch of a clinical skin cancer detection device (Verisante Aura) in Canada [4].

Raman spectroscopy also has been used to detect nonmelanoma skin cancer (NMSC), mainly basal cell carcinoma (BCC), squamous cell carcinoma (SCC) and actinic keratosis (AK, a precancerous state). Lieber *et al*. developed a portable confocal Raman system with a handheld probe, and achieved 100% sensitivity and 91% specificity in discriminating BCC, SCC and inflamed scar tissues from normal tissues (21 versus 21).

[2]Portions of this chapter are adapted from X. Feng, A. J. Moy, H. T. Nguyen, Y. Zhang, J. Zhang, M. C. Fox, K. R. Sebastian, J. S. Reichenberg, M. K. Markey, and J. W. Tunnell, "Raman biophysical markers in skin cancer diagnosis," J Biomed Opt 23, 057002 (2018).

The spectral differences were extracted through the maximum representation and discrimination feature (MRDF) statistical method [120]. Silveira *et al*. discriminated BCC, SCC, and AK from non-tumorous tissue (44 versus 55) with approximately 91.9% accuracy by using a dispersive Raman system and PLS-DA [125]. Schleusener *et al*. discriminated BCC from normal skin (35 versus 104) and SCC from normal skin (22 versus 104) based on PLS-DA with a balanced accuracy of 73% and 85%, respectively [123]. Lui *et al*. distinguished skin cancer and AK from benign lesions with 90 - 99% sensitivity and 24% - 66% specificity based on PLS [4]. Despite these successes, these studies have employed statistical classifiers, sometimes called "black box" methods, to describe the spectral differences between pathologies. The challenge with these statistical algorithms lies in interpreting the biophysical basis for their discriminant ability. That is, they do not provide insights into the most relevant cancer biomarkers that Raman spectroscopy relies on to make an accurate diagnosis. Therefore, we aim to determine the biophysical basis of skin cancer detection based on Raman spectroscopy. This may enable the pathologist to interpret the spectral data in a familiar manner (such as a thickening epidermis, the change of collagen and lipid content, etc.) and guide a dermatologist in determining the most appropriate treatment.

In **Chapter 2**, we proposed a Raman biophysical inverse model to derive the skin's biochemical makeup from its Raman spectrum [126]. The model described the Raman spectra from *in vivo* human skin as a linear combination of eight Raman active skin constituents extracted from skin *in situ*, including collagen, elastin, keratin, triolein, ceramide, nucleus, melanin, and water. We have validated the model using previous *in vivo* human skin cancer screening data [126] and identified distinct biophysical changes between pathologies. However, we have not evaluated the diagnostic potential of those biophysical parameters in discriminating skin cancers. We also have not identified the important biophysical features used as diagnostic tools.

In this chapter, we present a preliminary study of *in vivo* diagnosis of melanoma and NMSC on the biophysical basis. We demonstrated that the biophysical model captures

the diagnostic power of the previously used statistical classification model while also providing the skin's biophysical composition. Our work demonstrates the ability of Raman spectroscopy in sensing the biochemical composition of skin cancers, thus allowing for better interpretation of the diagnostic results from a pathological basis.

3.2 MATERIALS AND METHODS

3.2.1 Clinical Instrument and Dataset

The clinical skin cancer screening study [67] was conducted using a Raman optical fiber probe [106] integrated in an optical fiber probe-based system [94]. An 830nm wavelength excitation was used to minimize tissue autofluorescence. Collected signals entered a spectrograph and were imaged onto a camera. Integration time for each measurement was 3s. Spectral resolution of the probe-based system is around 10 cm^{-1}. This study was approved by the Institutional Review Board at The University of Texas at Austin and The University of Texas MD Anderson Cancer Center (trial registration ID: NCT 00476905). Informed consents were acquired from all patients prior to the study.

In vivo Raman spectra were obtained from 65 patients diagnosed with basal cell carcinoma (BCC), squamous cell carcinoma (SCC), actinic keratosis (AK), dysplastic nevi (DN, a dysplastic form of PL), and malignant melanoma (MM). Details of the clinical data are provided in **Table 3.1**. In total there are 100 lesions and 99 adjacent normal tissues because one normal tissue was shared between two lesions. Fourteen out of 38 SCC lesions containing both SCC and AK were grouped into SCC. Multiple spectra were taken from each lesion by moving the probe to different locations to sample as much of the lesion as possible. Multiple spectra were also taken from the normal skin adjacent to each individual lesion. Although not verified by histopathology, normal skin was visually verified to be normal by an experienced dermatologist or physician assistant.

Table 3.1: Summary of clinical data.

Lesion type	# patients	# lesions (# spectra)	# adjacent normal tissues (# spectra)
MM	10	12 (33)	11 (23)
DN	11	17 (37)	17 (33)
BCC	14	19 (39)	19 (38)
SCC	20	38 (81)	38 (76)
AK	10	14 (30)	14 (28)
Total	65	100 (220)	99 (198)

Table 3.2: Patient age for MM and DN.

MM patient #	Age	DN patient #	Age
1	70	1	75
2	58	2	69
3	81	3	31
4	-	4	34
5	69	5	29
6	33	6	69
7	68	7	34
8	70	8	28
9	60	9	35
10	78	10	22
		11	34
Average age	**65**		**42**

3.2.2 Data Preprocessing

Spectra underwent wavenumber calibration, dark noise removal, cosmic ray removal, and smoothing, followed by a fifth-order polynomial fitting [103] to remove tissue fluorescence background. Spectral data were spectral response calibrated using a tungsten halogen lamp (LS-1-CAL, Ocean Optics). Spectral band between 800 and 900

cm^{-1} was excluded due to a strong broad fiber background peak around 800cm^{-1}. A sharp room light peak at 1100 cm^{-1} was removed from five spectra from one MM patient.

3.2.3 Diagnostic Algorithms

3.2.3.1 Classification Tasks

We used four classification tasks in this study: (1) MM versus DN; (2) MM, DN versus normal (Norm); (3) NMSC (BCC, SCC, AK) versus Norm; and (4) SCC, BCC versus AK. Diagnostic algorithms were implemented within MATLAB (version R2015a, MathWorks).

We chose these four classification tasks not only to be consistent with our previous study, but also based on their clinical significance. Task (1) is significant because it directly affects the decision of a clinician to remove the lesion or continue to observe when facing a pigmented lesion of concern. Task (4) is significant because while a BCC or SCC will require surgical excision, it is often sufficient to treat an AK with cryotherapy or a topical chemotherapeutic agent. Both task (1) and (4) are highly related to reducing the number of unnecessary excisional skin biopsies. Although Task (2) and (3) are not currently clinically actionable, they are very relevant to the perspective of tumor margin detection. We used normal skin as a placeholder for these other diagnoses, with the hope that in the future we can perform the analysis on enough benign lesions to allow the device to distinguish these benign issues from cancer.

3.2.3.2 Receiver Operating Characteristic (ROC)

An ROC curve was used to determine a model's performance in discriminating between two groups. An ROC curve is a graphical representation of the trade-off between sensitivity and specificity. Sensitivity is the ability of the model to correctly identify the positive group, whereas specificity is the ability of the model to correctly identify the negative group. For good discrimination, the ROC curve is predominately in the left and

top boundaries of the graph, while for poor discrimination, the ROC curve approaches the diagonal line drawn from the bottom-left to the top-right of the plot. ROC curves were calculated separately for PCA and biophysical model, and for each of the four classification tasks.

By default, the ROC curves were calculated by treating each lesion as an experimental unit. The method is described elsewhere [29]: if one or more spectra from a site were classified as cancer, the site was classified as cancer. If all spectra from a site were classified as normal, the site was classified as normal. We used this conservative technique to approximate the dermatologist's tendency to err on the side of caution.

3.2.3.3 Statistical Model

The statistical model (PCA) was adopted from our previous publication [67]. For each classification task, we limited the number of principal components (PCs) to 5, because the diagnostic improvements dropped significantly beyond 4 [67]. Firstly, we performed PCA for a given classification task and then generated all the possible combinations of 1, 2, 3, 4, or 5 PCs from the first 15 PCs. Next, we selected one combination of PCs and built a logistic regression classifier. Specifically, for each PC-logistic regression analysis, a successive single lesion was left out for testing, with the remaining lesions being used for training. After the posterior probabilities of all lesions were calculated according to the leave-one-lesion-out cross validation protocol, an ROC curve was then calculated. Using this method, we generated different ROC curves for different combinations of PCs. The combination of PCs that yielded the largest area under the ROC curve (AUC) was selected for subsequent analyses.

3.2.3.4 Biophysical Model

In vivo Raman spectra were fit into the biophysical model with eight primary model components: collagen, elastin, triolein, nucleus, keratin, ceramide, melanin, and water, as

shown in **Figure 3.1**. Those components were collected from human skin *in situ* and were averaged over multiple patients.

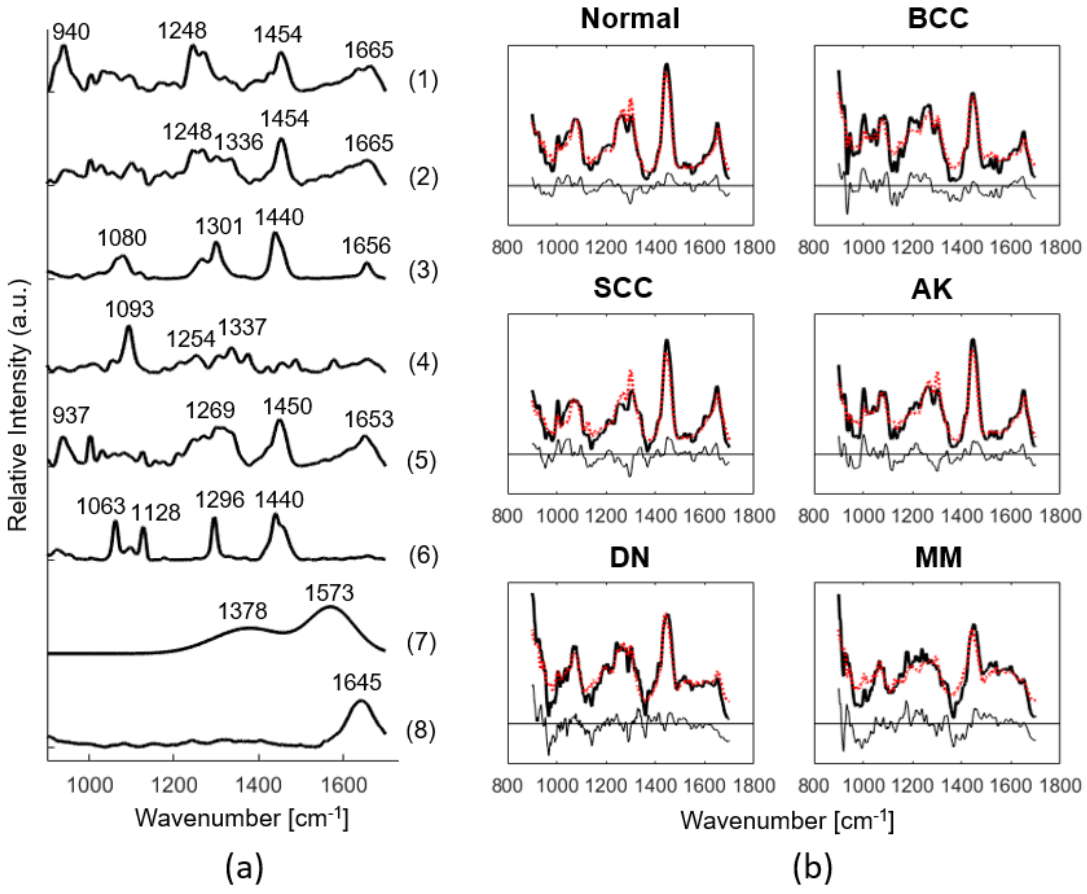

Figure 3.1: **(a**) Eight model components: (1) collagen, (2) elastin, (3) triolein, (4) nucleus, (5) keratin, (6) ceramide, (7) melanin, (8) water. Peak positions of the main Raman bands are labeled. (b) Fitting results for the average Raman spectra of normal tissue, BCC, SCC, AK, DN, and MM. Black solid lines: average Raman tissue spectra. Red dotted lines: model fits. Residuals are also plotted on the bottom. Images are adapted from Reference [126].

The model components contain both biochemical and structural information. For instance, nucleus refers to the nuclear material in the cell. Collagen and elastin refer to dermal extracellular matrix. Keratin represents epidermal extracellular matrix. Triolein mainly represents subcutaneous fat. Peak positions of the main Raman bands and their physical origin are summarized in **Table 2.2** [126-129]. The sub-bands (or sub-peaks) were not listed but also played a role in the fitting. The fit coefficients provide the relative concentration of those components and were used as the input variables of the discriminant analysis. Similar to PCA model, for each classification task, we generated all the possible combinations of 1, 2, 3, 4, or 5 components from the 8 primary model components and built logistic regression classifiers. We then selected the combination of model components that yielded the largest AUC.

3.2.4 Comparison of Discriminative Capability between Statistical and Biophysical Models

Statistical analysis was performed using an open-source package written in R software (version 3.3.3) [130]. The AUC of two paired ROC curves were compared using the bootstrap test, with a goal to determine if the biophysical model provides at least equivalent potential for classification compared to statistical model.

3.2.5 Interpretation of Biophysical Model Result

The fit coefficients of the 8 model components generated by the biophysical model were visualized using scatter plots. Each scatter point represents one spectrum. The error bar generated by the 95% CI are used to represent the variance of the fit coefficient. Unpaired Student's *t*-test was employed, and the corresponding *p* values were labeled to compare if the fit coefficients have any statistically significant difference between pathologies.

3.3 RESULTS

3.3.1 Statistical Model versus Biophysical Model

In **Table 3.3**, the diagnostically relevant model components in statistical and biophysical models are displayed and the AUCs are compared. **Figure 3.2** compares the corresponding ROC curves. The AUCs of the ROC curves of the two models are not statistically distinguishable for the classification tasks of MM versus DN, [MM, DN] versus Norm, and [BCC, SCC] versus AK. However, the AUC of the ROC of the biophysical model for [BCC, SCC, AK] versus Norm is statistically significantly better than the corresponding statistical model ($p < 0.0001$). **Table 3.4** compares the specificities of the two models corresponding to sensitivities of 90% and 95%, respectively.

Table 3.3: Comparison of diagnostic performance of statistical model and biophysical model.

Classification tasks	**# lesion**	**Diagnostically relevant components**		**ROC AUC**	
		Statistical model	Biophysical model	Statistical model	Biophysical model
MM vs DN	12 vs 17	PC 3,4,5,8,9	collagen, triolein, melanin	1.00	0.99
[MM, DN] vs Norm	29 vs 28	PC 1,6,9	triolein, melanin	0.89	0.93
[BCC, SCC, AK] vs Norm	72 vs 64	PC 3,4,8,9	collagen, triolein, elastin, nucleus, ceramide	0.58	0.76
[SCC, BCC] vs AK	68 vs 55	PC 3,6,7,8	collagen, keratin, water	0.62	0.65

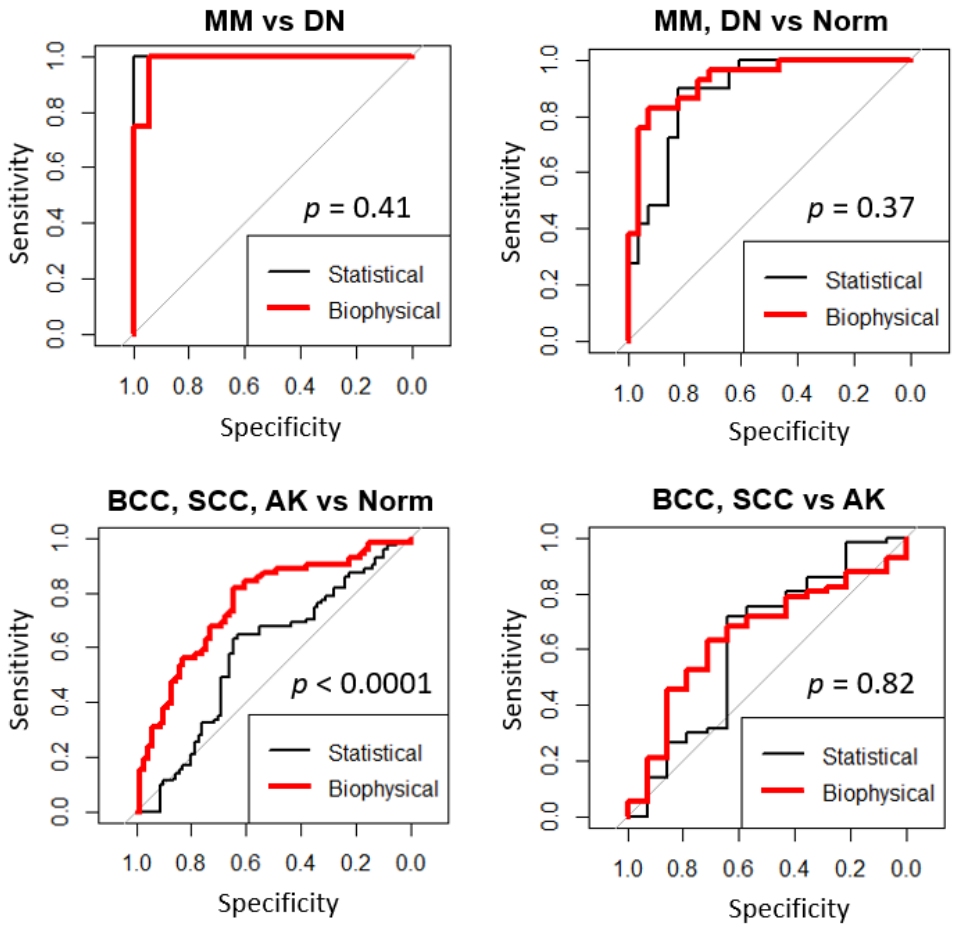

Figure 3.2: Comparison of ROC curves between statistical model (thin line) and biophysical model (thick line) for the 4 classification tasks: MM vs DN, MM, DN vs Norm (adjacent normal tissue), BCC, SCC, AK vs Norm, and BCC, SCC vs AK. The ROC curves are statistically compared, and the *p* values are labeled. $p > 0.05$ indicates no significant difference between the two curves.

Table 3.4: Comparison of specificities derived from ROCs according to sensitivities of 95% and 90%.

Classification tasks	Statistical model		Biophysical model	
	Sensitivity (%)	Specificity (%)	Sensitivity (%)	Specificity (%)
MM vs. DN	95	100	95	94
	90	100	90	94
[MM, DN] vs. Norm	95	64	95	71
	90	71	90	75
[BCC, SCC, AK] vs. Norm	95	10	95	18
	90	6	90	39
[SCC, BCC] vs. AK	95	21	95	11
	90	21	90	21

3.3.2 Biophysical Basis of Classification Results

3.3.2.1 Malignant Melanoma (MM) versus Dysplastic Nevi (DN)

The biophysical model reveals the biomarkers responsible for the variances between pathologies. Major bands used for fitting and their physical origin was shown in **Table 3.3** and reported in literature [126-129]. The fit coefficients of the eight model components in DN and MM are displayed in **Figure 3.3**. Statistical analysis indicates significant differences in collagen, elastin, triolein, nucleus, and melanin content between MM and DN. Collagen and triolein contributed greatly to the spectral variance between MM and DN. By using the fit coefficients of collagen and triolein, 29 out of 33 MM spectra and 35 out of 37 DN spectra are correctly classified (**Figure 3.4**).

The best result was achieved by employing 3 components: collagen, triolein and melanin, resulting in 12 out of 12 MM lesions and 16 out of 17 DN lesions being correctly classified. ROC AUC is 0.99, and specificity is 94% (90% – 95% sensitivity, **Table 3.4**).

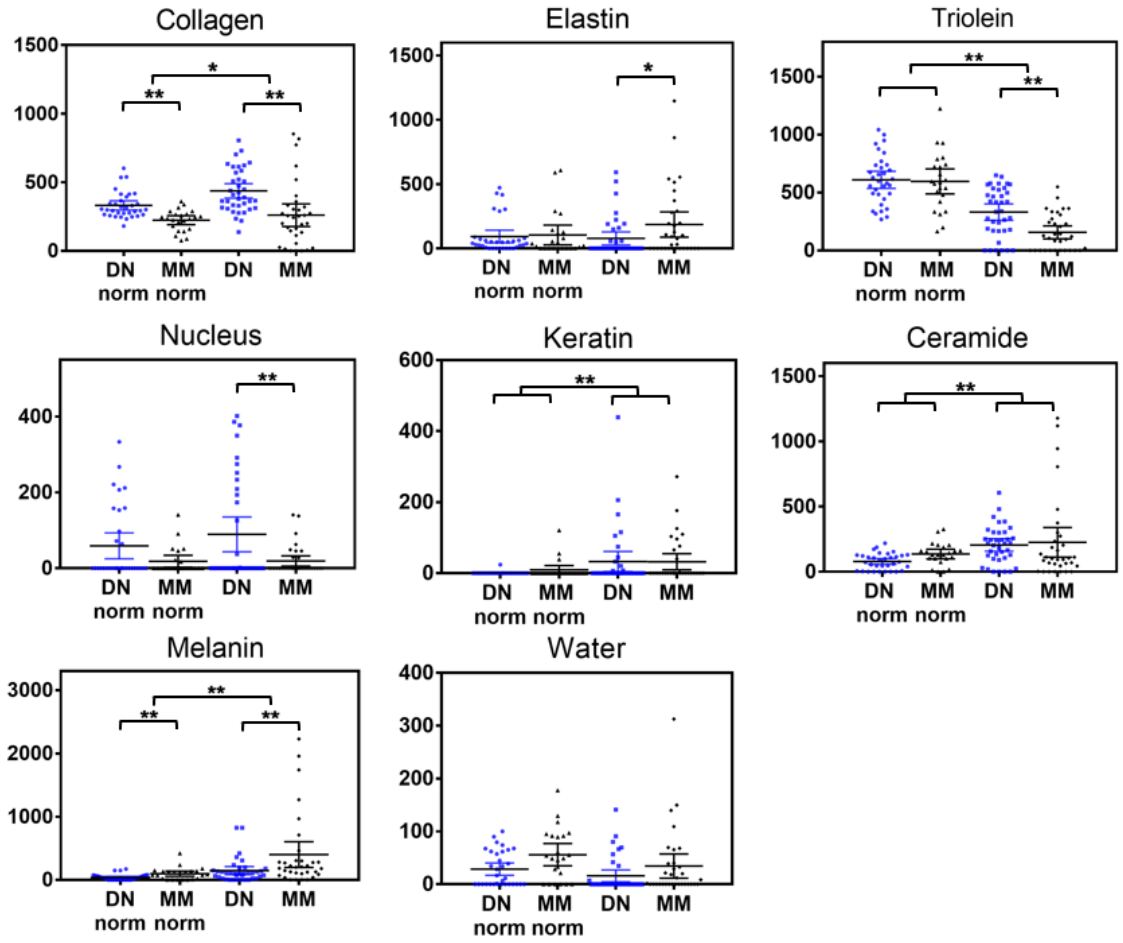

Figure 3.3: Fit coefficients of the 8 model components computed from the biophysical model. Each point represents a spectrum data. Significance tests are conducted for the fit coefficients of DN norm (the adjacent normal tissue of DN) versus MM norm (the adjacent normal tissue of MM), DN versus MM, and [DN norm and MM norm] versus [DN and MM]. ** $p \leq 0.01$, * $p \leq 0.05$.

3.3.2.2 Pigmented Lesions (MM, DN) versus Adjacent Normal Tissue

Figure 3.3 shows that pigmented lesions and their adjacent normal tissue have significant differences in triolein, collagen, ceramide, keratin, and melanin content. Our

results show that triolein and melanin are the most relevant model components to discriminate MM and DN from adjacent normal skin. The ROC AUC is 0.93 (**Table 3.3**) for sensitivities from 95% to 90% and specificities of 71% to 75% (**Table 3.4**).

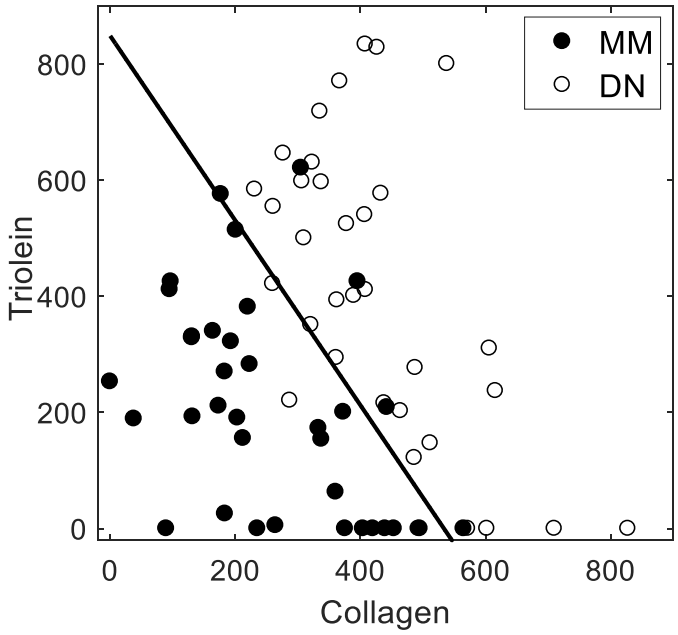

Figure 3.4: Scatter plot drawn from triolein and collagen content. The solid logistic regression line separates MM from DN.

3.3.2.4 Nonmelanoma Skin Cancers (BCC, SCC) versus AK

Figure 3.5 shows significant differences in collagen, nucleus, keratin and water between SCC and AK, as well as significant differences in keratin and ceramide between BCC and AK. The fit coefficients of collagen, keratin and water discriminated BCC, SCC from AK with a ROC AUC of 0.65 (**Table 3.3**), and specificities range from 11% to 21% for sensitivities corresponding to 95% to 90% (**Table 3.4**).

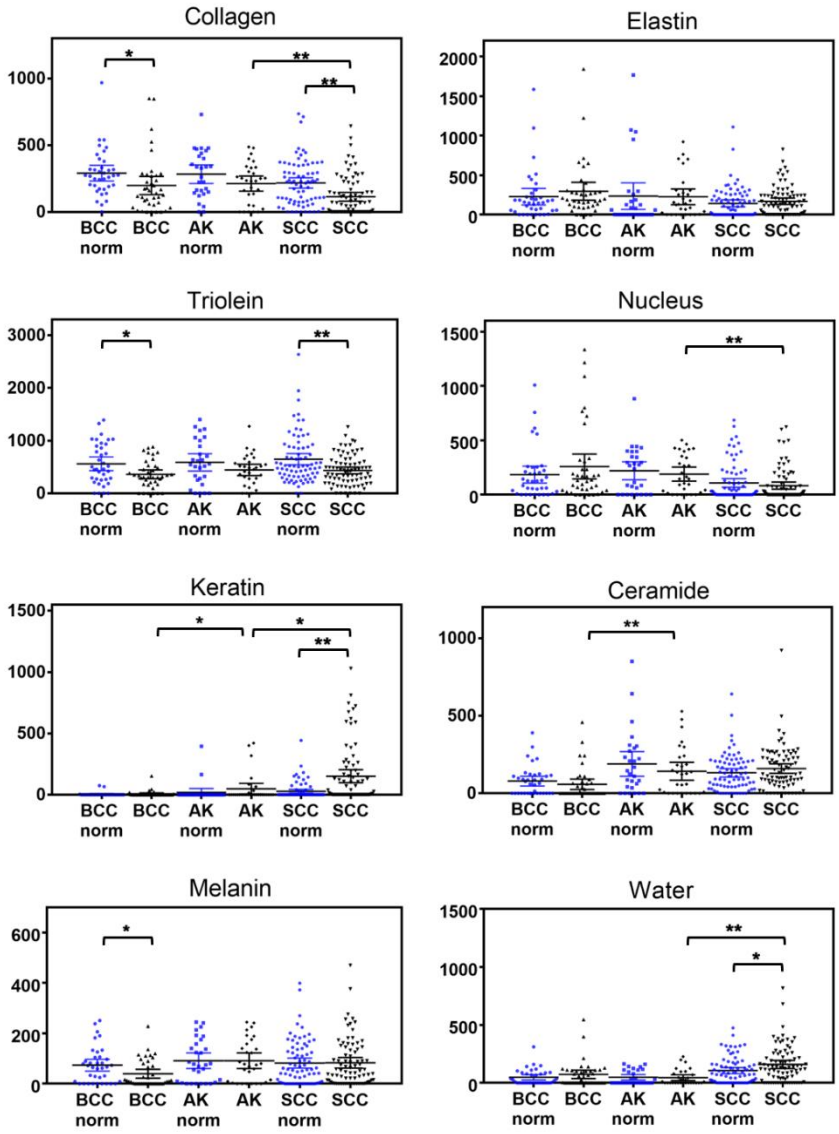

Figure 3.5: Fit coefficients of the 8 model components computed from the biophysical model. Each point represents a spectrum data. Significance tests are conducted for the fit coefficients of adjacent normal tissue of BCC (BCC norm) versus BCC, the adjacent normal tissue of SCC (SCC norm) versus SCC, SCC vs AK, and BCC vs AK. ** $p \leq 0.01$, * $p \leq 0.05$.

3.4 DISCUSSION

In our previous work [67], we demonstrated the capability of Raman spectroscopy in detecting skin cancers using a statistical model. Here we show that a biophysical model can achieve consistent diagnostic performance with the statistical model while simultaneously extracting the relevant biomarkers accounting for the diagnosis.

Our model reveals a markedly different biochemical and structural composition between pathologies. First, the amount of triolein is significantly lower in all skin lesions than surrounding normal skin. Triolein mostly originates from adipose tissue in the subcutaneous layer, with a small contribution from epidermal surface lipids [113]. Triolein has a large Raman scattering cross-section, thus contributing greatly to normal skin spectra. The decrease of triolein in skin lesions does not necessarily indicate the actual amount of fat decreases in skin lesions, only that there is a decrease in the triolein sampled by the probe. One possible reason is epithelial thickening associated with dysplastic progression [131, 132]. An increased thickness of epidermis would mean the total volume of tissue sampled would include more epidermis and less adipose tissue, thereby decreasing the amount of Raman emission from deeper skin layers (adipose). Another possible reason for the decrease of triolein in pigmented lesions relative to the adjacent normal skin is that melanin strongly absorbs excitation laser power and therefore reduces the contribution of triolein in Raman signal.

Next, we found that the collagen content is significantly lower in nonmelanoma skin cancers than their adjacent normal tissue and AK. For instance, collagen does not change significantly in the progression from normal to AK (benign), but it decreases significantly from AK to SCC (cancer). This trend of decreased collagen in cancer was also observed in previous biophysical models of *ex vivo* human skin fragments [65], urological tissue [96], gastric/esophagus tissue [97], and cervical tissue [133]. This may be partially explained by the thickening of the epithelium as mentioned above. Other reasons may include the release of metalloproteinases (MMP) by cancerous cells to degrade dermal

connective tissue [134, 135], and extracellular-degrading enzymes secreted from fibroblasts that damage the stroma [136].

Discriminating MM from benign pigmented lesions (especially DN) usually leads to large negative biopsy ratio. Due to their highly similar appearance, the ratio of negative versus positive biopsies ranges from 22:1 to 59:1 for experienced versus new general practitioners [5]. Understanding the biophysical basis of melanoma skin cancer progression is essential to reduce large negative biopsy ratio and save considerable associated costs and efforts. In our study, we discovered that collagen and triolein are the two most important biomarkers to differentiate MM from DN, and NMSCs from normal tissue. Two previous *ex vivo* studies based on Raman biophysical models also showed collagen and triolein (or fat) had important roles in tissue Raman spectra. Bodanese *et al.* discovered the amount of collagen and fat extracted from tissue Raman spectra can classify BCC from normal skin with sensitivity and specificity of 95% and 83% [64]. Haka *et al*. found the fit coefficients of collagen and fat can distinguish cancerous breast tissues from normal and benign tissues with 94% sensitivity and 96% specificity [118].

Our results show that melanin is an important biomarker for classifying pigmented lesions from adjacent normal tissue, which is as expected because pigmented lesions typically contain more melanin than the surrounding normal skin. However, we also found melanin is not as relevant as collagen and triolein in differentiating MM from DN. In fact, melanomas do not always have more melanin than do benign pigmented lesions. The existence of amelanotic melanoma is a good example – we estimated zero melanin content for the one amelanotic melanoma lesion in our sample. Blue nevi, on the other hand, contain abundant pigment but are not cancer. Thus, more data from amelanotic melanomas is needed to clarify the role that melanin may play in differentiating MM and DN.

We were best able to classify NMSCs from normal skin by employing a model that considered collagen, triolein, elastin, nucleus, and ceramide. To better understand the biophysical changes of each pathology, we examined the lesion-normal pairs for BCC and SCC separately. We found that melanin content is significantly lower in BCC than in

adjacent normal skin, likely because the invasion of basal cells takes over the space normally occupied by the melanocytes. Although not statistically significant, the amount of nucleus and elastin is larger in BCC compared to its adjacent normal skin, which may be explained by the proliferation of cancer cells and the enlargement of nuclei. Elastin content is also larger in BCC than adjacent normal, probably because of the existence of solar elastosis [137]. On the contrary, SCC appears to have a higher amount of keratin, ceramide, and water as compared to its adjacent normal skin. The increase of keratin may be attributed to large areas of keratinization in response to malignant epithelial cells [138]. Ceramide indicates abnormal epidermal surface lipid synthesis and thus is a key component to differentiate SCC from normal skin.

AK is the most common precursor lesion of SCC among lightly pigmented individuals. Almost every SCC that arises on sun-damaged skin has evidence of AK in the epidermis, either directly contiguous with or adjacent to the neoplasm [139]. However, AK and SCC have a similar crusted appearance, making it difficult to differentiate by visual examination. We found the most important components to discriminate SCC from AK are collagen, keratin and water. AK is confined to foci within the epidermis, whereas SCC may further invade into dermis. Thus, SCC is expected to have a higher amount of keratin than AK. Nucleus content is lower in SCC than AK, likely because the prominent keratinization in SCC occupies the space of cells. We also observed a higher amount of water content in SCC than AK. High wavenumber Raman will be an ideal tool to study the significance of water in NMSC diagnosis.

An interesting discovery is that the normal tissue adjacent to a DN has significantly more collagen than normal tissue adjacent to a MM (**Figure 3.2**). We were suspicious that the observed difference in collagen could be simply due to aging since the average age of the MM patients (N = 9) in our study was 65 years (one patients did not have age information on record), while the average age of the DN patients (N = 11) was 42 years (**Table 3.2**). To control for the effect of aging, we built a generalized linear mixed-effect model [140] using patient age and collagen as fixed effects predictors, and tissue type as

the response variable (0 = normal tissue adjacent to DN, 1 = normal tissue adjacent to MM). We also included a random-effects term for intercept grouped by patient to account for patient-specific variations. Our result shows that the *p* value of collagen is 0.041, indicating the amount of collagen is a significant predictor of tissue type, even after controlling for age. It is plausible that there is more collagen in normal skin adjacent to DN than in that adjacent to MM because melanoma growth is not only associated with malignant growth of cancer cells, but also changes in its stroma microenvironment to support metastasis [141]. Paidi *et al.* discovered that the use of Raman spectroscopy is feasible to detect changes in the stroma of the lung microenvironment in response to primary breast tumors [142]. Sahu *et al.* found that early malignancy-associated changes in normal contralateral sites of oral cancer may lead to anatomical variability and cause misclassification between contralateral and tumor [143]. Boppart *et al.* raised the question that molecular surgical margin may be a better way to define tumor boundary than the "gold standard" structural tumor margin [144]. Further studies are needed to study changes in normal stroma in response to dysplastic progression.

One limitation of this study is that it simplifies the model to only eight Raman active components. Although originally we had 15 components, we narrowed down to 8 to avoid collinearity issues [126]. We found including multiple chemically similar components (e.g. various proteins) would result in fitting results with high variance. However, as there are far more molecules in skin, this method may underestimate the contribution of other molecules to the Raman signal. Another limitation is the limited sample size, which is also the main reason that we used leave-one-out cross validation to compute the ROC AUC. It is worth mentioning that this method comes with the risk of over-optimism. This may be the cause for the discrimination of MM from DN being better than that of (MM, DN) from normal (**Figure 3.2**). Alternative methods include (1) k-fold cross validation (such as k = 10), and (2) bootstrapping [145]. The former utilizes 10% of the data as a test set, and the other 90% as the training set. Although it avoids the caveat of using single observation to

estimate the model performance in each split of the data, it requires a larger sample size. The latter approach may provide a better estimate of internal validity [146].

3.5 CONCLUSION

In this chapter, we have demonstrated that the biophysical model has consistent diagnostic capability as our previously published statistical model. By comparing with the statistical model, we have demonstrated that the biophysical model captures the spectral variances between skin pathologies in four distinct classification tasks. More importantly, the biophysical model captures the relevant biophysical changes accounting for the diagnosis. In particular, we found that collagen and triolein were the most important biomarkers in discriminating malignant melanoma from benign pigmented lesions, and nonmelanoma skin cancers and precancers from surround normal skin. Our work demonstrated that Raman spectroscopy has great potential in diagnosing skin cancer noninvasively while extracting the skin's biophysical composition.

Chapter 4: Biophysical basis of *ex vivo* skin cancer surgical margin detection using Raman spectroscopy[3]

4.1 INTRODUCTION

Achieving adequate margins during tumor margin resection is critical to minimize the recurrence rate and maximize positive patient outcomes during skin cancer surgery. Previous studies have demonstrated Raman spectroscopy can accurately detect basal cell carcinoma (BCC) from surrounding normal tissue; however, the biophysical basis of the detection remained unclear. Therefore, the goal of this chapter is to explore the relevant Raman biomarkers to guide basal cell carcinoma margin resection.

Nonmelanoma skin cancer is by far the most common malignancy worldwide. Among more than 5 million new cases diagnosed annually in the US, approximately 80% are BCC [147]. Currently, Mohs micrographic surgery (Mohs) is the most effective method for the treatment of BCC. The 5-year recurrence rate of Mohs (1 – 3% for primary BCC and 5 – 7% for recurrent BCC) is much lower than standard surgical excision (3 – 10% in primary BCC and >17% in recurrent BCC) [11]. Mohs involves iterative excision of surgical margins of each stage, followed by frozen section histopathology. If the histopathological diagnosis indicates tumor still exists, further tissue layers will be removed until the margins are clear.

Although effective, Mohs has several limitations, including time, expense, training requirements and lab infrastructure. Most tumors require 1 to 3 stages (sometimes as many as 5 – 6) for complete removal, with patients waiting under local anesthesia between each stage [148]. The total time for Mohs surgery can be anywhere from one to five hours. Infrastructure requirements may also be limiting, including the building and maintenance of histology lab, staff training and physician training. As these requirements pose

[3]Portions of this chapter are adapted from X. Feng, M. C. Fox, J. S. Reichenberg, F. C. Lopes, K. R. Sebastian, M. K. Markey, and J. W. Tunnell, "Biophysical basis of skin cancer margin assessment using Raman spectroscopy," Biomedical Optics Express **10**, 104-118 (2019).

significant barriers to its use, Mohs is used in less than half (~40%) of cases, and less effective treatments such as standard surgical excision are more frequently employed [149]. Moreover, disparities in access to care, such as in among different geographic regions and racial and ethnic groups, leads to substantial underutilization of Mohs in underserved populations [149, 150]. Therefore, a critical unmet need exists for low-infrastructure technologies that would enable general dermatologists to perform resections with high accuracy.

Raman spectroscopy is a nondestructive and label-free optical technique, and has demonstrated great clinical merits for tumor margin assessment in numerous types of cancer, including skin [151], brain [152, 153], oral cavity [154, 155], breast [57, 156], and stomach [157]. Those studies either use fiber-optical Raman probe for single point sampling or Raman microscopy (also called Raman microspectroscopy) for optical imaging. One major advantage of Raman microscopy is that it has high resolution and sectioning comparable with that of conventional histology. Moreover, it provides an objective diagnosis with minimal tissue processing. Previous studies have demonstrated Raman microscopy can discriminate BCC from normal skin tissues with sensitivity of 90 – 100% and specificity of 85 – 93%. Nijssen *et al*. was among the first to discriminate BCC from surrounding normal tissue using Raman spectroscopy and reached 100%/93% sensitivity/specificity (15 patients, 59 spectra) [158]. Lieber *et al*. developed an *in vivo* Raman microscopy and achieved 100%/91% sensitivity/specificity (19 patients, 42 spectra) in classifying BCC and squamous cell carcinoma from paired normal skin tissues [120]. Larraona-Puy *et al*. demonstrated the ability of Raman microscopy in discriminating BCC from surrounding normal tissue with 90%/85% sensitivity/specificity (20 patients, 329 spectra) [159]. Kong *et al*. combined Raman microscopy with autofluorescence imaging to increase acquisition speed and achieved 100% sensitivity and 92.9% specificity for discriminating BCC [151].

Prior studies mostly utilized statistical algorithms to extract the spectral differences between BCC and normal tissue, such as principal component analysis [151, 158], linear

discriminant analysis [160] and maximum representation and discrimination feature [120]. Although such methods provided high diagnostic accuracy, they did not elucidate the nature and biochemical processes responsible for the spectral differences. Understanding the biophysical basis of the discriminatory power of Raman spectroscopy would increase fundamental knowledge of cancer processes as well as lay the groundwork for improving the diagnostic performance of the technology [40]. Therefore, our aim in this study is to obtain biophysically relevant markers from Raman spectra of BCC and surrounding normal tissue, and then build diagnostic model to guide BCC tumor margin delineation.

In **Chapter 2**, we proposed a biophysical human skin cancer model, an inverse model that infers the skin's biochemical makeup from its Raman spectrum [161]. Different from previous studies that selected a number of Raman bands as "fingerprints" to discriminate between healthy skin and tumor regions [159, 162], our method is based on the fitting of pure spectral components. We validated the model using previous *in vivo* human skin cancer screening data [67], and demonstrated the feasibility of Raman spectroscopy to capture relevant biophysical changes accounting for the *in vivo* diagnosis [163]. Later, we presented a preliminary study of BCC tumor margin detection using the biophysical model based on a small dataset from 14 patients [164]. This study demonstrated the feasibility of detecting biophysical changes between BCC and five primary normal structures (epidermis, dermis, hair follicle, sebaceous gland and fat), but has several limitations: firstly, the number of patients is small; secondly, inflamed dermis was not included in the study, which may be confused with BCC in histopathological diagnosis [151, 159]; finally, a more comprehensive analysis is needed to link our biophysical approach with molecular vibrational approaches [128, 129].

In this chapter, we demonstrate that Raman spectroscopy is highly sensitive in capturing the biochemical differences between BCC and surrounding normal skin structures. Based on these biochemical differences, we can develop diagnostic algorithms to accurately discriminate BCC in Mohs excisions, which supports the future development of intraoperative assessment of tumor margins.

4.2 MATERIALS AND METHODS

4.2.1 Patients and Sample Preparation

This study was approved by the Institutional Review Board (IRB) at The University of Texas at Austin and the Seton Healthcare Family. A total of 30 frozen tissue blocks were collected from 30 patients who had undergone Mohs at Austin Dermatologic Surgery Center. 18 samples were found to have both BCC tumors and surrounding normal tissue, and 12 samples contained only normal tissue. Before the Raman experiment, 20μm tissue sections were sliced from frozen tissue blocks at -22C and transferred onto low Raman background glass slides (MgF2 substrates). Serial sections were transferred onto microscope slides for hematoxylin and eosin (H&E) staining. The H&E technique stains cell nuclei in purple (hematoxylin), and intracellular or extracellular protein in red (eosin). Tissue structure identification and histopathological diagnosis were provided by a board-certified dermatologist.

4.2.2 Raman Imaging Experiment and Data Preprocessing

Raman imaging was performed using a custom-built confocal Raman microscope. We used a longer wavelength laser (830nm) to minimize tissue autofluorescence. Reflectance confocal and bright-field images are also collected simultaneously. A detailed system description can be found elsewhere [161]. The power delivered to the sample was approximately 45mW. Raman images were collected from "tissue-level" regions varying from 60×60 μm^2 to 100×100 μm^2 (2μm steps, 2s per step). The "tissue-level" regions consist of ~10 – 100 cells, approximating the resolution of a dermatologist reading an H&E slide.

Raw Raman spectra underwent wavenumber calibration, dark noise removal, cosmic ray removal, smoothing, and a fifth-order polynomial fitting [103] to remove tissue fluorescence background. Spectral response calibration was conducted using a tungsten

halogen lamp (LS-1-CAL, Ocean Optics, FL, USA). The effective spectral range was 800 to 1790 cm^{-1}. Data were normalized to the area under curve.

4.2.3 Clustering Analysis

Raman pseudo-color images were generated by k-means clustering. K-means is an unsupervised algorithm for cluster analysis and can easily handle large amounts of Raman spectroscopy data for cell [165] and tissue [158] imaging. The first 100 principal components accounting for 95% - 99% of the variation in the dataset served as input for K-means. The number of clusters was determined by visual comparison of the pseudo-color image and histopathology. Each cluster was represented by a centroid Raman spectrum and assigned a different color. To eliminate spectral outliers, any spectrum that belonged to a cluster that was more than three times the standard deviation from the mean of that cluster was omitted [158]. We then annotated the centroid Raman spectrum of each cluster as either BCC or normal skin structures: inflamed dermis (Inf), epidermis (Epi), dermis (Der), hair follicle (HF), hair shaft (HS), sebaceous gland (SG), and fat. HS is a long filament in the center of the follicle extended above the surface of epidermis (also called hair). HF is the sheath of cells and connective tissue that surrounds the root of a hair. HF and HS were separated because they had heterogenous biochemical composition [160]. While muscle tissue can be present in Mohs sections and has been studied in other Raman studies [151, 162], it generally appears in a small minority of cases; thus, we have excluded it from this study.

4.2.4 Raman Biophysical Model

A previously developed biophysical model [161] was used to extract the biochemical composition from the centroid Raman spectra of BCC and normal tissue structures. The model consists of seven Raman active components: collagen, elastin, triolein, keratin, nucleus, ceramide, and water, as shown in Fig. 1. Melanin was not included because melanin played a minor role in fitting the spectra of normal tissue and non-pigmented BCC. All the model components were extracted from human skin sections in situ and contained rich biochemical and structural information. For instance, collagen and elastin were the major constituents in dermal extracellular matrix, while keratin was rich in epidermal extracellular matrix. Nucleus represented the nuclear material in the cell. Ceramide was important constituent in epidermal lipid, while triolein existed in small amount in sebaceous lipid and large amount in subcutaneous fat.

4.2.5 Model Fitting and Statistical Analysis

Each centroid Raman spectrum was described as a linear combination of the model components according to a non-negative linear least-squares fitting criteria. The fit coefficients were then visualized using scatter plots. The variation of the fit coefficient is represented by the error bar generated by the 95% confidence interval. The fit coefficients of BCC and individual normal tissue structures were statistically compared. To account for dependencies in the data inherent from measuring multiple skin structures per patient, linear fixed-effects models were employed with the skin structures (epidermis, dermis, etc.) treated as a fixed effect and the patient treated as a random effect. The models were fitted using restricted maximum likelihood and *p*-values were derived from t-tests using Satterthwaite approximations [166, 167].

4.2.6 Diagnostic Algorithm

A logistic regression classifier was built to discriminate BCC from normal tissue structures based on their fit coefficients. Leave-one-patient-out receiver operator

characteristic (ROC) analysis was used to determine the optimum number of input model components., i.e., the models were trained using a subset of 29 patients and tested on the remaining one patient. To avoid overfitting, the number of input model components was in all cases no more than 4. Leave-one-spectrum-out ROC analysis was also performed for inspection of the misclassified spectra. The area under the ROC curve (AUC) was calculated to measure the discriminatory power of the classification model. The combination of sensitivity and specificity with of greatest clinical value was obtained from the ROC curve. Sensitivity determines the ability of the model to correctly identify the positive group, whereas specificity is the ability of the model to correctly identify the negative group. Positive predictive value (PPV) and negative predictive value (NPV) were derived from the following equation. PPV is the probability that the positive group (BCC) identified by the model is truly positive. NPV is the probability that the negative group (normal tissue) identified by the model is truly negative.

$$PPV = \frac{number\ of\ true\ positives}{number\ of\ true\ positives + number\ of\ false\ positives} \quad \textbf{(4.1)}$$

$$NPV = \frac{number\ of\ true\ negatives}{number\ of\ true\ negatives + number\ of\ false\ negatives} \quad \textbf{(4.2)}$$

4.3 RESULTS

4.3.1 Annotated Tissue Spectra Database

In total, we obtained 223 centroid Raman spectra from 30 patients, including 50 spectra from BCC, and 173 spectra from normal structures (including inflamed dermis (N = 19), epidermis (N = 26), dermis (N = 47), hair follicle (N = 31), hair shaft (N = 18), sebaceous gland (N = 22), and fat (N = 10)).

Reflectance confocal images were also collected from each region. The images could also be stitched together to generate a larger field of view. Reflectance confocal images of various skin structures are displayed in **Appendix B**.

Figure 4.1 shows a typical example of Raman experiment. Good visual correspondence was observed between Raman pseudo-color images and H&E images of the serial section. **Figure 4.2** shows the mean Raman spectra of BCC and normal structures. The main differences between BCC and epidermis/hair follicle/inflamed dermis can be found at 1093, 1577, 1663 cm^{-1} (assigned to nucleus), while the main differences between dermis and BCC can be found at 856, 940, 1248 cm^{-1} (assigned to collagen).

4.3.2 Biophysical Model Fitting Results

Figure 4.3 shows the mean Raman spectra fit to the model components in Fig. 1. The fit coefficients of the model components computed from the biophysical model were visualized in **Figure 4.4**. Statistical significance for BCC versus inflamed dermis, BCC versus epidermis, BCC versus dermis, and BCC versus hair follicle was demonstrated in **Figure 4.4**. A complete list of statistical comparison between BCC and individual normal structures was displayed in **Table 4.1**.

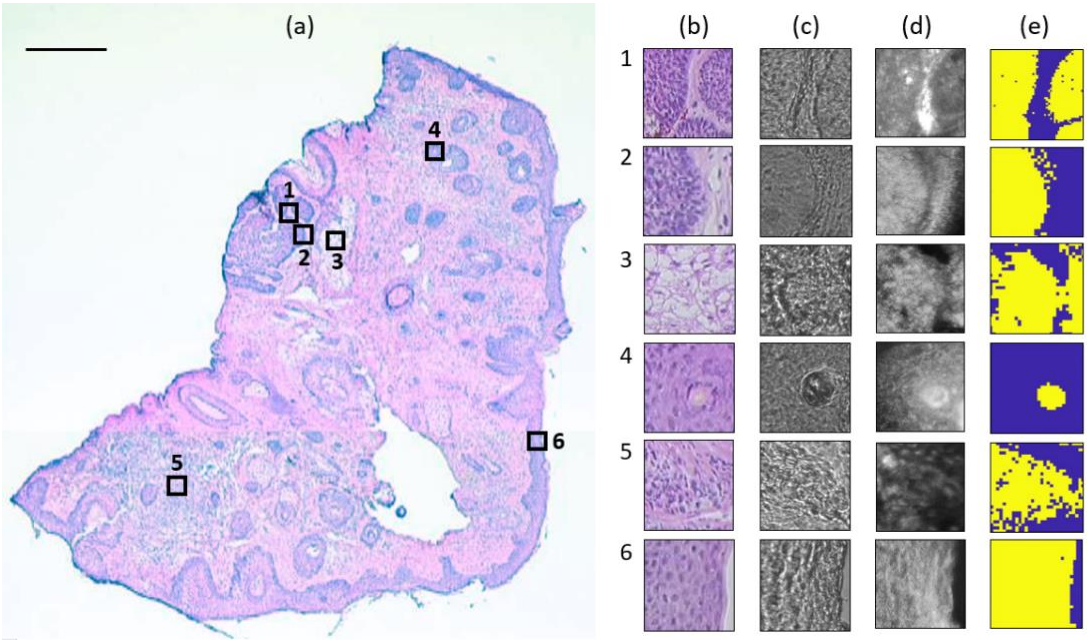

Figure 4.1: Raman experiment on a typical skin tissue section. (a) H&E image shows six measured regions of 100×100 μm^2, being represented as empty squares. Scale bar: 500 μm. (b) H&E image of the serial section. (c) Bright-field image. (d) Reflectance confocal images. (e) Raman pseudo-color image generated by k-means. Region 1 and 2 contains BCC (yellow) and dermis (blue), region 3 contains sebaceous gland (yellow) and MgF_2 substrate (blue), region 4 contains hair shaft (yellow) and hair follicle (blue), region 5 contains inflamed dermis (yellow) and dermis (blue), and region 6 contains epidermis (yellow) and MgF_2 substrate (blue).

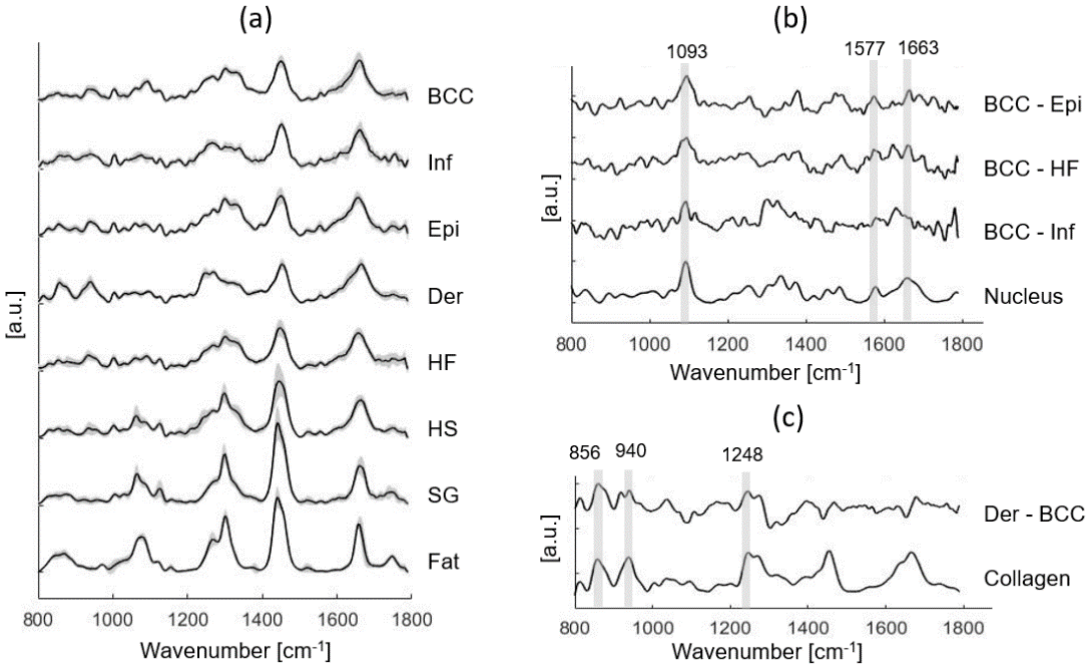

Figure 4.2: Mean Raman spectra ± SD of all individual tissue structures, including BCC, Inf (inflamed dermis), Epi (epidermis), Der (dermis), HF (hair follicle), HS (hair shaft), SG (sebaceous gland) and fat. (b) Spectral differences of mean spectra of BCC minus Epi, BCC minus HF, and BCC minus Inf are compared with the basis spectrum of nucleus. (c) Spectral difference of mean spectra of dermis minus BCC is compared with the basis spectrum of collagen. Peak positions of the main Raman bands are labeled.

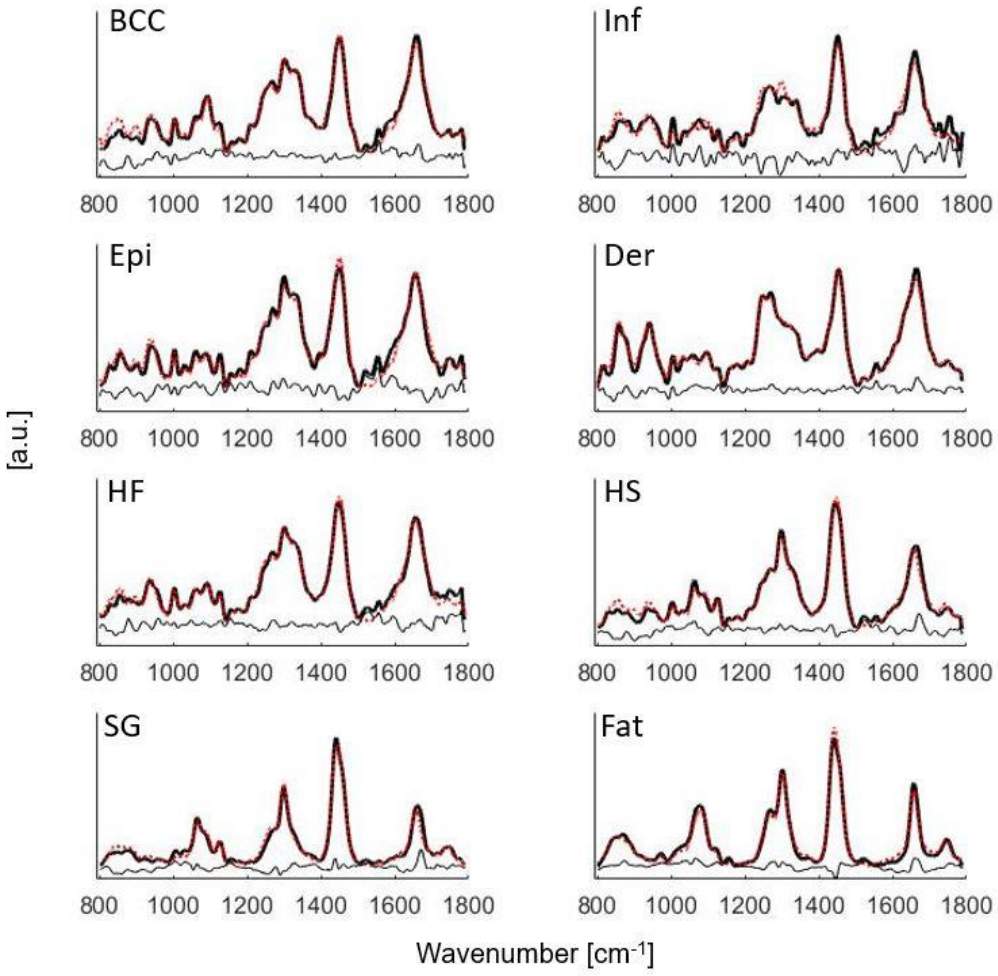

Figure 4.3: Mean Raman spectra of BCC, Inf (inflamed dermis), Epi (epidermis), Der (dermis), HF (hair follicle), HS (hair shaft), SG (sebaceous gland) and fat fit to the model components in Fig. 1. Black solid lines: mean tissue spectra. Red dotted lines: model fits. Residuals are also plotted on the bottom.

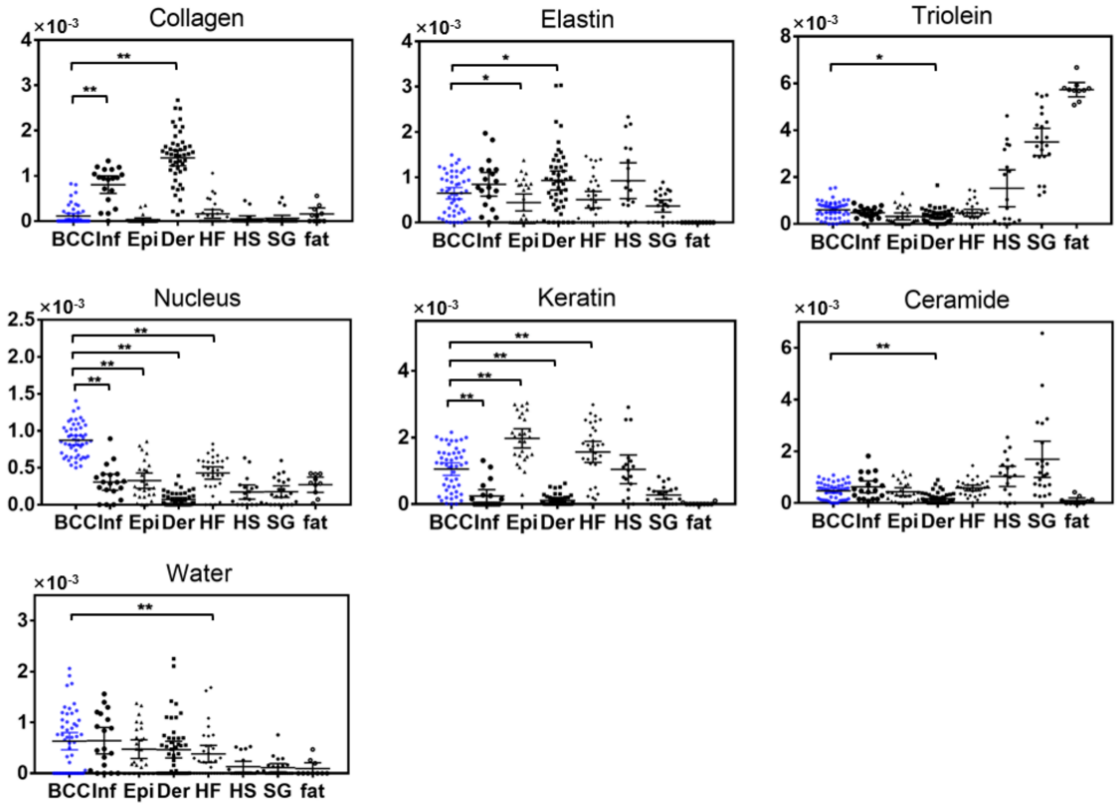

Figure 4.4: Fit coefficients of the biophysical markers for BCC (N = 50), Inf (inflamed dermis, N = 19), Epi (epidermis, N = 26), Der (dermis, N = 47), HF (hair follicle, N = 31), HS (hair shaft, N = 18), SG (sebaceous gland, N = 22) and fat (N = 10). Each point represents a spectrum data. Statistical significance of BCC versus Inf, BCC versus Epi, BCC versus Der, and BCC versus HF are labeled. ***$p \leq 0.05$, ****$p \leq 0.01$.

Table 4.1: Statistical comparison between BCC and individual normal structures (*p≤ 0.05, **p≤0.01).

		Collagen	Elastin	Triolein	Nucleus	Keratin	Ceramide	Water
BCC vs.	Inflammation	**			**	**		
	Epidermis		*		**	**		
	Dermis	**	*	*	**	**	**	
	Hair follicle				**	**		**
	Hair shaft			**	**		**	
	Sebaceous gland		**	**	**	**	**	**
	Fat		**	**	**	**		*

4.3.3 Discrimination between BCC and Normal Tissue Structures

The optimum results to classify BCC from all normal structures were reached by using the fit coefficient of nucleus alone, leading to an AUC of 0.94 for leave-one-patient-out ROC analysis, and 0.97 for leave-one-spectrum-out ROC analysis (**Figure 4.5**). Additional inclusion of keratin, triolein, and collagen in the classification model did not further improve the diagnostic performance (**Table 4.2**). A summary of misclassifications is displayed in **Table 4.3**. One may see that hair follicle and epidermis are more commonly misclassified as BCC compared to other normal structures. The discrimination threshold is chosen to prioritize either high sensitivity or high specificity, or a balanced combination of sensitivity and specificity (both ≥90%). By prioritizing high sensitivity, classification result achieved 100% sensitivity, 84% specificity, 65% PPV, and 100% NPV; while by prioritizing high specificity, classification result reached 52% sensitivity, 99% specificity, 93% PPV, and 88% NPV.

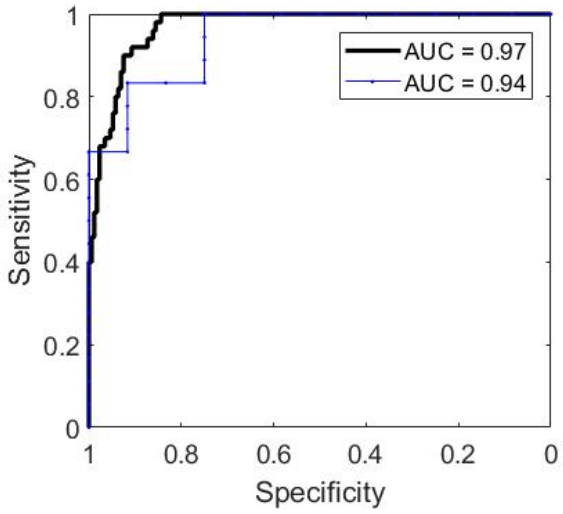

Figure 4.5: ROC analysis for classifying BCC from all normal structures. Black thick line: leave-one-spectrum-out ROC curve. Blue thin line: leave-one-patient-out ROC curve.

Table 4.2: Discriminating between BCC and all normal structures using optimum combination of components.

# components	Optimum combinations	Leave-one-patient-out ROC AUC	Leave-one-spectrum-out ROC AUC
1	[nucleus]	0.94	0.97
2	[nucleus, keratin] [nucleus, triolein] [nucleus, collagen]	0.94	0.97
3	nucleus, triolein, keratin] [nucleus, triolein, collagen]	0.94	0.97
4	[nucleus, keratin, triolein, collagen]	0.93	0.96

Table 4.3: Summary of misclassifications by prioritizing high sensitivity or specificity.

	Sensitivity/ Specificity (%)	PPV/ NPV (%)	BCC	Normal tissue structures						
				Inf	Epi	Der	HF	HS	SG	Fat
Prioritizing high sensitivity	100/84	65/100	0/50	3/19	6/26	0/47	15/31	2/18	1/22	0/10
Prioritizing high specificity	52/99	93/88	24/50	1/19	1/26	0/47	0/31	0/18	0/22	0/10
Balanced sensitivity and specificity	90/92	76/97	5/50	2/19	5/26	0/47	6/31	1/18	0/22	0/10

Figure 4.6 represents separating BCC from different categories of normal structures using the fit coefficients of two primary model components. **Figure 4.6**(a) shows that epidermis and hair follicle have the largest overlap with BCC compared to other normal structures. The overlap occurs when epidermis and hair follicle have comparable level of keratin and nucleus content as BCC. **Figure 4.6**(b) shows that fat and sebaceous gland can be easily separated from BCC because they have distinct nucleus and lipid content. **Figure 4.6**(c) (d) demonstrate inflamed dermis/dermis can also be separated from BCC using their distinct differences in nucleus and collagen.

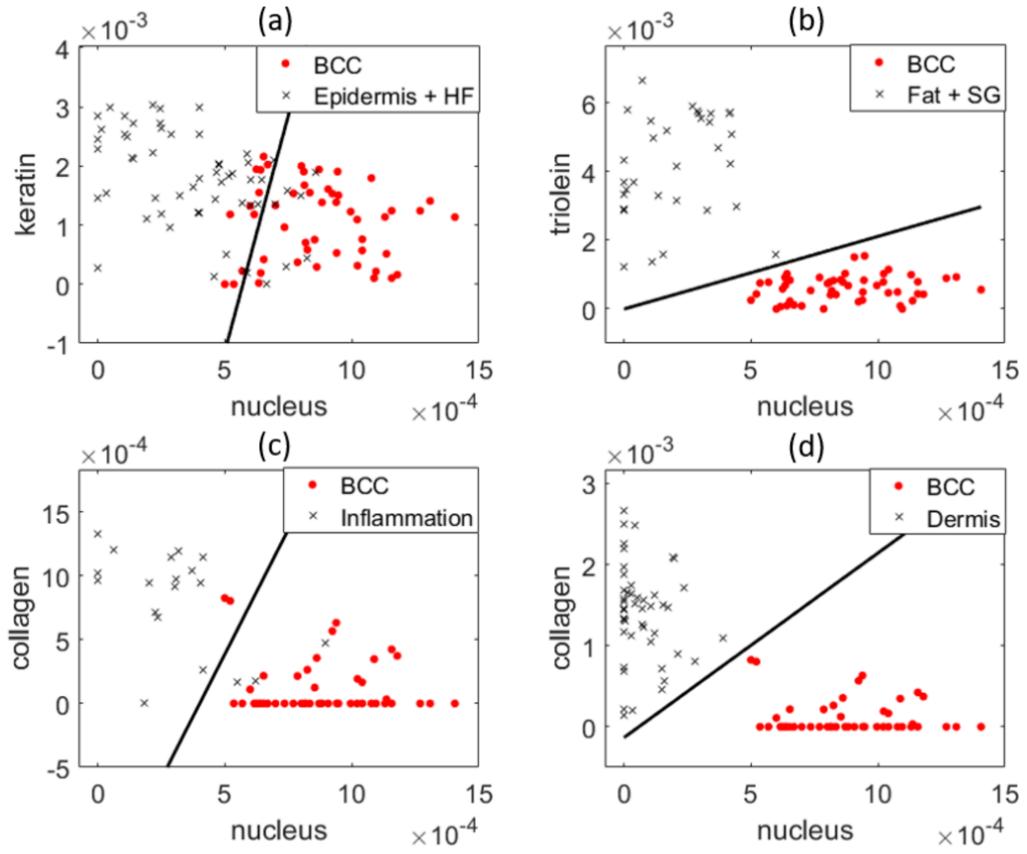

Figure 4.6: Scatter plots demonstrates the performance of two primary model components in discriminating BCC from normal structures. (a) Nucleus and keratin content of BCC, epidermis and HF. (b) Nucleus and triolein content of BCC, fat and SG. (c) Nucleus and ceramide content of BCC and inflamed dermis. (d) Nucleus and collagen content of BCC and dermis. Red dots: BCC. Black crosses: normal tissue structures. Each point represents a spectrum data. The black line is the decision line drawn by logistic regression.

4.4 DISCUSSION AND CONCLUSION

In this chapter, we evaluated the accuracy of Raman to discriminate between BCC and normal skin structures in excised Mohs skin sections. In contrast to previous studies, our discriminatory model was built upon the biochemical differences of Raman active components extracted from a previously developed model [161].

Our results show markedly different biochemical and structural compositions between BCC and normal tissue (**Figure 4.4** and **Table 4.1**). One important finding is that the spectra of BCC has statistically significantly larger contribution of nucleus material compared to normal tissue structures, which is consistent with previous Raman studies [158, 159, 168]. As seen in **Figure 4.2**(b), mean BCC spectra have stronger contribution from 1093, 1577 and 1663 cm^{-1} assigned to nucleus compared to epidermis, hair follicle and inflamed dermis. This is also consistent with the H&E image in **Figure 4.1**(b), where there are smaller amounts of cytoplasm and higher density of cells present in the BCC tumor. Other studies have pointed out similar or increased nucleic contributions in inflamed regions according to the presence of specific Raman bands [151, 162].

Another important finding is that BCC has significantly larger contribution from keratin compared to inflamed/normal dermis, and lower contribution from keratin than epidermis and HF. Keratin is a fibrous structural protein produced by keratinocytes and is abundant in normal epidermis. Keratinocytes are the predominant cells originating in the basal layer between epidermis and dermis, which then move towards the skin surface in a process of maturation and differentiation. The outermost skin layer, stratum corneum, consists about 80% of keratin in dry weight [128]. HF is also rich in keratin. The epithelium of HF forms a cylinder with different concentric layers, including the inner and outer root sheath, with each one expressing a distinct pattern of keratin [169]. Because keratin expression is closely related to differentiation of tumors, it plays a significant role in identifying the origin of BCC. Several studies have discovered that BCC may arise from germinative cells within the basal layer of epidermis or follicular structures [170, 171].

Furthermore, BCC has significantly smaller amounts of collagen and elastin compared to dermis. The difference spectra in **Figure 4.2**(c) shows that BCC spectra have weaker contribution from 856, 940, 1248 cm^{-1} assigned to the vibrational modes of collagen type I and elastin. This is likely the result of the epidermal origin of the BCC, high in cellular content and low in connective tissue. We also found collagen in inflamed dermis is higher than BCC, but lower than normal dermis. This confirms the observation of an early study that a dense inflammatory infiltrate appears to have less collagen than normal dermis [158].

Finally, BCC has significantly larger amount of triolein and ceramide compared to dermis, and larger amount of triolein compared to epidermis. The difference spectrum of BCC and dermis also shows higher contribution at 1080, 1128, 1440 cm^{-1} associated with lipids. A previous biophysical model built upon nonmelanoma skin cancer found an increased contribution of triolein to BCC spectra [65]. Another biophysical model also found an increase in triolein in urological carcinoma lesions [96]. Those studies suggested that maintaining sufficient lipid levels may be necessary to sustain fast tumor growth.

Some normal structures have high biochemical similarity. For instance, the biochemical compositions of epidermis and HF are highly similar, which agrees with the fact that HF is an invagination of normal dermis [160]. As a result, a previous study grouped epidermis and HF together for clustering analysis [151]. The biochemical composition of HS may resemble either HF or SG. This is because HS consists of terminally differentiated keratinocytes that are produced by HF [169], but it is sometimes coated by the sebum secreted by SG [172]. This also explains why the fit coefficients of HS have larger variation compared to the other components. Fat and SG both have low nucleus and high triolein content, so they can be easily discriminated from BCC (**Figure 4.6**(b)).

We evaluated the diagnostic performance by prioritizing either high sensitivity or high specificity (**Table 4.3**). Achieving high specificity is clinically significant in tissue-conserving surgeries such as Mohs, when preserving normal tissue is a critical concern.

Appropriate use criteria of Mohs include tumor location (such as “mask areas” of face), size, and patient type [173]. On the other hand, achieving high sensitivity is more clinically significant when the primary goal is to capture the entire margin based on aggressive growth histology rather than preserving normal tissue.

By prioritizing high sensitivity, we achieved 100% sensitivity and 84% specificity in discriminating BCC from all normal tissue structures. Our results show that that nucleus accounts for most of the discriminant ability. By using the fit coefficient of nucleus alone, 100% of the spectra annotated as dermis (40/40) and fat (10/10) were correctly classified. Most of the spectra annotated as SG (95%, 21/22) and HS (89%, 16/18) were also correctly classified. The misclassification in these latter two categories may be due to unknown tissue structures grouped as the same cluster as SG or HS, leading to high fitting error. On the contrary, HF, epidermis and inflamed dermis were the normal structures that were more easily misclassified as BCC. 16 out of 31 spectra annotated as HF were correctly classified (52%), 20 out of 26 spectra annotated as epidermis were correctly classified (77%), and 16 out of 19 spectra annotated as inflamed dermis were correctly classified (84%).

HF and epidermis were most easily misclassified as BCC. **Figure 4.6**(a) demonstrates that those misclassifications occur due to high nucleus content in some of HF and epidermis. The main reason is that HF may have abundant basal cells in inner and outer root sheath layer, whereas epidermis is rich in basal keratinocyte stem cells in stratum basale layer and polyhedral keratinocytes in stratum spinosum layer. About 16% of inflamed dermis was also misclassified as BCC. Corresponding with the H&E images indicated that inflamed dermis regions have higher number of nucleus than normal dermis, so their spectra were more similar to BCC than normal dermis.

By prioritizing high specificity, we achieved 99% specificity, 52% sensitivity and 93% PPV. High specificity indicates a region has high risk, so a dermatologist could remove more tissue from the corresponding region with high confidence of it being tumor [174]. In a Mohs guidance setting, this approach could reduce the number of skin samples processed for histopathology. The dermatologist would still make a histopathological

diagnosis on the final stage to ensure all the tumors are entirely removed; thus, one may be able to tolerate lower sensitivity. Ultimately, this system would need to be tested in an intraoperative setting to determine its impact on reducing the number of tissue samples needing histology processing. Our results showed 24 out of 50 spectra annotated as BCC were misclassified as normal structures. All the spectra annotated as dermis, HF, HS, SG and fat were classified correctly. Most of the spectra annotated as inflamed dermis (95%, 18/19) and epidermis (96%, 25/26) were correctly classified.

Although we have demonstrated Raman microscopy is highly accurate in evaluating skin tumor surgical margin, one major limitation is lengthy acquisition time. To raster scan a tissue $1mm^2$ in size, it would take around 10 – 20 hours, making it unpractical for intraoperative use. To overcome this limitation, several wide-field imaging techniques could be employed. Kong *et al*. integrated Raman microscopy with tissue autofluorescence imaging and achieved one or two orders of magnitude faster speed [151]. Karen *et al*. developed fluorescence confocal mosaicking microscopy and proved its potential for rapid assessment of BCC margins during Mohs [175]. Flores *et al* used fluorescence confocal mosaicking microscopy to enable rapid detection of residual tumor directly in the surgical wounds on patients [18]. Further directions for this work include speeding up Raman acquisition without losing molecular specificity, and combining Raman spectroscopy with wide-field imaging technique for fast intraoperative surgical guidance.

Chapter 5: Superpixel Raman spectroscopy for rapid skin cancer surgical margin assessment

5.1 Background

Although confocal Raman microscope has demonstrated high accuracy in detecting tumor margin, one major challenge is the acquisition speed is slow. A good signal-to-noise ratio spectrum typically takes 1 second in tissue; thus, to scan a centimeter scale sample would take hours or even days. This makes histopathology impractical for use during surgery for most cancer types. As a result, this chapter centers on expediting the acquisition speed of Raman spectroscopy for cancer margin detection.

5.2 Basic Principle of Superpixel Acquisition

We describe a superpixel acquisition method for rapid human skin cancer margin assessment. **Figure 5.1** demonstrates its basic principle. While sparse point-by-point scanning requires 1s for each pixel, superpixel acquisition only takes 1s for the whole area, thus substantially speeding up the acquisition. When the laser spot size is 1μm and superpixel size is 100μm, speed gain would be 10,000x.

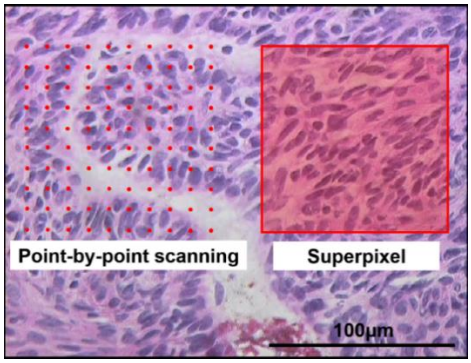

Figure 5.1: Comparison between sparse point-by-point scanning and superpixel imaging.

As seen in **Figure 5.2**, a tradeoff exists between speed up factor and spatial resolution. Our preliminary superpixel acquisition data were obtained based on 100μm superpixel size, because reasonable resections are a least a few hundreds of microns. In the future, we will perform experiment on different superpixel sizes to determine the optimum size.

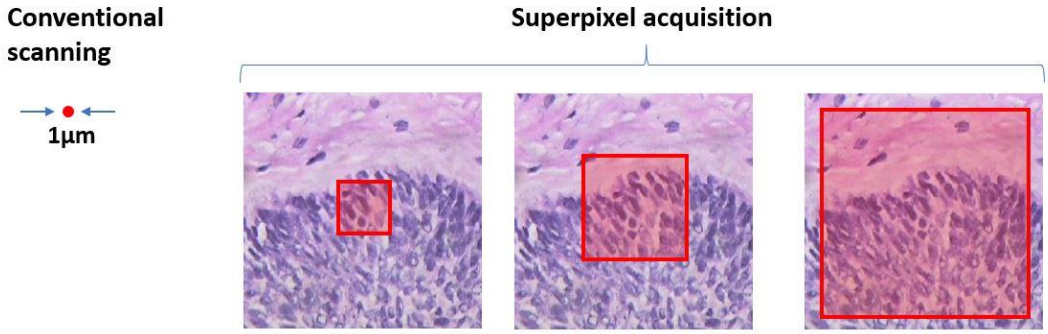

Superpixel size (μm)	25	50	100
Resolution (cells)	10	25	100
Speed up factor	625x	2,500x	10,000x

Figure 5.2: Tradeoff between superpixel size and speed up factor. Here show three different sizes: 25μm, 50μm, and 100μm.

5.3 Preliminary Results of Superpixel Acquisition

We have obtained some preliminary results on both tissue-simulating phantom and human skin samples. **Figure 5.3(a)** shows an example experiment on a basal cell carcinoma (BCC) section. We sampled on both BCC and normal tissue structures (epidermis, dermis, inflamed dermis, hair follicle, hair shaft, sebaceous gland, and fat). In total, we collected data from 154 sites from 10 samples in 8 patients undergoing Mohs surgery. We then applied the biophysical inverse model to the average tissue spectra and extracted the concentration of the biomarkers. Finally, we used the diagnostic model described in **Chapter 4** to classify BCC from normal tissue structures. Our initial results demonstrated

that the optimum classification result can be achieved by combining the biochemical changes of nucleus, collagen, keratin, and ceramide. **Figure 5.3(b)** showed that superpixel acquisition has consistent diagnostic performance as compared to point-by-point scanning.

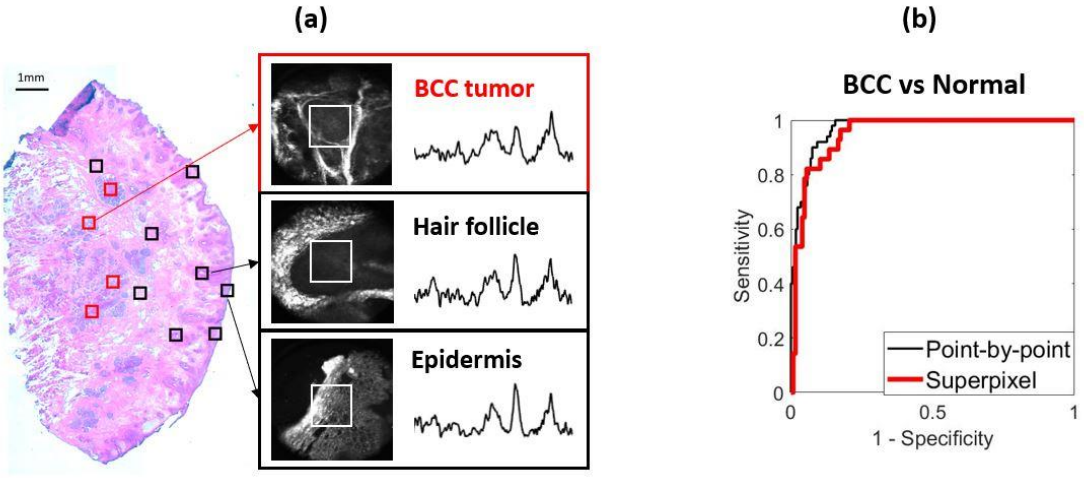

Figure 5.3: (a) Example of superpixel experiment on a basal cell carcinoma (BCC) section. From each superpixel ($100\times100\mu m^2$), we generated one average Raman spectrum. The reflectance confocal images and average tissue spectra are shown on the right. The white squares label the location of the superpixel ($100\times100\mu m^2$). (b) ROC curves of superpixel acquisition versus point-by-point scanning.

5.4 SUPERPIXEL IMAGING

5.4.1 Instrumentation

After demonstrating the capability of superpixel acquisition, our next step is to perform superpixel imaging on a large field of view (e.g. $1\times1mm^2$). Our previous system only allows for scanning a maximum of $300\times300\mu m^2$ by steering the laser beam using 2D galvanometer mirrors. Therefore, we added a 2D motorized translation stage to translate the sample. **Figure 5.4** compares the optical system before and after adaption. We changed

the system from inverted objective setup to upright setup due to the mechanical restraint of the motorized stages. However, in our future work we will replace it with a high-speed linear stage (e.g. HLD117, Prior Scientific [33]), which has a fast translation speed, and can be easily mounted on a commercial microscope base. Another system upgrade in the future is adding autofocusing in the z axis [33]. For the preliminary study, we placed a quartz slide on the top of the sample to improve surface flatness. However, the image blurs when the stage moves a few millimeters. An autofocusing algorithm would keep the sample within focus at all times, enabling a larger scan area. **Appendix D Table D.1** summarizes the key components of this system.

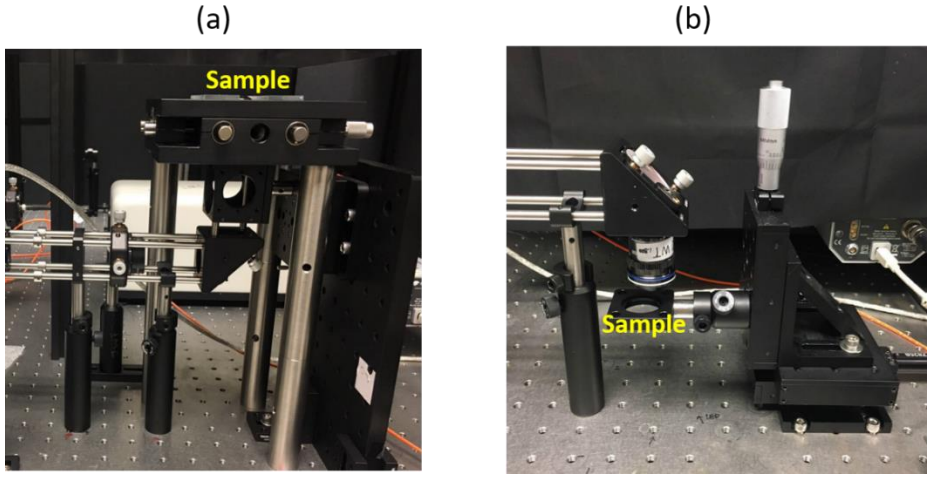

Figure 5.4: (a) Previous system (inverted objective setup, the tissue is stationary). (b) Current system (upright objective setup, the tissue is mounted on a 2D motorized translation stage). (b) is adapted from (a) for superpixel imaging.

Figure 5.5 displays the LabVIEW program for automated superpixel imaging. The user records the X and Y value of the initial position, defines the size of the superpixel (25, 50, 75, or 100 μm), the number of steps, and the integration time. Once click "Run", the galvanometer mirrors will scan continuously to generate the superpixel, and the reflectance

confocal image will be displayed and saved in real time. Meanwhile, the motorized stage will translate the sample in 2D, and the CCD camera will capture one spectrum for each step. To repeat the measurement for the same region, the user only needs to move the motorized stage back to its original X and Y position.

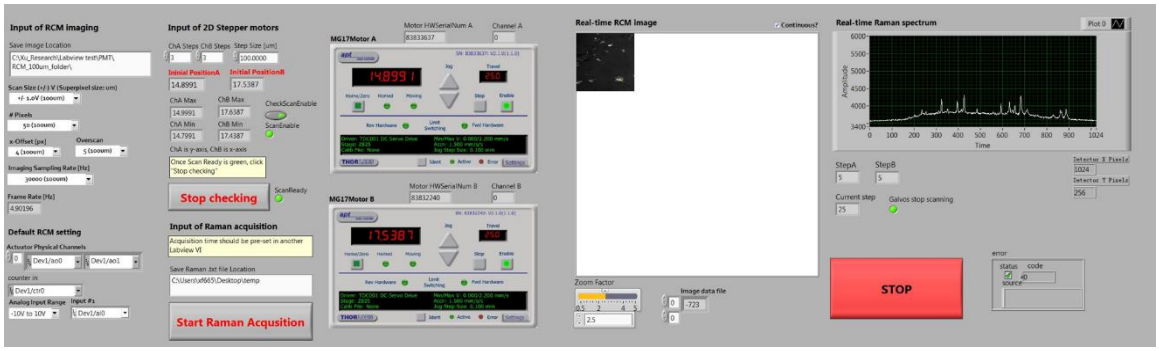

Figure 5.5: LabVIEW program for automated superpixel imaging.

5.4.2 experiment

In **Figure 5.6**, we imaged two Mohs surgical specimens, one positive margin and one negative margin. The positive margin contains basal cell carcinoma and normal tissue, and the negative margin contains only normal tissue. We tested three superpixel sizes within the same 1×1mm^2 area. A prior classification model was applied to each superpixel, labeling each superpixel as positive or negative. The results showed Raman correctly classified most of the positive and negative margins for the 100 μm, 50 μm and 25 μm superpixel images. In the future, we will collect more superpixel images, and correlate each pixel with the ground truth diagnosis. We will then optimize the classification model to improve the diagnostic performance.

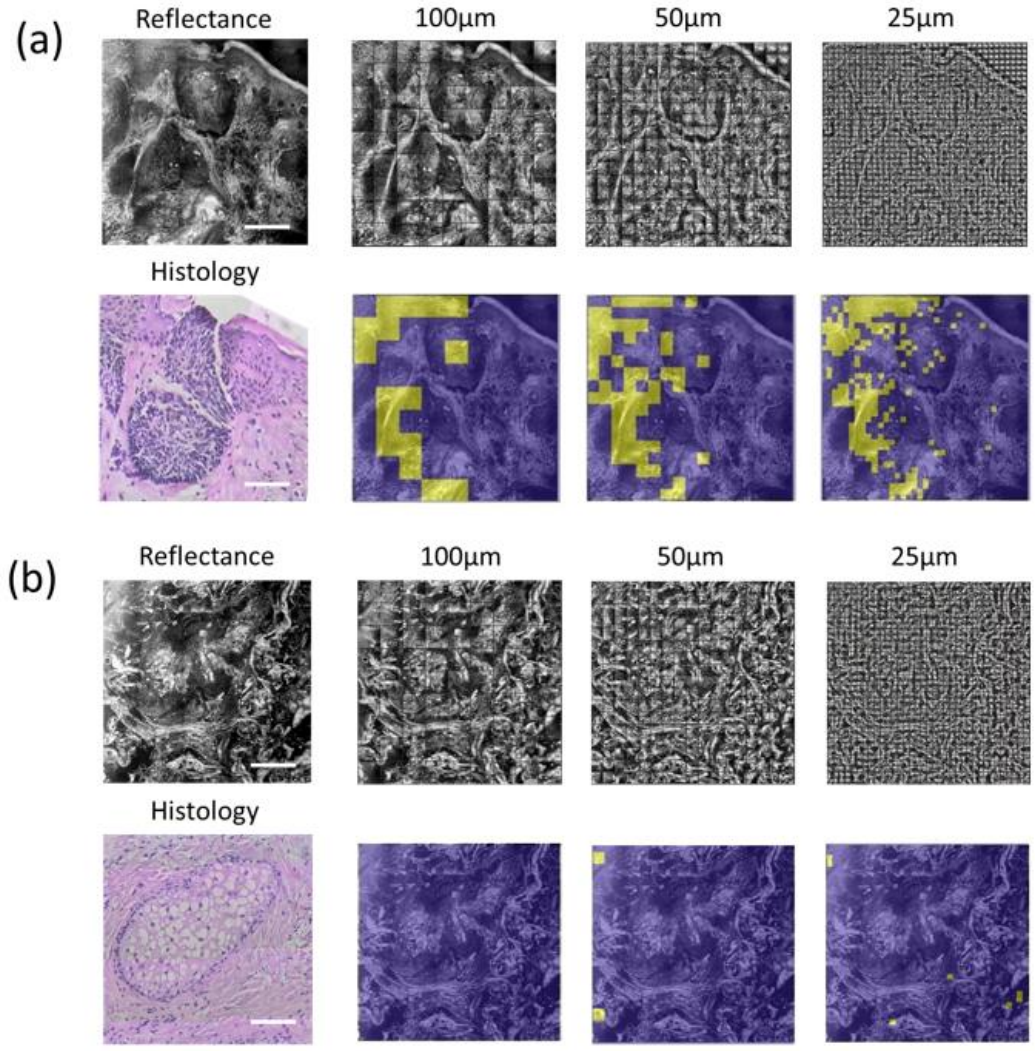

Figure 5.6: An example superpixel imaging experiment. (a) Positive margin. (b) Negative margin. Three superpixel sizes were tested: 100µm, 50µm, and 25µm. The classification maps shown here targeted at high specificity. Yellow: positive. Blue: negative. Scale bar: 200µm.

Chapter 6: Conclusion

The goal of this dissertation is to explore the biophysical origin of skin cancer detection using Raman spectroscopy. We built a mathematical inverse model (**Chapter 2**) and demonstrated that Raman spectroscopy is a promising tool for early cancer screening (**Chapter 3**), and surgical guidance of tumor margin delineation (**Chapter 4 & 5**).

Our previous clinical study showed that Raman spectroscopy has high accuracy in detecting malignant melanoma, the deadliest version of skin cancer. However, the statistical method we used for classification does not reveal the key diagnostic markers that Raman spectroscopy relies on to make an accurate diagnosis. Therefore, we built a biophysical inverse Raman model using eight primary Raman active biomarkers, including proteins (collagen, elastin, keratin), lipids (ceramide, triolein), cell nucleus, pigment (melanin), and water. We found those biomarkers are the most relevant in describing the spectral differences between normal skin and various diseased states.

For *in vivo* melanoma detection, we concluded that collagen and triolein are the two primary diagnostic markers. An interesting result we found is that the decrease of triolein (or subcutaneous fat) signal in melanoma is partially due to the epidermal thickening effect. Thickened epithelium prevents light from entering deeper layer of the skin, leading to a substantial decrease of Raman emission from fat. The biophysical changes we observed is based on our non-confocal probe, which has a relatively large tissue probing volume and deep tissue interrogation. It is worth noticing that the biophysical changes detected by Raman spectroscopy may vary depending on the probe design, as discussed by the Huang group [176]; however, the eight Raman active components will not change with the probe design. To further improve our study, we can include patient information in the diagnostic model (gender, race, family history, etc.), and confirm the biophysical changes (such as the epidermal thickening process) from histopathology and other optical imaging modalities (such as optical coherence tomography).

For *ex vivo* surgical margin detection, our results showed that Raman spectroscopy is highly accurate in discriminating basal cell carcinoma. Significant differences were

observed for nucleus, keratin, collagen, triolein, and ceramide content between basal cell carcinoma and surrounding normal tissue structures. Particularly, nucleus accounted for most of the discriminant power. We also highlighted a few classification tasks that the dermatologists are mostly interested, such as basal cell carcinoma versus epidermis and hair follicle, and basal cell carcinoma versus normal and inflamed dermis. Our results indicated that epidermis and hair follicle are mostly easily misclassified as basal cell carcinoma, especially in regions where the nucleus content is high. Besides, inflamed dermis has an increased amount of nucleus, and decreased amount of collagen compared to normal dermis. These results are consistent with standard histopathological diagnosis.

Finally, we described a superpixel acquisition approach for rapid human skin cancer surgical margin assessment. We envision this approach being used to develop an accurate, inexpensive, and efficient cancer imaging device, to aid Mohs surgeons and general practitioners in skin margin assessment during surgery.

Appendices

APPENDIX A: SYSTEM CHARACTERIZATION

A.1 Confocal Raman Microscope

Lateral, axial, and spectral resolution of the confocal Raman microscope is 1μm, 8μm, 8 cm^{-1}, respectively. System was characterized using the method described in Reference [177].

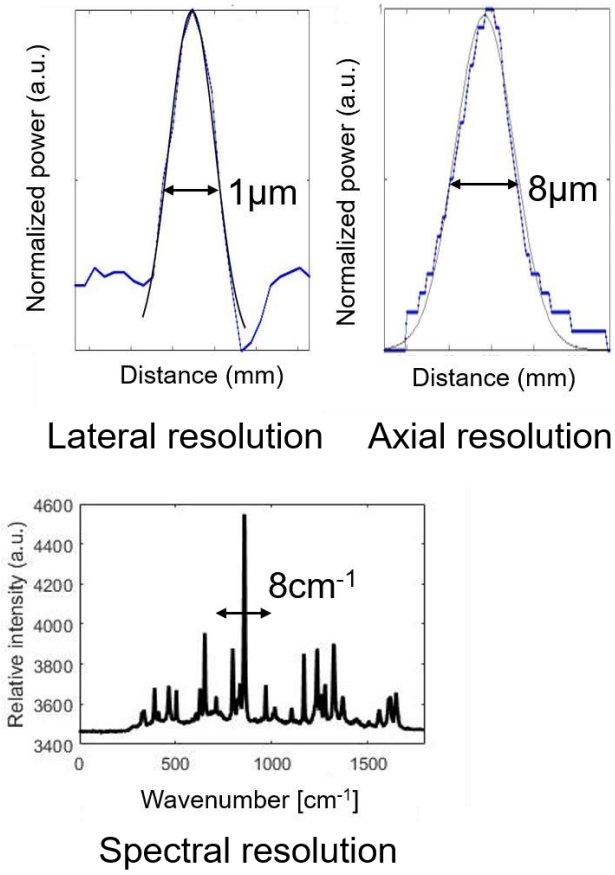

Figure A.1: Lateral, axial, and spectral resolution of the confocal Raman microscope.

A.2 Reflectance Confocal Microscope (RCM)

The maximum field of view of reflectance confocal microscope (RCM) is 300μm in diameter, as shown in **Figure A.2**. The field of view is limited by the aperture of the scanning lens. Currently, two achromatic doublets act as the scanning lens and tube lens to conjugate the 2D galvanometer mirrors to the back aperture of the microscope objective. However, a doublet has limited aperture and severe optical aberrations on the periphery of the image. Therefore, only the central 200×200 μm^2 region is used. In our future work, we should replace the doublet with a scanning lens or F-theta lens.

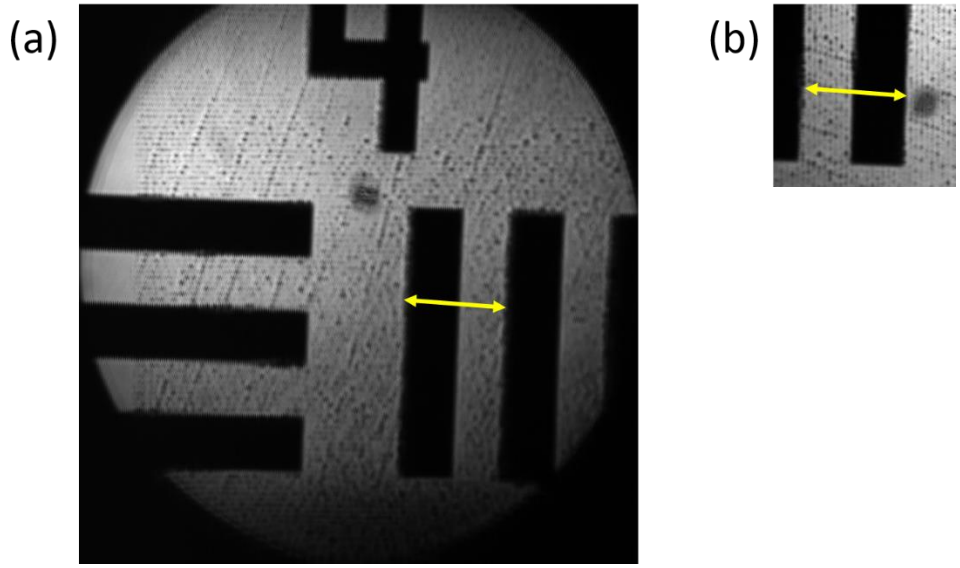

Figure A.2: Characterizing the field of view of RCM image using an USAF 1951 resolution target. A neural density filter with OD = 2.0 was used to attenuate the laser power to ~1% to prevent damage to the coating of the resolution target. The voltage of the current preamplifier was increased from 0.48V to 0.65V. Group 4 element 2 corresponds to 17.96 line pairs per mm (arrow). (a) +/- 3.0V input voltage. (b) +/- 1.0V input voltage. (b) is a 100×100μm^2 superpixel.

The lateral resolution of RCM is better than 1μm, as seen from **Figure A.3**. Individual polystyrene beads can be clearly resolved.

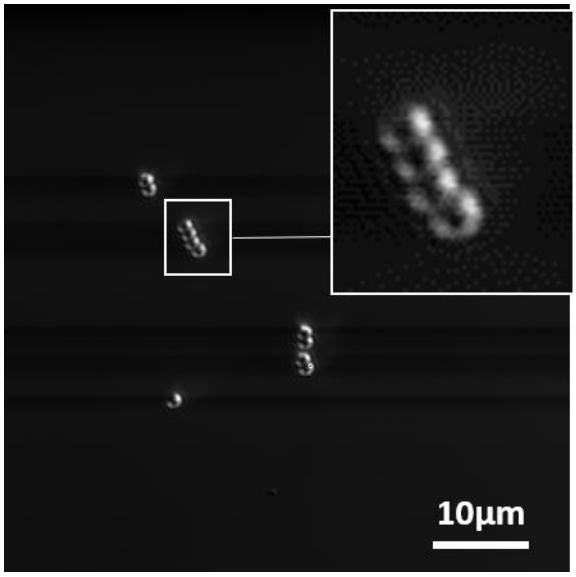

Figure A.3: Characterizing the lateral resolution of RCM using 1μm polystyrene beads.

APPENDIX B: RCM IMAGE OF SKIN

B.1 RCM Image of Tissue Sections

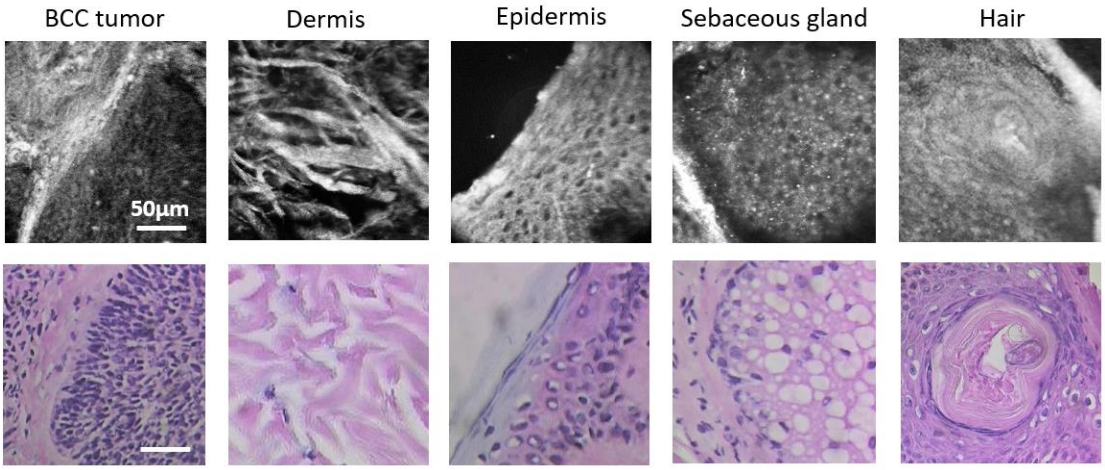

Figure B.1: RCM images of various tissue structures on Mohs skin sections. Each image has a size of 200×200µm^2.

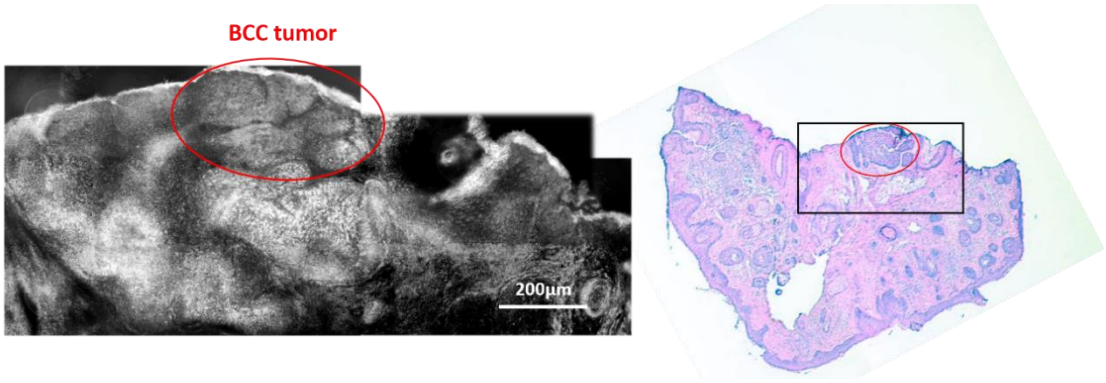

Figure B.2: Left: RCM image of a basal cell carcinoma (BCC) section. Right: H&E stained image of the serial section. BCC tumor is highlighted in red in both images. The RCM images were stitched together using Microsoft Image Composite Editor (ICE).

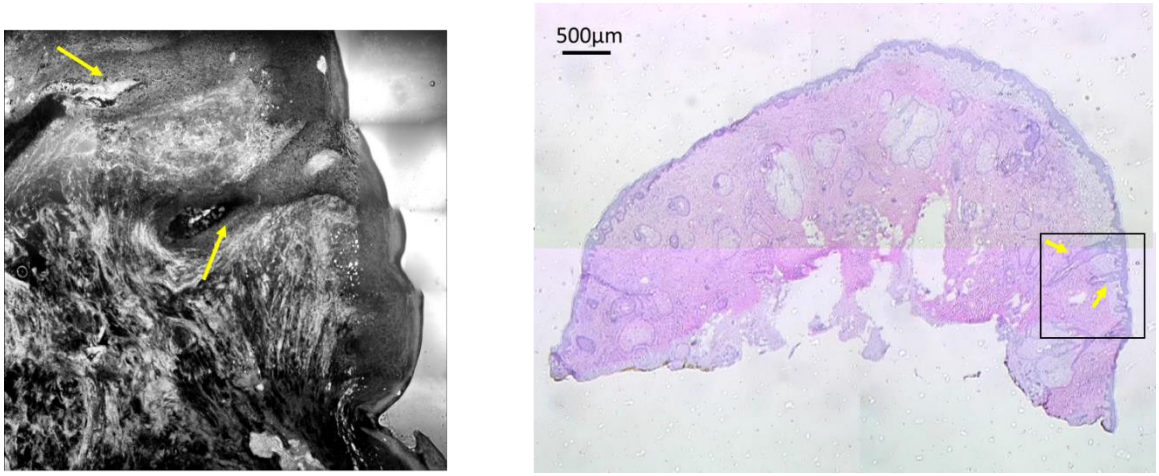

Figure B.3: Left: RCM image of a normal section. Right: H&E stained image of the serial section. Two hair follicles can be clearly identified from the image (yellow arrows).

B.2 RCM Image of Unsectioned Tissue Blocks

RCM images can be obtained directly from the unsectioned tissue blocks. This indicates that diagnosis can be obtained directly by analyzing the surface of tissue blocks removed during surgery without cutting thin sections [151]. In **Figure B.4**, stratum corneum and dermis can be clearly identified from a skin tissue block. The RCM image of stratum corneum matches with a previous study [42].

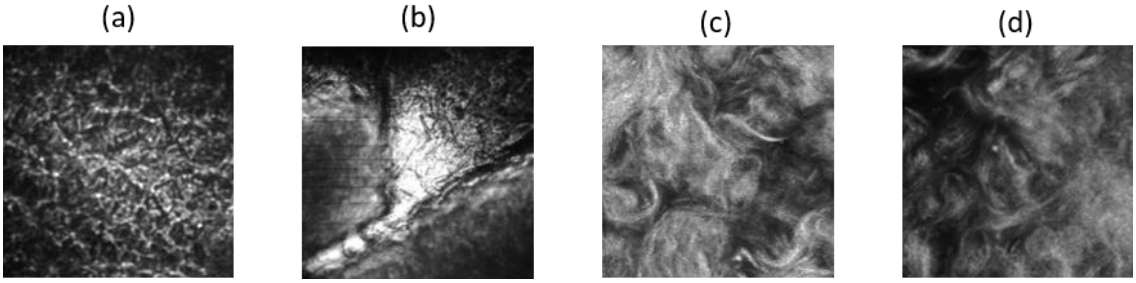

Figure B.4: RCM image of a skin tissue block. (a) (b) Stratum corneum side. (c) (d) Dermal side.

APPENDIX C: RCM VS TWO-PHOTON-EXCITED FLUORESCENCE IMAGE

High correlation is found between RCM image and two-photon-excited fluorescence (TPEF) image, as shown in **Figure B.5**.

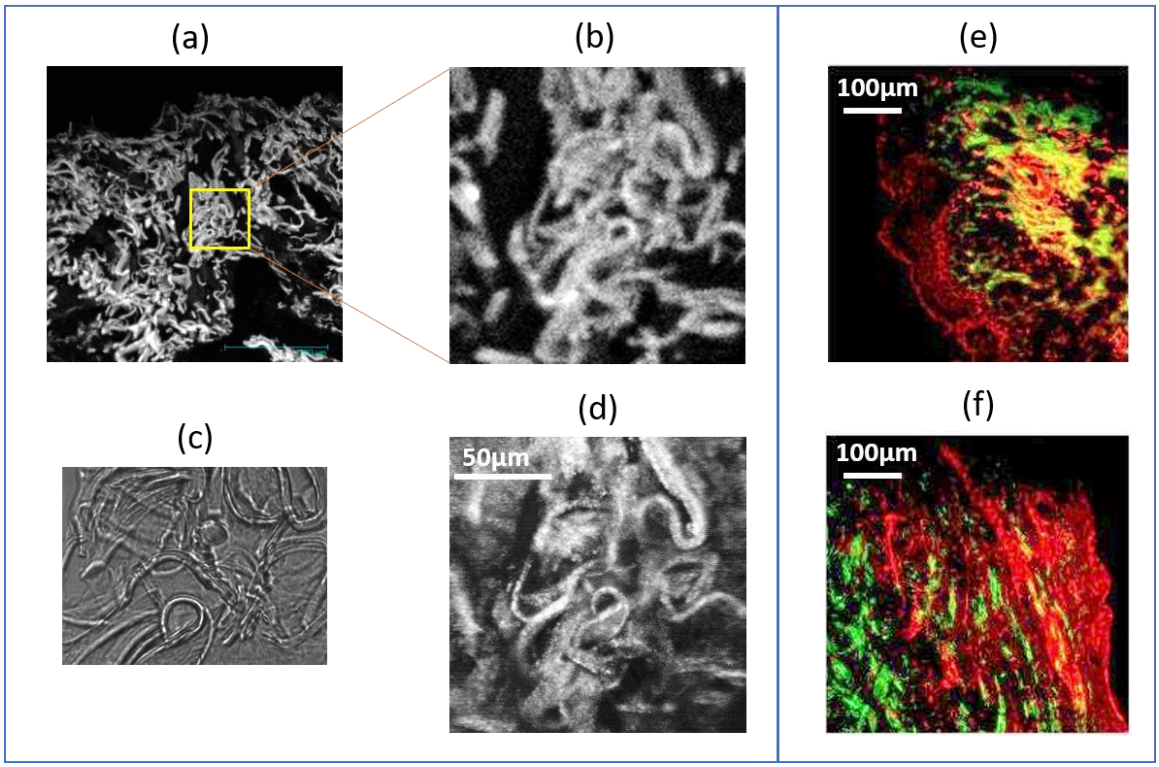

Figure B.5: Comparison between RCM and TPEF image. (a) TPEF image of a human skin section. (b) Zoom-in. Excitation wavelength: 820nm. Objective lens 20x. (c) Bright-field image. (d) RCM image. Comparison is also made between TPEF image of (e) human skin and (f) porcine skin. Red: keratin (excitation: 780nm, emission: 525±35nm). Green: collagen (excitation: 1020nm, emission: 525±35nm).

APPENDIX D: COMPLETE LIST OF SYSTEM COMPONENTS

Table D.1 A summary of the system components. Hardware abbreviations can be found in **Figure 2.1**.

Hardware	Description	Part Number	Manufacturer
Laser	830nm free-space single mode diode laser, maximum power 200mW	LM830-PLR 200 The new version was degraded to 170mw	Ondax
CF	830nm Maxline laser clean-up filter	LL01-830-25	Semrock
OI	Free space isolator, 830nm	IO-3D-830-VLP	Thorlabs
Mirrors	Protected silver mirror, 1”	ME1-P01	Thorlabs
SF	Spatial filter system (L1, P1, & L2)	KT310	Thorlabs
L1	Aspheric lens, f = 11mm	A397TM-B	Thorlabs
P1	25um pinhole	P25S	Thorlabs
L2	Achromatic doublet, f = 25mm	AC254-025-B-ML	Thorlabs
D1, D2	830 nm LPF, RazorEdge Dichroic laser-flat beamsplitter	LPD01-830RU-25x36x2.0	Semrock
GM	2D small beam diameter (<5mm) scanning galvo mirror systems	GVSM002	Thorlabs
L3	Achromatic doublet, f = 100mm	AC254-100-B-ML	Thorlabs
L4	Achromatic doublet, f = 200mm	AC254-200-B-ML	Thorlabs
FM	30 mm Cage Cube-Mounted Non-Polarizing Beamsplitter, 700 - 1100 nm, 50:50 split ratio	CM1-BS014	Thorlabs

Table D.1 Continued.

Microscope objective	60x, NA = 1.2, WD = 0.28mm, water	UPLSAPO60XW IR	Olympus
Low bgd Raman substrate	Magnesium fluoride window	64-094	Edmund Optics
Low bgd Raman substrate (for cell study)	Quartz cover slip for microscope slide, fused, 1" dia, 0.15-0.25mm thick	43211	Alfa Aesar
Sample stage (manual translation), used for inverted objective setup	Aperture platform two-Axis linear stage, 1/4-20 with two vernier micrometer, 13 mm Travel	406 with SM-13	New Focus
CMOS	MP monochrome CMOS camera, 12-bit	BTE-B050-U	Mightex
Motorized Stage	2-axis 1" motorized translation stage	PT1-Z8	Thorlabs
Axial translation (manual)	1" Translation Stage with Standard Micrometer	PT1	Thorlabs
Notch filter	830nm, 25mm Diameter, OD 4 Notch Filter	86-703	Edmund Optics
L5, L6	Aspheric lens	f = 18.4mm	Thorlabs
P2, P3	50um fiber, NA = 0.22, multi-mode, Low OH	M14L01	Thorlabs
Spectrograph	Holographic Imaging Spectrograph	HoloSpec f/1.8i - NIR	Kaiser Optical Systems
CCD	Back-illuminated deep-depletion CCD, Broad band UV-Near IR detection, 1024x256 pixels	Andor iDus 420, DU420ABEXDD	Oxford Instruments
Current preamplifier	Low noise current preamplifier	SR570	Stanford Research Systems

Table D.1 Continued.

DAQ board	Data acquisition board	PCIe-6351	National Instruments
Future work			
Axial translation (autofocusing)	NanoFlex 5 mm Translation Stage with Diff. Drive and Piezo	NFL5DP20 (already purchased)	Thorlabs
High-speed linear stage	ProScan 121mm x 81mm travel DC linear motor stage for inverted microscope	HLD117NN	Prior Scientific

References

1. R. L. Siegel, K. D. Miller, and A. Jemal, "Cancer statistics, 2016," CA: a cancer journal for clinicians **66**, 7-30 (2016).
2. C. A. Lieber, S. K. Majumder, D. L. Ellis, D. D. Billheimer, and A. Mahadevan-Jansen, "In vivo nonmelanoma skin cancer diagnosis using Raman microspectroscopy," Lasers in Surgery and Medicine **40**, 461-467 (2008).
3. I. P. Santos, P. J. Caspers, T. C. B. Schut, R. van Doorn, V. N. Hegt, S. Koljenovic, and G. J. Puppels, "Raman Spectroscopic Characterization of Melanoma and Benign Melanocytic Lesions Suspected of Melanoma Using High-Wavenumber Raman Spectroscopy," Analytical Chemistry **88**, 7683-7688 (2016).
4. H. Lui, J. Zhao, D. McLean, and H. Zeng, "Real-time Raman spectroscopy for in vivo skin cancer diagnosis," Cancer research **72**, 2491-2500 (2012).
5. D. R. English, C. Del Mar, and R. C. Burton, "Factors influencing the number needed to excise: excision rates of pigmented lesions by general practitioners," Medical journal of Australia **180**, 16-19 (2004).
6. I. P. Santos, R. van Doorn, P. J. Caspers, T. C. B. Schut, E. M. Barroso, T. E. Nijsten, V. N. Hegt, S. Koljenović, and G. J. Puppels, "Improving clinical diagnosis of early-stage cutaneous melanoma based on Raman spectroscopy," British journal of cancer **119**, 1339 (2018).
7. C. Hansen, D. Wilkinson, M. Hansen, and G. Argenziano, "How good are skin cancer clinics at melanoma detection? Number needed to treat variability across a national clinic group in Australia," Journal of the American Academy of Dermatology **61**, 599-604 (2009).
8. K. Nelson, S. M. Swetter, S. Chen, and C. Curiel-Lewandrowski, "The estimated financial impact of diagnostic accuracy on melanoma diagnosis in 2018," (American Society of Clinical Oncology, 2018).
9. T. A. C. S. m. a. e. c. team, "Treatment of Melanoma Skin Cancer, by Stage" (American Cancer Society, 2018), retrieved 2019, https://www.cancer.org/cancer/melanoma-skin-cancer/treating/by-stage.html.
10. "Treatments for non-melanoma skin cancer" (Canadian Cancer Society, 2019), retrieved 2019, https://www.cancer.ca/en/cancer-information/cancer-type/skin-non-melanoma/treatment/?region=on.
11. K. Mosterd, G. A. Krekels, F. H. Nieman, J. U. Ostertag, B. A. Essers, C. D. Dirksen, P. M. Steijlen, A. Vermeulen, H. Neumann, and N. W. Kelleners-Smeets, "Surgical excision versus Mohs' micrographic surgery for primary and recurrent basal-cell carcinoma of the face: a prospective randomised controlled trial with 5-years' follow-up," The lancet oncology **9**, 1149-1156 (2008).
12. M. S. Tobias Meyer, Orlando Guntinas-Lichius and Jürgen Popp, "Toward an All-Optical Biopsy," Optics & Photonics News (2019).

13. A. I. Henry, B. Sharma, M. F. Cardinal, D. Kurouski, and R. P. Van Duyne, "Surface-Enhanced Raman Spectroscopy Biosensing: In Vivo Diagnostics and Multimodal Imaging," Analytical Chemistry **88**, 6638-6647 (2016).
14. S. Laing, K. Gracie, and K. Faulds, "Multiplex in vitro detection using SERS," Chemical Society Reviews **45**, 1901-1918 (2016).
15. S. Laing, L. E. Jamieson, K. Faulds, and D. Graham, "Surface-enhanced Raman spectroscopy for in vivo biosensing," Nature Reviews Chemistry **1**, 0060 (2017).
16. V. Ahlgrimm-Siess, M. Laimer, H. S. Rabinovitz, M. Oliviero, R. Hofmann-Wellenhof, A. A. Marghoob, and A. Scope, "Confocal microscopy in skin cancer," Current dermatology reports **7**, 105-118 (2018).
17. A. Scope, U. Mahmood, D. Gareau, M. Kenkre, J. Lieb, K. Nehal, and M. Rajadhyaksha, "In vivo reflectance confocal microscopy of shave biopsy wounds: feasibility of intraoperative mapping of cancer margins," British Journal of Dermatology **163**, 1218-1228 (2010).
18. E. S. Flores, M. Cordova, K. Kose, W. Phillips, A. Rossi, K. S. Nehal, and M. Rajadhyaksha, "Intraoperative imaging during Mohs surgery with reflectance confocal microscopy: initial clinical experience," J Biomed Opt **20**, 061103 (2015).
19. P. Guitera, G. Pellacani, C. Longo, S. Seidenari, M. Avramidis, and S. W. Menzies, "In Vivo Reflectance Confocal Microscopy Enhances Secondary Evaluation of Melanocytic Lesions," J Invest Dermatol **129**, 131-138 (2009).
20. B. Larson, S. Abeytunge, E. Seltzer, M. Rajadhyaksha, and K. Nehal, "Detection of skin cancer margins in Mohs excisions with high‐speed strip mosaicing confocal microscopy: a feasibility study," British Journal of Dermatology **169**, 922-926 (2013).
21. A. Levine, K. Wang, and O. Markowitz, "Optical coherence tomography in the diagnosis of skin cancer," Dermatologic clinics **35**, 465-488 (2017).
22. R. Pomerantz, D. Zell, G. McKenzie, and D. M. Siegel, "Optical coherence tomography used as a modality to delineate basal cell carcinoma prior to Mohs micrographic surgery," Case reports in dermatology **3**, 212-218 (2011).
23. N. Reddy and B. Nguyen, "The utility of optical coherence tomography for diagnosis of basal cell carcinoma: a quantitative review," British Journal of Dermatology (2018).
24. N. Iftimia, O. Yélamos, C.-S. J. Chen, G. Maguluri, M. A. Cordova, A. Sahu, J. Park, W. Fox, C. Alessi-Fox, and M. Rajadhyaksha, "Handheld optical coherence tomography–reflectance confocal microscopy probe for detection of basal cell carcinoma and delineation of margins," J Biomed Opt **22**, 076006 (2017).
25. J. Wang, Y. Xu, and S. A. Boppart, "Review of optical coherence tomography in oncology," J Biomed Opt **22**, 121711 (2017).
26. S. Heuke, N. Vogler, T. Meyer, D. Akimov, F. Kluschke, H.-J. Rowert-Huber, J. Lademann, B. Dietzek, and J. Popp, "Detection and Discrimination of Non-Melanoma Skin Cancer by Multimodal Imaging," Healthcare (Basel, Switzerland) **1**, 64-83 (2013).

27. S. W. Perry, R. M. Burke, and E. B. Brown, "Two-photon and second harmonic microscopy in clinical and translational cancer research," Annals of biomedical engineering **40**, 277-291 (2012).
28. S. You, H. Tu, E. J. Chaney, Y. Sun, Y. Zhao, A. J. Bower, Y.-Z. Liu, M. Marjanovic, S. Sinha, and Y. Pu, "Intravital imaging by simultaneous label-free autofluorescence-multiharmonic microscopy," Nature communications **9**, 2125 (2018).
29. N. Rajaram, J. S. Reichenberg, M. R. Migden, T. H. Nguyen, and J. W. Tunnell, "Pilot clinical study for quantitative spectral diagnosis of non‐melanoma skin cancer," Lasers in surgery and medicine **42**, 876-887 (2010).
30. A. Garcia-Uribe, J. Zou, M. Duvic, J. H. Cho-Vega, V. G. Prieto, and L. V. Wang, "In vivo diagnosis of melanoma and nonmelanoma skin cancer using oblique incidence diffuse reflectance spectrometry," Cancer research **72**, 2738-2745 (2012).
31. K. A. Chan and S. G. Kazarian, "Attenuated total reflection Fourier-transform infrared (ATR-FTIR) imaging of tissues and live cells," Chemical Society Reviews **45**, 1850-1864 (2016).
32. C. Krafft and V. Sergo, "Biomedical applications of Raman and infrared spectroscopy to diagnose tissues," Spectroscopy-an International Journal **20**, 195-218 (2006).
33. S. Mittal, K. Yeh, L. S. Leslie, S. Kenkel, A. Kajdacsy-Balla, and R. Bhargava, "Simultaneous cancer and tumor microenvironment subtyping using confocal infrared microscopy for all-digital molecular histopathology," Proceedings of the National Academy of Sciences **115**, E5651-E5660 (2018).
34. R. Bhargava, "Towards a practical Fourier transform infrared chemical imaging protocol for cancer histopathology," Analytical and bioanalytical chemistry **389**, 1155-1169 (2007).
35. C. V. Raman and K. S. Krishnan, "A new type of secondary radiation," Nature **121**, 501 (1928).
36. R. Lord and N.-T. Yu, "Laser-excited Raman spectroscopy of biomolecules: I. Native lysozyme and its constituent amino acids," Journal of molecular biology **50**, 509-524 (1970).
37. K. Kochan, E. Maslak, C. Krafft, R. Kostogrys, S. Chlopicki, and M. Baranska, "Raman spectroscopy analysis of lipid droplets content, distribution and saturation level in Non‐Alcoholic Fatty Liver Disease in mice," Journal of biophotonics **8**, 597-609 (2015).
38. K. Kochan, K. M. Marzec, K. Chruszcz-Lipska, A. Jasztal, E. Maslak, H. Musiolik, S. Chłopicki, and M. Baranska, "Pathological changes in the biochemical profile of the liver in atherosclerosis and diabetes assessed by Raman spectroscopy," Analyst **138**, 3885-3890 (2013).
39. N. Bergner, A. Medyukhina, K. D. Geiger, M. Kirsch, G. Schackert, C. Krafft, and J. Popp, "Hyperspectral unmixing of Raman micro-images for assessment of

morphological and chemical parameters in non-dried brain tumor specimens," Analytical and bioanalytical chemistry **405**, 8719-8728 (2013).
40. I. Pence and A. Mahadevan-Jansen, "Clinical instrumentation and applications of Raman spectroscopy," Chemical Society Reviews **45**, 1958-1979 (2016).
41. M. Jermyn, J. Desroches, K. Aubertin, K. St-Arnaud, W.-J. Madore, E. De Montigny, M.-C. Guiot, D. Trudel, B. C. Wilson, and K. Petrecca, "A review of Raman spectroscopy advances with an emphasis on clinical translation challenges in oncology," Physics in Medicine and Biology **61**, R370 (2016).
42. P. Caspers, G. Lucassen, and G. Puppels, "Combined in vivo confocal Raman spectroscopy and confocal microscopy of human skin," Biophysical journal **85**, 572-580 (2003).
43. T. W. Bocklitz, F. S. Salah, N. Vogler, S. Heuke, O. Chernavskaia, C. Schmidt, M. J. Waldner, F. R. Greten, R. Bräuer, and M. Schmitt, "Pseudo-HE images derived from CARS/TPEF/SHG multimodal imaging in combination with Raman-spectroscopy as a pathological screening tool," Bmc Cancer **16**, 534 (2016).
44. V. Zakharov, I. Bratchenko, S. Kozlov, A. Moryatov, D. Kornilin, O. Myakinin, and D. Artemyev, "Advances in tumor diagnosis using OCT and Raman spectroscopy," in *Biophotonics: Photonic Solutions for Better Health Care IV*, (International Society for Optics and Photonics, 2014), 91290L.
45. C. A. Patil, H. Kirshnamoorthi, D. L. Ellis, T. G. van Leeuwen, and A. Mahadevan‐Jansen, "A clinical instrument for combined raman spectroscopy‐optical coherence tomography of skin cancers," Lasers in surgery and medicine **43**, 143-151 (2011).
46. C. A. Patil, J. Kalkman, D. J. Faber, J. S. Nyman, T. G. van Leeuwen, and A. Mahadevan-Jansen, "Integrated system for combined Raman spectroscopy-spectral domain optical coherence tomography," J Biomed Opt **16**(2011).
47. S. Nori, F. Rius-Díaz, J. Cuevas, M. Goldgeier, P. Jaen, A. Torres, and S. González, "Sensitivity and specificity of reflectance-mode confocal microscopy for in vivo diagnosis of basal cell carcinoma: a multicenter study," Journal of the American Academy of Dermatology **51**, 923-930 (2004).
48. Y. Rivenson, H. Wang, Z. Wei, K. de Haan, Y. Zhang, Y. Wu, H. Günaydın, J. E. Zuckerman, T. Chong, and A. E. Sisk, "Virtual histological staining of unlabelled tissue-autofluorescence images via deep learning," Nature Biomedical Engineering, 1 (2019).
49. J. T. Kwak, S. M. Hewitt, S. Sinha, and R. Bhargava, "Multimodal microscopy for automated histologic analysis of prostate cancer," BMC cancer **11**, 62 (2011).
50. T. W. Bocklitz, F. S. Salah, N. Vogler, S. Heuke, O. Chernavskaia, C. Schmidt, M. J. Waldner, F. R. Greten, R. Brauer, M. Schmitt, A. Stallmach, I. Petersen, and J. Popp, "Pseudo-HE images derived from CARS/TPEF/SHG multimodal imaging in combination with Raman-spectroscopy as a pathological screening tool," Bmc Cancer **16**(2016).

51. Y. K. Tao, D. Shen, Y. Sheikine, O. O. Ahsen, H. H. Wang, D. B. Schmolze, N. B. Johnson, J. S. Brooker, A. E. Cable, and J. L. Connolly, "Assessment of breast pathologies using nonlinear microscopy," Proceedings of the National Academy of Sciences **111**, 15304-15309 (2014).
52. M. G. Giacomelli, T. Yoshitake, L. C. Cahill, H. Vardeh, L. M. Quintana, B. E. Faulkner-Jones, J. Brooker, J. L. Connolly, and J. G. Fujimoto, "Multiscale nonlinear microscopy and widefield white light imaging enables rapid histological imaging of surgical specimen margins," Biomedical optics express **9**, 2457-2475 (2018).
53. N. Singla, K. Dubey, and V. Srivastava, "Automated assessment of breast cancer margin in optical coherence tomography images via pretrained convolutional neural network," Journal of biophotonics **12**, e201800255 (2019).
54. H. Lin, C. Wei, G. Wang, H. Chen, L. Lin, M. Ni, J. Chen, and S. Zhuo, "Automated classification of hepatocellular carcinoma differentiation using multiphoton microscopy and deep learning," Journal of biophotonics, e201800435 (2019).
55. A. Mahadevan‐Jansen, M. F. Mitchell, N. Ramanujamf, A. Malpica, S. Thomsen, U. Utzinger, and R. Richards‐Kortumt, "Near‐Infrared Raman Spectroscopy for In Vitro Detection of Cervical Precancers," Photochemistry and photobiology **68**, 123-132 (1998).
56. J. Chen and X. Wang, "A new approach to near-infrared spectral data analysis using independent component analysis," Journal of Chemical Information and Computer Sciences **41**, 992-1001 (2001).
57. A. S. Haka, Z. Volynskaya, J. A. Gardecki, J. Nazemi, J. Lyons, D. Hicks, M. Fitzmaurice, R. R. Dasari, J. P. Crowe, and M. S. Feld, "In vivo margin assessment during partial mastectomy breast surgery using Raman spectroscopy," Cancer Research **66**, 3317-3322 (2006).
58. L. A. Austin, S. Osseiran, and C. L. Evans, "Raman technologies in cancer diagnostics," Analyst **141**, 476-503 (2016).
59. O. Stevens, I. E. Iping Petterson, J. C. Day, and N. Stone, "Developing fibre optic Raman probes for applications in clinical spectroscopy," Chem Soc Rev **45**, 1919-1934 (2016).
60. I. Barman, N. C. Dingari, A. Saha, S. McGee, L. H. Galindo, W. Liu, D. Plecha, N. Klein, R. R. Dasari, and M. Fitzmaurice, "Application of Raman spectroscopy to identify microcalcifications and underlying breast lesions at stereotactic core needle biopsy," Cancer research **73**, 3206-3215 (2013).
61. R. Sathyavathi, A. Saha, J. S. Soares, N. Spegazzini, S. McGee, R. R. Dasari, M. Fitzmaurice, and I. Barman, "Raman spectroscopic sensing of carbonate intercalation in breast microcalcifications at stereotactic biopsy," Scientific reports **5**(2015).
62. P. Crow, A. Molckovsky, N. Stone, J. Uff, B. Wilson, and L.-M. Wongkeesong, "Assessment of fiberoptic near-infrared Raman spectroscopy for diagnosis of bladder and prostate cancer," Urology **65**, 1126-1130 (2005).

63. N. D. Magee, J. S. Villaumie, E. T. Marple, M. Ennis, J. S. Elborn, and J. J. McGarvey, "Ex vivo diagnosis of lung cancer using a Raman miniprobe," The Journal of Physical Chemistry B **113**, 8137-8141 (2009).
64. B. Bodanese, F. L. Silveira, R. A. Zangaro, M. T. T. Pacheco, C. A. Pasqualucci, and L. Silveira, Jr., "Discrimination of Basal Cell Carcinoma and Melanoma from Normal Skin Biopsies in Vitro Through Raman Spectroscopy and Principal Component Analysis," Photomedicine and Laser Surgery **30**, 381-387 (2012).
65. L. Silveira, F. L. Silveira, B. Bodanese, R. A. Zangaro, and M. T. T. Pacheco, "Discriminating model for diagnosis of basal cell carcinoma and melanoma in vitro based on the Raman spectra of selected biochemicals," J Biomed Opt **17**, 077003-077003 (2012).
66. A. Mahadevan‐Jansen, M. F. Mitchell, N. Ramanujam, U. Utzinger, and R. Richards‐Kortum, "Development of a fiber optic probe to measure NIR Raman spectra of cervical tissue in vivo," Photochemistry and photobiology **68**, 427-431 (1998).
67. L. Lim, B. Nichols, M. R. Migden, N. Rajaram, J. S. Reichenberg, M. K. Markey, M. I. Ross, and J. W. Tunnell, "Clinical study of noninvasive in vivo melanoma and nonmelanoma skin cancers using multimodal spectral diagnosis," J Biomed Opt **19**(2014).
68. B. R. Masters and P. So, *Handbook of biomedical nonlinear optical microscopy* (Oxford University Press, 2008).
69. J.-X. Cheng, Y. K. Jia, G. Zheng, and X. S. Xie, "Laser-scanning coherent anti-Stokes Raman scattering microscopy and applications to cell biology," Biophysical journal **83**, 502-509 (2002).
70. C. W. Freudiger, W. Min, B. G. Saar, S. Lu, G. R. Holtom, C. He, J. C. Tsai, J. X. Kang, and X. S. Xie, "Label-free biomedical imaging with high sensitivity by stimulated Raman scattering microscopy," Science **322**, 1857-1861 (2008).
71. O. Uckermann, R. Galli, S. Tamosaityte, E. Leipnitz, K. D. Geiger, G. Schackert, E. Koch, G. Steiner, and M. Kirsch, "Label-Free Delineation of Brain Tumors by Coherent Anti-Stokes Raman Scattering Microscopy in an Orthotopic Mouse Model and Human Glioblastoma," Plos One **9**(2014).
72. V.-H. Le, S. W. Yoo, Y. Yoon, T. Wang, B. Kim, S. Lee, K.-H. Lee, K. H. Kim, and E. Chung, "Brain tumor delineation enhanced by moxifloxacin-based two-photon/CARS combined microscopy," Biomedical Optics Express **8**, 2148-2161 (2017).
73. S. Heuke, N. Vogler, T. Meyer, D. Akimov, F. Kluschke, H. J. Roewert-Huber, J. Lademann, B. Dietzek, and J. Popp, "Multimodal mapping of human skin," British Journal of Dermatology **169**, 794-803 (2013).
74. L. Gao, Z. Wang, F. Li, A. A. Hammoudi, M. J. Thrall, P. T. Cagle, and S. T. C. Wong, "Differential Diagnosis of Lung Carcinoma With Coherent Anti-Stokes Raman Scattering Imaging," Archives of Pathology & Laboratory Medicine **136**, 1502-1510 (2012).

75. I. I. Patel, C. Steuwe, S. Reichelt, and S. Mahajan, "Coherent anti-Stokes Raman scattering for label-free biomedical imaging," Journal of Optics **15**(2013).
76. C. H. Camp, Jr. and M. T. Cicerone, "Chemically sensitive bioimaging with coherent Raman scattering," Nat Photonics **9**, 295-305 (2015).
77. A. Lombardini, V. Mytskaniuk, S. Sivankutty, E. R. Andresen, X. Chen, J. Wenger, M. Fabert, N. Joly, F. Louradour, and A. Kudlinski, "High-resolution multimodal flexible coherent Raman endoscope," Light: Science & Applications **7**, 10 (2018).
78. C. W. Freudiger, R. Pfannl, D. A. Orringer, B. G. Saar, M. Ji, Q. Zeng, L. Ottoboni, W. Ying, C. Waeber, J. R. Sims, P. L. De Jager, O. Sagher, M. A. Philbert, X. Xu, S. Kesari, X. S. Xie, and G. S. Young, "Multicolored stain-free histopathology with coherent Raman imaging," Laboratory Investigation **92**, 1492-1502 (2012).
79. M. Ji, D. A. Orringer, C. W. Freudiger, S. Ramkissoon, X. Liu, D. Lau, A. J. Golby, I. Norton, M. Hayashi, N. Y. R. Agar, G. S. Young, C. Spino, S. Santagata, S. Camelo-Piragua, K. L. Ligon, O. Sagher, and X. S. Xie, "Rapid, Label-Free Detection of Brain Tumors with Stimulated Raman Scattering Microscopy," Science Translational Medicine **5**(2013).
80. M. Ji, S. Lewis, S. Camelo-Piragua, S. H. Ramkissoon, M. Snuderl, S. Venneti, A. Fisher-Hubbard, M. Garrard, D. Fu, and A. C. Wang, "Detection of human brain tumor infiltration with quantitative stimulated Raman scattering microscopy," Science translational medicine **7**, 309ra163-309ra163 (2015).
81. C.-S. Liao, P. Wang, C. Y. Huang, P. Lin, G. Eakins, R. T. Bentley, R. Liang, and J.-X. Cheng, "In vivo and in situ spectroscopic imaging by a handheld stimulated Raman scattering microscope," ACS Photonics **5**, 947-954 (2017).
82. C. W. Freudiger, W. Yang, G. R. Holtom, N. Peyghambarian, X. S. Xie, and K. Q. Kieu, "Stimulated Raman scattering microscopy with a robust fibre laser source," Nat Photonics **8**, 153 (2014).
83. J. Qi and W.-C. Shih, "Performance of line-scan Raman microscopy for high-throughput chemical imaging of cell population," Appl Optics **53**, 2881-2885 (2014).
84. K. St-Arnaud, K. Aubertin, M. Strupler, M. Jermyn, K. Petrecca, D. Trudel, and F. Leblond, "Wide-field spontaneous Raman spectroscopy imaging system for biological tissue interrogation," Optics Letters **41**, 4692-4695 (2016).
85. D. Wei, S. Chen, Y. H. Ong, C. Perlaki, and Q. Liu, "Fast wide-field Raman spectroscopic imaging based on simultaneous multi-channel image acquisition and Wiener estimation," Optics letters **41**, 2783-2786 (2016).
86. L. Kong, M. Navas-Moreno, and J. W. Chan, "Fast confocal Raman imaging using a 2-D multifocal array for parallel hyperspectral detection," Analytical chemistry **88**, 1281-1285 (2015).
87. H. Jobin-Yvon, "Technical note: RA-TN04: DuoScan Imaging," (2012).
88. K. Hamada, K. Fujita, N. I. Smith, M. Kobayashi, Y. Inouye, and S. Kawata, "Raman microscopy for dynamic molecular imaging of living cells," Journal of biomedical optics **13**, 044027-044027-044024 (2008).

89. K. Hamada, K. Fujita, M. Kobayashi, and S. Kawata, "Observation of cell dynamics by laser scanning Raman microscope," in *Biomedical Optics (BiOS) 2007*, (International Society for Optics and Photonics, 2007), 64430Z-64430Z-64436.
90. M. Okuno and H.-o. Hamaguchi, "Multifocus confocal Raman microspectroscopy for fast multimode vibrational imaging of living cells," Optics Letters **35**, 4096-4098 (2010).
91. J. Qi and W.-C. Shih, "Parallel Raman microspectroscopy using programmable multipoint illumination," Optics Letters **37**, 1289-1291 (2012).
92. F. Sinjab, K. Kong, G. Gibson, S. Varma, H. Williams, M. Padgett, and I. Notingher, "Tissue diagnosis using power-sharing multifocal Raman micro-spectroscopy and auto-fluorescence imaging," Biomedical optics express **7**, 2993-3006 (2016).
93. G. Falgayrac, B. Cortet, O. Devos, J. Barbillat, V. Pansini, A. Cotten, G. Pasquier, H. Migaud, and G. Penel, "Comparison of two-dimensional fast raman imaging versus point-by-point acquisition mode for human bone characterization," Analytical chemistry **84**, 9116-9123 (2012).
94. M. Sharma, E. Marple, J. Reichenberg, and J. W. Tunnell, "Design and characterization of a novel multimodal fiber-optic probe and spectroscopy system for skin cancer applications," Rev Sci Instrum **85**(2014).
95. K. E. Shafer-Peltier, A. S. Haka, J. T. Motz, M. Fitzmaurice, R. R. Dasari, and M. S. Feld, "Model-based biological Raman spectral imaging," Journal of Cellular Biochemistry, 125-137 (2002).
96. N. Stone, M. C. H. Prieto, P. Crow, J. Uff, and A. W. Ritchie, "The use of Raman spectroscopy to provide an estimation of the gross biochemistry associated with urological pathologies," Analytical and bioanalytical chemistry **387**, 1657-1668 (2007).
97. M. S. Bergholt, W. Zheng, K. Lin, K. Y. Ho, M. Teh, K. G. Yeoh, J. B. Y. So, and Z. Huang, "Characterizing variability in in vivo Raman spectra of different anatomical locations in the upper gastrointestinal tract toward cancer detection," J Biomed Opt **16**, 037003-037003-037010 (2011).
98. H. L. Jianhua Zhao, David I. McLean and Haishan Zeng, "Real time raman spectroscopy for noninvasive in vivo skin analysis and diagnosis," New Developments in Biomedical Engineering (2010).
99. H. P. Buschman, G. Deinum, J. T. Motz, M. Fitzmaurice, J. R. Kramer, A. van der Laarse, A. V. Bruschke, and M. S. Feld, "Raman microspectroscopy of human coronary atherosclerosis: Biochemical assessment of cellular and extracellular morphologic structures in situ," Cardiovascular Pathology **10**, 69-82 (2001).
100. K. E. Shafer-Peltier, A. S. Haka, M. Fitzmaurice, J. Crowe, J. Myles, R. R. Dasari, and M. S. Feld, "Raman microspectroscopic model of human breast tissue: implications for breast cancer diagnosis in vivo," Journal of Raman Spectroscopy **33**, 552-563 (2002).

101. J. Zhao, H. Lui, D. I. McLean, and H. Zeng, "Integrated real‐time Raman system for clinical in vivo skin analysis," Skin Research and Technology **14**, 484-492 (2008).
102. J. Jaumot, A. de Juan, and R. Tauler, "MCR-ALS GUI 2.0: new features and applications," Chemometrics and Intelligent Laboratory Systems **140**, 1-12 (2015).
103. C. A. Lieber and A. Mahadevan-Jansen, "Automated method for subtraction of fluorescence from biological Raman spectra," Applied spectroscopy **57**, 1363-1367 (2003).
104. D. Zhang, P. Wang, M. N. Slipchenko, D. Ben-Amotz, A. M. Weiner, and J.-X. Cheng, "Quantitative vibrational imaging by hyperspectral stimulated Raman scattering microscopy and multivariate curve resolution analysis," Analytical Chemistry **85**, 98-106 (2013).
105. W. Windig and D. Stephenson, "Self-modeling mixture analysis of second-derivative near-infrared spectral data using the SIMPLISMA approach," Analytical Chemistry **64**, 2735-2742 (1992).
106. J. T. Motz, M. Hunter, L. H. Galindo, J. A. Gardecki, J. R. Kramer, R. R. Dasari, and M. S. Feld, "Optical fiber probe for biomedical Raman spectroscopy," Appl Optics **43**, 542-554 (2004).
107. R. Manoharan, J. J. Baraga, M. S. Feld, and R. P. Rava, "Quantitative Histochemical Analysis of Human Artery Using Raman-Spectroscopy," J Photoch Photobio B **16**, 211-233 (1992).
108. S. Wold, A. Ruhe, H. Wold, and I. Dunn, WJ, "The collinearity problem in linear regression. The partial least squares (PLS) approach to generalized inverses," SIAM Journal on Scientific and Statistical Computing **5**, 735-743 (1984).
109. P. R. T. Jess, V. Garces-Chavez, D. Smith, M. Mazilu, L. Paterson, A. Riches, C. S. Herrington, W. Sibbett, and K. Dholakia, "Dual beam fibre trap for Raman microspectroscopy of single cells," Opt Express **14**, 5779-5791 (2006).
110. D. T. Downing, "Lipid and protein structures in the permeability barrier of mammalian epidermis," J Lipid Res **33**, 301-313 (1992).
111. Z. Movasaghi, S. Rehman, and I. U. Rehman, "Raman spectroscopy of biological tissues," Applied Spectroscopy Reviews **42**, 493-541 (2007).
112. P. Olczyk, Ł. Mencner, and K. Komosinska-Vassev, "The role of the extracellular matrix components in cutaneous wound healing," BioMed research international **2014**(2014).
113. A. Pappas, "Epidermal surface lipids," Dermato-endocrinology **1**, 72-76 (2009).
114. M. Rajadhyaksha, M. Grossman, D. Esterowitz, R. H. Webb, and R. R. Anderson, "In vivo confocal scanning laser microscopy of human skin: melanin provides strong contrast," J Invest Dermatol **104**, 946-952 (1995).
115. Z. Huang, H. Lui, X. Chen, A. Alajlan, D. I. McLean, and H. Zeng, "Raman spectroscopy of in vivo cutaneous melanin," J Biomed Opt **9**, 1198-1205 (2004).

116. P. Vítek, K. Osterrothová, and J. Jehlička, "Beta-carotene—a possible biomarker in the Martian evaporitic environment: Raman micro-spectroscopic study," Planetary and Space Science **57**, 454-459 (2009).
117. P. J. Caspers, G. W. Lucassen, E. A. Carter, H. A. Bruining, and G. J. Puppels, "In vivo confocal Raman microspectroscopy of the skin: noninvasive determination of molecular concentration profiles," J Invest Dermatol **116**, 434-442 (2001).
118. A. S. Haka, K. E. Shafer-Peltier, M. Fitzmaurice, J. Crowe, R. R. Dasari, and M. S. Feld, "Diagnosing breast cancer by using Raman spectroscopy," P Natl Acad Sci USA **102**, 12371-12376 (2005).
119. D. Weedon, "Tumors of the epidermis," Skin pathology, 753-802 (2002).
120. C. A. Lieber, S. K. Majumder, D. L. Ellis, D. D. Billheimer, and A. Mahadevan‐Jansen, "In vivo nonmelanoma skin cancer diagnosis using Raman microspectroscopy," Lasers in surgery and medicine **40**, 461-467 (2008).
121. W.-C. Shih, K. L. Bechtel, and M. S. Feld, "Intrinsic Raman spectroscopy for quantitative biological spectroscopy part I: theory and simulations," Opt Express **16**, 12726-12736 (2008).
122. M. Gniadecka, P. A. Philipsen, S. Sigurdsson, S. Wessel, O. F. Nielsen, D. H. Christensen, J. Hercogova, K. Rossen, H. K. Thomsen, R. Gniadecki, L. K. Hansen, and H. C. Wulf, "Melanoma diagnosis by Raman spectroscopy and neural networks: Structure alterations in proteins and lipids in intact cancer tissue," J Invest Dermatol **122**, 443-449 (2004).
123. J. Schleusener, P. Gluszczynska, C. Reble, I. Gersonde, J. Helfmann, J. W. Fluhr, J. Lademann, J. Roewert-Huber, A. Patzelt, and M. C. Meinke, "In vivo study for the discrimination of cancerous and normal skin using fibre probe-based Raman spectroscopy," Experimental Dermatology **24**, 767-772 (2015).
124. J. Zhao, H. Lui, S. Kalia, and H. Zeng, "Real-time Raman spectroscopy for automatic in vivo skin cancer detection: an independent validation," Analytical and bioanalytical chemistry **407**, 8373-8379 (2015).
125. F. L. Silveira, M. T. Pacheco, B. Bodanese, C. A. Pasqualucci, R. A. Zangaro, and L. Silveira, Jr., "Discrimination of non-melanoma skin lesions from non-tumor human skin tissues in vivo using Raman spectroscopy and multivariate statistics," Lasers Surg Med **47**, 6-16 (2015).
126. X. Feng, A. J. Moy, H. T. M. Nguyen, J. Zhang, M. C. Fox, K. R. Sebastian, J. S. Reichenberg, M. K. Markey, and J. W. Tunnell, "Raman active components of skin cancer," Biomedical Optics Express **8**, 2835-2850 (2017).
127. G. Pezzotti, M. Boffelli, D. Miyamori, T. Uemura, Y. Marunaka, W. Zhu, and H. Ikegaya, "Raman spectroscopy of human skin: looking for a quantitative algorithm to reliably estimate human age," J Biomed Opt **20**, 065008 (2015).
128. P. Caspers, G. Lucassen, R. Wolthuis, H. Bruining, and G. Puppels, "In vitro and in vivo Raman spectroscopy of human skin," BIOSPECTROSCOPY-NEW YORK- **4**, S31-S40 (1998).

129. B. Barry, H. Edwards, and A. Williams, "Fourier transform Raman and infrared vibrational study of human skin: assignment of spectral bands," Journal of Raman Spectroscopy **23**, 641-645 (1992).
130. X. Robin, N. Turck, A. Hainard, N. Tiberti, F. Lisacek, J.-C. Sanchez, and M. Müller, "pROC: an open-source package for R and S+ to analyze and compare ROC curves," BMC bioinformatics **12**, 77 (2011).
131. S. Duraipandian, W. Zheng, J. Ng, J. J. Low, A. Ilancheran, and Z. Huang, "Simultaneous fingerprint and high-wavenumber confocal Raman spectroscopy enhances early detection of cervical precancer in vivo," Anal Chem **84**, 5913-5919 (2012).
132. S. K. Teh, W. Zheng, K. Y. Ho, M. Teh, K. G. Yeoh, and Z. Huang, "Near-infrared Raman spectroscopy for gastric precancer diagnosis," Journal of Raman Spectroscopy **40**, 908-914 (2009).
133. A. Daniel, A. Prakasarao, and S. Ganesan, "Near-infrared Raman spectroscopy for estimating biochemical changes associated with different pathological conditions of cervix," Spectrochimica Acta Part A: Molecular and Biomolecular Spectroscopy (2017).
134. S. Zucker, T. Turpeenniemi-Hujanen, N. Ramamurthy, J. Wieman, R. Lysik, P. Gorevic, L. Liotta, S. Simon, and L. Golub, "Purification and characterization of a connective-tissue-degrading metalloproteinase from the cytosol of metastatic melanoma cells," Biochemical Journal **245**, 429-437 (1987).
135. T. Quan, Z. Qin, W. Xia, Y. Shao, J. J. Voorhees, and G. J. Fisher, "Matrix-degrading metalloproteinases in photoaging," in *Journal of Investigative Dermatology Symposium Proceedings*, (Elsevier, 2009), 20-24.
136. F. M. Watt and H. Fujiwara, "Cell-extracellular matrix interactions in normal and diseased skin," Cold Spring Harbor perspectives in biology **3**, a005124 (2011).
137. E. C. Naylor, R. E. Watson, and M. J. Sherratt, "Molecular aspects of skin ageing," Maturitas **69**, 249-256 (2011).
138. V. R. Yanofsky, S. E. Mercer, and R. G. Phelps, "Histopathological variants of cutaneous squamous cell carcinoma: a review," Journal of skin cancer **2011**(2010).
139. W. Fu and C. J. Cockerell, "The actinic (solar) keratosis: a 21st-century perspective," Archives of dermatology **139**, 66-70 (2003).
140. MathWorks, "Generalized linear mixed-effects models", retrieved https://www.mathworks.com/help/stats/mixed-effects-2.html.
141. V. Mundra, W. Li, and R. I. Mahato, "Nanoparticle-mediated drug delivery for treating melanoma," Nanomedicine **10**, 2613-2633 (2015).
142. S. K. Paidi, A. Rizwan, C. Zheng, M. L. Cheng, K. Glunde, and I. Barman, "Label-Free Raman Spectroscopy Detects Stromal Adaptations in Premetastatic Lungs Primed by Breast Cancer," Cancer Research **77**, 247-256 (2017).
143. A. Sahu, A. Deshmukh, A. R. Hole, P. Chaturvedi, and C. M. Krishna, "In vivo subsite classification and diagnosis of oral cancers using Raman spectroscopy," Journal of Innovative Optical Health Sciences **9**(2016).

144. S. A. Boppart, J. Q. Brown, C. S. Farah, E. Kho, L. Marcu, C. M. Saunders, and H. J. Sterenborg, "Label-free optical imaging technologies for rapid translation and use during intraoperative surgical and tumor margin assessment," J Biomed Opt **23**, 021104 (2017).
145. F. E. Harrell Jr, *Regression modeling strategies: with applications to linear models, logistic and ordinal regression, and survival analysis* (Springer, 2015).
146. E. W. Steyerberg, F. E. Harrell, G. J. Borsboom, M. Eijkemans, Y. Vergouwe, and J. D. F. Habbema, "Internal validation of predictive models: efficiency of some procedures for logistic regression analysis," Journal of clinical epidemiology **54**, 774-781 (2001).
147. A. C. Society, *Cancer facts & figures 2018* (American Cancer Society, Altanta, 2018).
148. N. Smeets, D. Kuijpers, P. Nelemans, J. Ostertag, M. Verhaegh, G. Krekels, and H. Neumann, "Mohs' micrographic surgery for treatment of basal cell carcinoma of the face——results of a retrospective study and review of the literature," British journal of dermatology **151**, 141-147 (2004).
149. K. V. Viola, M. B. Jhaveri, P. R. Soulos, R. B. Turner, W. L. Tolpinrud, D. Doshi, and C. P. Gross, "Mohs micrographic surgery and surgical excision for nonmelanoma skin cancer treatment in the Medicare population," Arch. Dermatol. **148**, 473-477 (2012).
150. M. Shareef and W. Hussain, "The M ohs histotechnician: a review of training and practice within 29 centres in the UK," Clinical and experimental dermatology **38**, 589-593 (2013).
151. K. Kong, C. J. Rowlands, S. Varma, W. Perkins, I. H. Leach, A. A. Koloydenko, H. C. Williams, and I. Notingher, "Diagnosis of tumors during tissue-conserving surgery with integrated autofluorescence and Raman scattering microscopy," Proceedings of the National Academy of Sciences **110**, 15189-15194 (2013).
152. M. Jermyn, K. Mok, J. Mercier, J. Desroches, J. Pichette, K. Saint-Arnaud, L. Bernstein, M. C. Guiot, K. Petrecca, and F. Leblond, "Intraoperative brain cancer detection with Raman spectroscopy in humans," Sci Transl Med **7**, 274ra219 (2015).
153. M. Kirsch, G. Schackert, R. Salzer, and C. Krafft, "Raman spectroscopic imaging for in vivo detection of cerebral brain metastases," Analytical and Bioanalytical Chemistry **398**, 1707-1713 (2010).
154. I. Behl, L. Kukreja, A. Deshmukh, S. Singh, H. Mamgain, A. R. Hole, and C. M. Krishna, "Raman mapping of oral buccal mucosa: a spectral histopathology approach," J Biomed Opt **19**, 126005-126005 (2014).
155. F. L. Cals, T. B. Schut, P. Caspers, R. B. de Jong, S. Koljenović, and G. J. Puppels, "Raman spectroscopic analysis of the molecular composition of oral cavity squamous cell carcinoma and healthy tongue tissue," Analyst **143**, 4090-4102 (2018).

156. M. D. Keller, E. Vargis, A. Mahadevan-Jansen, N. de Matos Granja, R. H. Wilson, M.-A. Mycek, and M. C. Kelley, "Development of a spatially offset Raman spectroscopy probe for breast tumor surgical margin evaluation," J Biomed Opt **16**, 077006 (2011).
157. S. K. Teh, W. Zheng, K. Y. Ho, M. Teh, K. G. Yeoh, and Z. Huang, "Diagnostic potential of near-infrared Raman spectroscopy in the stomach: differentiating dysplasia from normal tissue," British Journal of Cancer **98**, 457-465 (2008).
158. A. Nijssen, T. C. B. Schut, F. Heule, P. J. Caspers, D. P. Hayes, M. H. A. Neumann, and G. J. Puppels, "Discriminating basal cell carcinoma from its surrounding tissue by Raman spectroscopy," J Invest Dermatol **119**, 64-69 (2002).
159. M. Larraona-Puy, A. Ghita, A. Zoladek, W. Perkins, S. Varma, I. H. Leach, A. A. Koloydenko, H. Williams, and I. Notingher, "Development of Raman microspectroscopy for automated detection and imaging of basal cell carcinoma," J Biomed Opt **14**, 054031-054031-054010 (2009).
160. M. Larraona-Puy, A. Ghita, A. Zoladek, W. Perkins, S. Varma, I. Leach, A. Koloydenko, H. Williams, and I. Notingher, "Discrimination between basal cell carcinoma and hair follicles in skin tissue sections by Raman micro-spectroscopy," Journal of Molecular Structure **993**, 57-61 (2011).
161. X. Feng, A. J. Moy, H. T. Nguyen, J. Zhang, M. C. Fox, K. R. Sebastian, J. S. Reichenberg, M. K. Markey, and J. W. Tunnell, "Raman active components of skin cancer," Biomedical optics express **8**, 2835-2850 (2017).
162. R. Boitor, K. Kong, D. Shipp, S. Varma, A. Koloydenko, K. Kulkarni, S. Elsheikh, T. B. Schut, P. Caspers, and G. Puppels, "Automated multimodal spectral histopathology for quantitative diagnosis of residual tumour during basal cell carcinoma surgery," Biomedical optics express **8**, 5749-5766 (2017).
163. X. Feng, A. J. Moy, H. T. Nguyen, Y. Zhang, J. Zhang, M. C. Fox, K. R. Sebastian, J. S. Reichenberg, M. K. Markey, and J. W. Tunnell, "Raman biophysical markers in skin cancer diagnosis," J Biomed Opt **23**, 057002 (2018).
164. X. Feng, A. J. Moy, H. T. Nguyen, Y. Zhang, M. C. Fox, K. R. Sebastian, J. S. Reichenberg, M. K. Markey, and J. W. Tunnell, "Raman spectroscopy reveals biophysical markers in skin cancer surgical margins," in *Biomedical Vibrational Spectroscopy 2018: Advances in Research and Industry*, (International Society for Optics and Photonics, 2018), 104900B.
165. M. Miljkovic, "Label-free imaging of human cells: algorithms for image reconstruction of Raman hyperspectral datasets," Analyst (2010).
166. D. Bates, M. Mächler, B. Bolker, and S. Walker, "Fitting linear mixed-effects models using lme4," arXiv preprint arXiv:1406.5823 (2014).
167. S. G. Luke, "Evaluating significance in linear mixed-effects models in R," Behavior Research Methods **49**, 1494-1502 (2017).
168. M. A. Short, H. Lui, D. McLean, H. Zeng, A. Alajlan, and X. K. Chen, "Changes in nuclei and peritumoral collagen within nodular basal cell carcinomas via

confocal micro-Raman spectroscopy," J Biomed Opt **11**, 034004-034004-034009 (2006).
169. M. R. Schneider, R. Schmidt-Ullrich, and R. Paus, "The hair follicle as a dynamic miniorgan," Current Biology **19**, R132-R142 (2009).
170. S. J. Miller, "Biology of basal cell carcinoma (Part I)," Journal of the American Academy of Dermatology **24**, 1-13 (1991).
171. K.-i. Yoshikawa, Y. Katagata, and S. Kondo, "Biochemical and immunohistochemical analyses of keratin expression in basal cell carcinoma," Journal of dermatological science **17**, 15-23 (1998).
172. W.-S. Lee, "Integral hair lipid in human hair follicle," Journal of dermatological science **64**, 153-158 (2011).
173. A. H. T. F. S. M. Connolly, D. R. Baker, B. M. Coldiron, M. J. Fazio, P. A. Storrs, A. T. Vidimos, M. J. Zalla, J. D. Brewer, W. S. Begolka, and R. P. T. G. Berger, "AAD/ACMS/ASDSA/ASMS 2012 Appropriate Use Criteria for M ohs Micrographic Surgery: A Report of the A merican A cademy of D ermatology, A merican C ollege of M ohs S urgery, A merican S ociety for D ermatologic S urgery A ssociation, and the A merican S ociety for M ohs Surgery," Dermatologic Surgery **38**, 1582-1603 (2012).
174. D. W. Shipp, E. A. Rakha, A. A. Koloydenko, R. D. Macmillan, I. O. Ellis, and I. Notingher, "Intra-operative spectroscopic assessment of surgical margins during breast conserving surgery," Breast Cancer Research **20**, 69 (2018).
175. J. Karen, D. Gareau, S. Dusza, M. Tudisco, M. Rajadhyaksha, and K. Nehal, "Detection of basal cell carcinomas in Mohs excisions with fluorescence confocal mosaicing microscopy," British Journal of Dermatology **160**, 1242-1250 (2009).
176. J. Wang, K. Lin, W. Zheng, K. Y. Ho, M. Teh, K. G. Yeoh, and Z. Huang, "Comparative study of the endoscope-based bevelled and volume fiber-optic Raman probes for optical diagnosis of gastric dysplasia in vivo at endoscopy," Analytical and Bioanalytical Chemistry **407**, 8303-8310 (2015).
177. L. Lim, "Clinical, non-invasive in vivo diagnosis of skin cancer using multimodal Spectral Diagnosis," (2013).